Chemical profiling of cultivated and wild African ginger and absolute configurations of compounds from mangroves and *Ancistrocladus* species

by

KATELE ZONGWE Félix Junior

Submitted in partial fulfillment of the requirements for the degree

MAGISTER SCIENTIAE

In the Faculty of Natural & Agricultural Sciences

UNIVERSITY OF PRETORIA

PRETORIA

Supervisor: Prof. V. J. Maharaj

Co-supervisor: Prof. G. Bringmann

December 2015

Declaration

I, **KATELE ZONGWE Félix Junior** declare that the theis/dissertation, which I hereby submit for the degree MSc chemistry at the University of Pretoria, is my own work and has not previously been submitted by me for a degree at this or any other tertiary institution.

Signature: ……

Date: ……

Acknowledgements

I would sincerely like to express all my gratitude to my supervisors **Prof. V. J. Maharaj** and **Prof. G. Bringmann**, from the University of Pretoria and the University of Würzburg respectively, for their commitment and all their incredible scientific contributions to the present work. Thank you for the opportunity you have given me to learn from your side.

A special thanks to **Dr. T. Bruhn** from **AK Bringmann**, University of Würzburg, for the coaching in quantum-chemical calculations of chiroptical spectroscopy. This has been much appreciated and will never be forgotten.

All my gratitude to the **BEBUC Scholarship System** and its panel members for the master scholarship; as well as the nonprofit organization ***f*UNIKIN** (**Förderverein Uni Kinshasa e.V.**) – initiated by **Prof. G. Bringmann** and co-presided with **Prof. V. Mudogo** from the University of Kinshasa, for the greatest vision ever that aimed at promoting excellency and raising a new generation of professors in Congolese universities. Words are not enough to express my gratitude for financial and all other supports of any kind!

Thanks to **S. Pöhlmann** and **C. Wolf** for all the affection and the never-to-be-forgotten incredible time in Würzburg; and the **Holger-Pöhlmann-Stiftung** for additional financial supports.

A particular thanks to **Dr. K. Ndjoko** (BEBUC general manager) and **Dr. med. H. Mavoko** for all the remarkable advices and fruitful discussions.

To my parents **A. Katele** and **S. Mulezi**, a great thanks for all advices, encouragements and supports; to **Papa L. Badi** and his family for kindheartedness and accommodation in Pretoria.

Thanks to **Dr. A. Zillenbiller**, **A. Gehrold**, **B. Schinner-Schäfer** from AK Bringmann, for all the assistances with administrative matters at the University of Würzburg; **C. Froschgeiser**, **C. Steinert**, **E. Schoenemann**, **F. Witterauf**, **Dr. J. Li**, **J. Wendrich** and **M. Pfletscher** for all the amazing moments spent together in Würzburg, Germany. That was appreciated a lot!

To my friends and colleagues **B.K. Lombe**, **D.T. Tshitenge** and **J.P. Mufusama** (the AK Bringmann Congolese guys), a great thanks for all the fruitful scientific discussions and extra hilarious moments; the **African community of Würzburg** (**P. Shama**, **V. Fungula** and others) for all cultural, sportive and para academic activities.

Thanks to **Dr. D. Koot**, **D. Liles**, **Dr. Y. Naudé** and **E. Palmer** for UPLC MS, X-ray diffraction, GC MS and NMR experiments; to **Dr. N. Oktober**, **Dr. L. Pilcher**, **Dr. D. Riley** and my labmate **T. Shoko** for all scientific discussions and exciting group seminars.

"Natural products are a matchless source of novel drug leads and inspiration for the synthesis of non-natural molecules"

H. F. Li, X. J. Li, H. Y. Zhang, *EMBO Rep.* **2009**, *10*, 194-200.

… To **Christine Wolf** and **Sylvia Pöhlmann**,

I dedicate this work.

Summary

Medicinal plants and natural products have played a pivotal role as a source of drug leads that has led to improving health conditions and have provided humankind with numerous pharmacologically active drugs.

Other than the biological screening and chemical profiling of plant extracts, the isolation, purification and elucidation of the full absolute structures of natural compounds are some of the key areas required in the time-consuming process of drug discovery based on natural products.

Elucidation of the absolute configuration (AC) of chiral natural products represents one of the most challenging tasks in the determination of full molecular structures but still remains an essential concept in drug discovery as enantiomers do not always exhibit the same pharmacological activities.

The present study successively investigated the UPLC MS and GC MS chemical profiles of organic extracts from the wild and cultivated popular, but threatened medicinal plant, African ginger {i.e., *Siphonochilus aethiopicus* (Schweinf.) B.L. Burtt} and the absolute configurations of limonoids, diterpenoid and dimeric naphthylisoquinoline (NIQ) alkaloids isolated from mangroves and *Ancistrocladus* species.

The first part of the study aimed at exploring the similarities and/or differences between the UPLC MS and GC MS chemical profiles of wild and cultivated African ginger rhizomes and evaluating the antimalarial activity of extracts from both sources taking into account that traditional healers are not unanimous on using the cultivated material for medicinal purposes.

UPLC MS chemical profiling of n-hexane/DCM (1:1) extracts from air-dried rhizomes has revealed the presence of additional peaks in the chromatographic profiles of wild plants but also confirmed the major peak in the profiles of both wild and cultivated rhizomes to be the common furanoterpenoid (**4**), known as Siphonochilone. The compound was unexpectedly observed to be highly unstable and generated artefact sesquiterpenoids after autoxidation.

Autoxidation was observed for the pure compound, as well as in dried and powdered rhizomes. The latter aspect confirmed that the artefact sesquiterpenoids only form after autoxidation and do not occur in the fresh plant as reported in many publications.

GC MS analyses of n-hexane extracts from fresh, air-dried and oven-dried plants confirmed the presence of Siphonochilone (**4**) from both sources but further revealed the presence of eucalyptol, which was significantly depleted after drying.

Antimalarial screenings of n-hexane/DCM (1:1) extracts against the chloroquine-sensitive (CQS) strain of *Plasmodium falciparum* (NF54) did not show substantial change in the IC_{50} values for both sources.

The second part of the study aimed at elucidating the absolute configurations of two limonoids, one diterpenoid and two NIQ dimers. This was tackled by conducting quantum-chemical calculations of chiroptical spectroscopy, such as circular dichroism. Absolute configurations were deduced from the comparison between experimental chiroptical data with the curves predicted for the possible enantiomers.

The absolute configurations of the limonoids thaixylomolin A (**12**) and B (**13**) were respectively revealed as 1*R*,5*R*,8*R*,9*R*,10*R*,13*S*,14*R*,15*S*,17*S* and 1*R*,2*R*,3*S*,4*R*,5*S*,9*S*,10*R*,13*R*,17*R* while that of the diterpenoid decandrinin (**14**) was 5*S*,9*S*,10*R* and those for the NIQ dimers mbandakamines A (**15a**) and B (**15b**) validated published data.

Keywords: African ginger, chemical profiling, circular dichroism, optical rotatory dispersion, absolute configuration

List of abbreviations

AC	-	Absolute Configuration
ACN	-	Acetonitrile
BEBUC	-	Bourse d'Excellence Bringmann aux Universités Congolaises
CC	-	Coupled-Cluster
CD	-	Circular Dichroism
CE	-	Cotton Effect
CIP	-	Cahn-Ingold-Prelog
COSMO	-	Conductor-like Screening Model
COSY	-	Correlation Spectroscopy
CQ	-	Chloroquine
CQS	-	Chloroquine-Sensitive
CSIR	-	Council for Scientific and Industrial Research
CT	-	Charge-Transfer
DCM	-	Dichloromethane
DEPT-135	-	Distortionless Enhancement by Polarization 135°
DFT/MRCI	-	Density Functional Theory/Multi Reference Configuration Interaction
DNP	-	Dictionary of Natural Products
ECD	-	Electronic Circular Dichroism
EtOAc	-	Ethyl acetate
GC	-	Gas Chromatography
GC MS	-	Gas Chromatography Mass Spectrometry
HMBC	-	Heteronuclear Multiple Bond Correlation
HSQC	-	Heteronuclear Single Quantum Correlation
IR	-	Infrared
KZN	-	KwaZulu-Natal
lCpl	-	Left circularly polarized light
Lpl	-	Linearly polarized light
MMFF	-	Merck Molecular Force Field
MS	-	Mass Spectrometry

MW	-	Molecular Weight
NIQ	-	Naphthylisoquinoline alkaloid
NIST	-	National Institute of Standards and Technology iibrary
NMR	-	Nuclear Magnetic Resonance
NOE	-	Nuclear Overhauser Effect
NOESY	-	Nuclear Overhauser Effect Spectroscopy
NP	-	Natural Product
ORD	-	Optical Rotatory Dispersion
Rel. Int.	-	Relative intensities
rCpl	-	Right circularly polarized light
RI	-	Retention index
ROA	-	Raman Optical Activity
ROESY	-	Rotating-frame Overhauser Spectroscopy
RPA	-	Random Phase Approximation
RT	-	Retention time
TDA	-	Tamm-Dancoff Approximation
TD-DFT	-	Time Dependent-Density Functional Theory
TDM	-	Transition Dipole Moment
TIC	-	Total Ion Chromatogram
TLC	-	Thin Layer Chromatography
TOF MS EI	-	Time Of Flight Mass Spectrometry Electron Ionization
UCT	-	University of Cape Town
UPLC	-	Ultra Performance Liquid Chromatography
UPLC MS	-	Ultra Performance Liquid Chromatography Mass Spectrometry
UV	-	Ultraviolet

List of figures

Chapter 1: General introduction

Chapter 2: Chemical profiling of cultivated and wild African ginger, *Siphonochilus aethiopicus* (Schweinf.) B. L. Burtt

Chapter 3: Absolute configurations of compounds from mangroves and *Ancistrocladus* species

List of schemes

Chapter 2: Chemical profiling of cultivated and wild African ginger, *Siphonochilus aethiopicus* (Schweinf.) B. L. Burtt

Chapter 3: Absolute configurations of compounds from mangroves and *Ancistrocladus* species

List of tables

Chapter 2: Chemical profiling of cultivated and wild African ginger, *Siphonochilus aethiopicus* (Schweinf.) B. L. Burtt

Chapter 3: Absolute configurations of compounds from mangroves and *Ancistrocladus* species

Table of contents

Chapter 1

General introduction

The history of humanity has evidenced the vital role of medicinal plants in the improvement of health conditions (e.g., healing and prevention of diseases). Plants are known to have been used as source of medicines in almost all the ancient civilizations; and they still represent today an important reservoir of both traditional remedies and modern drugs.[1, 2] It is considered that ca. 80% of people around the world still rely on herbal remedies for their primary health care.[3-5]

However, unsustainable harvesting of medicinal plants has usually endangered or threatened some species with extinction.[6] This is for instance the case of the rhizomatous plant African ginger, i.e., *Siphonochilus aethiopicus* (Schweinf.) B.L. Burtt, in South Africa.[7] This highly prized plant is widely used in the South African traditional medicine to treat a number of ailments, such as asthma, colds, coughs, influenza and malaria.[8]

Overharvesting has unfortunately threatened the species with extinction to the point that it is being considered as scarce in the wild, and reported as locally extinct in some areas.[7, 9]

Although the micropropagation technique has been successfully applied using a tissue-culture based method followed by systematic cultivation in commercial nurseries to preserve the species from complete depletion,[7, 10, 11] the major concern on its use arises from traditional healers. They do not unanimously rely on African ginger rhizomes cultivated from cloned plants.[12]

To date no scientific studies have been reported to monitor the similarities and/or differences between the chemical profiles of wild crafted African ginger and cultivated clonal varieties.

Most reported studies focused on antimalarial,[13] antibacterial and antifungal,[14, 15] anti-inflammatory and anti-asthmatic activities,[16, 17] and were conducted on extracts prepared from dried plants. This was done without consideration that drying the plants may result in depletion of volatile ingredients, and that traditional use not only involves chewing of fresh rhizomes but includes inhalation of vapors from hot infusions.[16]

Understanding the chemical profiles of wild crafted and cultivated African ginger plants while taking into consideration the impact of drying processes on the composition of volatiles and plant ingredients, should result in a reliable and comprehensive benchmark for scientific studies which investigate

anecdotal effectiveness of African ginger, and further provide a useful background on the profile of the natural products contained in the plant.

Natural products (NPs) have provided humankind with a wide range of pharmacologically active drugs, e.g., the antiplasmodial artemisinin (**1**), the anti-inflammatory aspirin (**2**) and the anticancer taxol (**3**),[18-22] which have contributed to the management of and the fight against devastating diseases such as malaria. It is currently estimated that about 60 % of all drugs available on the market are somehow related to natural products.[1]

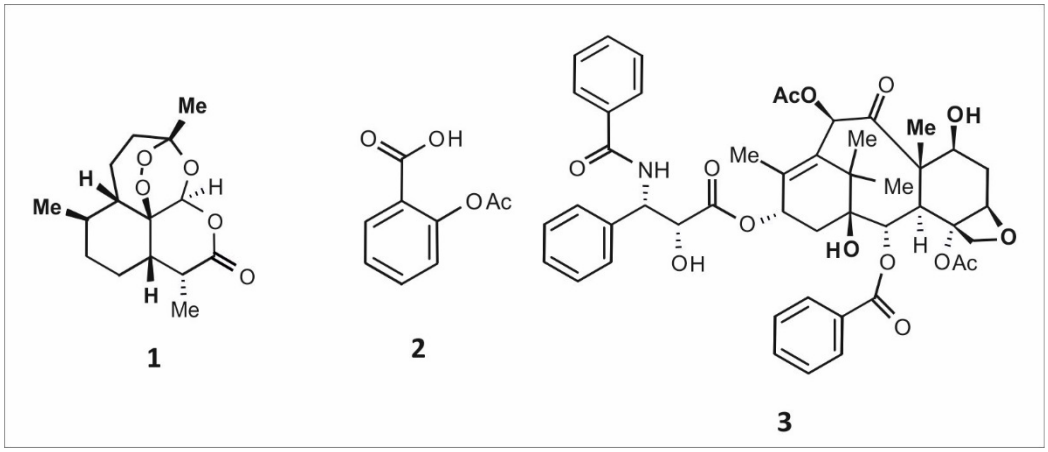

Figure 1.1: Structures of artemisinin (**1**), aspirin (**2**) and taxol (**3**).

In recent times, research of bioactive NPs (i.e., isolation, characterization and structure elucidation) has reached considerably high interest in organic chemistry and related sciences. Investigation of new drug leads and development of new drug candidates against sicknesses such as tropical infectious diseases (e.g., malaria, leishmaniasis and trypanosomiasis) have given rise to an unprecedented ethnobotanical and chemo-taxonomical exploration of medicinal plants.[23, 24] These have recently led to the isolation of highly interesting chiral naphthylisoquinoline alkaloids (NIQ), limonoids and diterpenoids, from a newly discovered but as yet undescribed Congolese *Ancistrocladus* species, a Thai and an Indian mangrove.[25-27]

Based on the fact that chirality in molecules leads to the existence of enantiomers (i.e., mirror-image but not superimposable compounds), which sometimes obviously result in ambivalent bioactivities,[28-30] the investigation of the absolute configuration of NPs is usually a relevant task especially since its knowledge directs the establishment of adequate synthetic routes, and guides the understanding of biosynthetic pathways.

As part of this study absolute configurations of two unsymmetrical dimeric NIQ atropo-diastereomers, two limonoids and one diterpenoid were targeted by conducting quantum-chemical calculations of the circular dichroism chiroptical behavior.[31, 32]

References

[1] D. J. Newman, *J. Med. Chem.* **2008**, *51*, 2589-2599.

[2] D. J. Newman, G. M. Cragg, *J. Nat. Prod.* **2012**, *75*, 311-335.

[3] J. K. Borchardt, *Drug News Perspect.* **2002**, *15*, 187-192.

[4] A. Gurib-Fakim, *Mol. Aspects Med.* **2006**, *27*, 1-93.

[5] C. S. Patch, *Med. J. Aust.* **2006**, *185*, S1-S24.

[6] J. W. Li, J. C. Vederas, *Science* **2009**, *325*, 161-165.

[7] N. Crouch, M. Lotter, S. Krynauw, C. Pottas Bircher, *Herbertia* **2000**, *55*, 115-129.

[8] C. W. Holzapfel, W. Marais, P. L. Wessels, B. Van Wyk, *Phytochemistry* **2002**, *59*, 405-407.

[9] V. Williams, J. Victor, N. Crouch, *S. Afr. J. Bot.* **2013**, *86*, 23-35.

[10] N. Crouch, R. Symmonds, *Plantlife* **2002**, *26*, 19-20.

[11] G. L. Ngwenya, N. Moodley, M. E. Nemutanzhela, B. G. Crampton, *S. Afr. J. Bot.* **2010**, *76*, 414.

[12] T. Z. Manzini, MSc dissertation, University of Pretoria (South Africa), **2005**.

[13] C. A. Lategan, W. E. Campbell, T. Seaman, P. J. Smith, *J. Ethnopharmacol.* **2009**, *121*, 92-97.

[14] M. Light, L. McGaw, T. Rabe, S. Sparg, M. Taylor, D. Erasmus, A. Jäger, J. Van Staden, *S. Afr. J. Bot.* **2002**, *68*, 55-61.

[15] R. Coopoosamy, K. Naidoo, L. Buwa, B. Mayekiso, *J. Med. Plant Res.* **2010**, *4*, 1228-1231.

[16] G. Fouche, S. van Rooyen, T. Faleschini, *Int. J. Genuine Trad. Med.* **2013**, *3*, 24-29.

[17] G. Fouche, N. Nieuwenhuizen, V. Maharaj, S. van Rooyen, N. Harding, R. Nthambeleni, J. Jayakumar, F. Kirstein, B. Emedi, P. Meoni, *J. Ethnopharmacol.* **2011**, *133*, 843-849.

[18] G. A. Balint, *Pharmacol. Ther.* **2001**, *90*, 261-265.

[19] R. N. Price, *Expert Opin. Investig. Drugs* **2000**, *9*, 1815-1827.

[20] J. G. Mahdi, *J. Saudi Chem. Soc.* **2010**, *14*, 317-322.

[21] G. M. Cragg, P. G. Grothaus, D. J. Newman, *Chem. Rev.* **2009**, *109*, 3012-3043.

[22] M. Suffness, *Annu. Rep. Med. Chem.* **1993**, *28*, 305-314.

[23] A. Ghorbani, F. Naghibi, M. Mosaddegh, *Iran. J. Pharm. Sci.* **2006**, *2*, 109-118.

[24] D. Kong, X. Li, H. Zhang, *Drug Discov. Today* **2009**, *14*, 115-119.

[25] G. Bringmann, B. K. Lombe, C. Steinert, K. N. Ioset, R. Brun, F. Turini, G. Heubl, V. Mudogo, *Org. Lett.* **2013**, *15*, 2590-2593.

[26] J. Li, M. Li, T. Bruhn, F. Z. Katele, Q. Xiao, P. Pedpradab, J. Wu, G. Bringmann, *Org. Lett.* **2013**, *15*, 3682-3685.

[27] H. Wang, M. Li, F. Z. Katele, T. Satyanandamurty, J. Wu, G. Bringmann, *Beilstein J. Org. Chem.* **2014**, *10*, 276-281.

[28] J. McConathy, M. J. Owens, *Prim. Care. Companion J. Clin. Psychiatry* **2003**, *5*, 70-73.

[29] C. Sánchez, *Basic Clin. Pharmacol. Toxicol.* **2006**, *99*, 91-95.

[30] J. Najib, *Clin. Ther.* **2006**, *28*, 491-516.

[31] G. Bringmann, T. A. Gulder, M. Reichert, T. Gulder, *Chirality* **2008**, *20*, 628-642.

[32] G. Bringmann, T. Bruhn, K. Maksimenka, Y. Hemberger, *Eur. J. Org. Chem.* **2009**, *17*, 2717-2727.

Chapter 2

Chemical profiling of cultivated and wild African ginger, *Siphonochilus aethiopicus* (Schweinf.) B.L. Burtt

2.1. Introduction

African ginger is a rhizomatous plant restricted to savanna regions of tropical and southern Africa.[1, 2] It is a member of the Zingiberaceae family and was once widespread in countries like Malawi, Zambia, Zimbabwe and South Africa.[3, 4]

It is well-known and commonly employed in the South African traditional medicine for its therapeutic benefits and is usually quoted as one of the most popular medicinal plants sold in the Durban muthi markets.[5] Its rhizomes are either chewed fresh, used to prepare cold or hot infusions and inhalation of vapors from hot infusions for the treatment of mild asthma, colds and influenza.[6]

Prolonged harvesting has unfortunately threatened the plant with extinction[7-9] and according to its red list status which is CR A4acd, African ginger is critically endangered and face an extreme risk of extermination in the wild.[9]

Tissue culture micropropagation at both the Kirstenbosch and Durban Botanic Gardens in South Africa[10] which aimed at rescuing the plant from total extinction, has played a vital role in the conservation of the species. Presently micropropagated plants are available in a number of commercial nurseries and are being cultivated on a small scale in several locations in South Africa.[11]

2.2. Botanical description, ethnobotany, cultivation and pharmacochemistry

The scientific designation of African ginger is *Siphonochilus aethiopicus* and this refers to both the shape of the flowers and the geographic origin of the plant. While the greek words "*Siphono*" and "*chilus*" meaning respectively tube and lip, morphologically describe the flowers which are funnel-shaped, the word "*aethiopicus*" mentions the African origin of the plant.[12]

African ginger (**Figure 2.1**) is also known as wild ginger (in English), wildegemmer (in Afrikaans), indungulo or isiphephetho (in Zulu). *Kaempferia aethiopica* (Schweinf.) Benth. and *Cienkowskia aethiopica* Schweinf. are few common botanical synonyms.[1, 8, 10]

It is usually described as "*a deciduous forest floor plant with large, hairless leaves that annualy develop from a cone-shaped rhizome*".[3]

Figure 2.1 : Rhizome of African ginger with fresh tuberous roots (private photo).

It has attractive trumpet-like white, yellow and mauve flowers that emerge in spring directly from the underground rhizomes which smell like real ginger, *Zingiber officinale*.[3, 8] The flowers often raise before the leaves which are depicted as "*light green and lance shaped*".[12]

Most plants are hermaphroditic, and have larger flowers than the females equivalent. Fruits are berry-like and mature below or above the ground.[3, 8]

African ginger is easily cultivated, provided it is given adequate conditions[12] such as "*loose, friable and well-drained soils*" with high water holding capacity.[8]

Propagation is easily done by vegetative multiplication (splitting and replanting of dormant rhizomes) and by tissue culture micropropagation.[8, 13]

Mono and sesquiterpenoids present in the volatile oil have been usually considered to be the active ingredients of the plants.[10]

Two sesquiterpenoids, the furanoterpenoid (**4**) and the hydroxyfuranoterpenoid (**5**) and their relative stereochemistry were reported after steam distillation of fleshy crushed roots.[4] Three additional sesquiterpenoid lactones, compounds (**6**), (**7**) and (**8**), were purified from an ethylacetate extract of dried and powdered rhizomes and their relative stereochemistry were reported.[14]

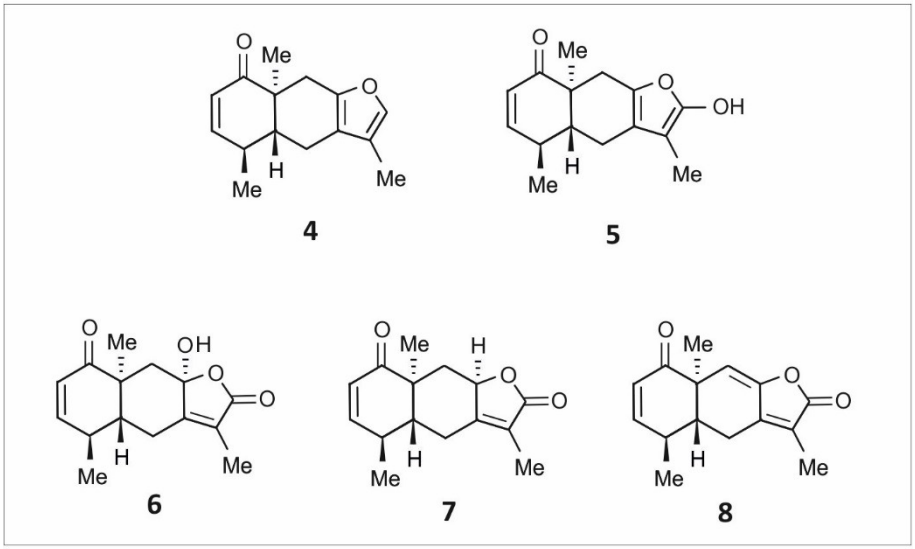

Figure 2.2: Sesquiterpenoids reported from African ginger (only one stereo-isomer shown).

Ethanolic and ethylacetate extracts were reported to exhibit antibacterial activity against a number of both Gram-positive and negative bacteria such as *Bacillus subtilis*, *Staphyloccus aureus*, *Escherichia coli* and *Klebsiella pneumoniae*.[15]

The composition of the essential oil from the roots and rhizomes is reported to contain 1,8 cineole (eucalyptol), (*E*)-β-ocimene, *cis*-allocimene and a sesquiterpenoid of furanoid type.[16]

A number of dried organic extracts revealed anti-inflammatory and immuno suppressent activities *in vitro* using NF-kβ transcription response and a cytokine assay.[6]

The study reported in this chapter aims at investigating qualitative similarities and/or differences between the chemical profiles of dried and extracted wild and cultivated African ginger plants and assessing the impact of the drying processes on the composition of selected volatile compounds. The latter *viz*. the drying process, impacts on the analysis of the wild and cultivated plants.

2.3. Rational and motivation

A study that aimed at estimating the genetic diversity within a natural population of African ginger and individuals cloned for commercial purposes, noted a wide genetic variation in the wild population and almost none for the cultivated plants sampled.[17]

From a survey in Mpumalanga villages, divergences among traditional healers on using wild or cultivated African ginger have been reported and noted that about half of the practitioners interviewed rely on wild material.[18]

Based on the knowledge that genetic variations and other factors may quantitatively and/or qualitatively affect the chemistry of secondary metabolites in a plant and thus the bioactivity,[19, 20] investigation of the chemical profiles of wild rhizomes and individuals cultivated from cloned plants became relevant for a clear and conclusive assessment of similarities and/or differences.

2.4. Objectives

2.4.1. General objectives

The general objectives are as follows:

- Qualitative investigation of similarities and/or differences between the chemical profiles of wild and cultivated plants of African ginger;
- Monitoring the impact of drying the plant on the chemical profiles, as well as the composition of selected volatiles;
- Assessment of the antimalarial activity of extracts produced from the wild and cultivated rhizomes.[1]

2.4.2. Specific objectives

- Preparation of organic extracts for chemical analyses and biological screening (antiplasmodial test);
- Isolation, purification and structural elucidation of relevant compounds to produce pure chemical standards;
- Investigation of the chemical fingerprints (i.e., chemical profiles) of extracts from wild and cultivated rhizomes of African ginger, using the UPLC MS and GC MS techniques;
- Assessment of the similarities and differences between the chemical profiles of wild and cultivated African ginger, based on the comparison of the related profiles;
- Evaluation of the impact of the drying processes on the chemical compounds in general, and the volatiles in particular;

[1] The antiplasmodial bioassay was selected because the plant is reported to be used for malaria.

- Investigation of the antimalarial activity of extracts from wild and cultivated plants of African ginger on the chloroquine-sensitive (CQS) strains of *Plasmodium falciparum* (NF54).

2.5. Theoretical framework

Chromatographic methods such as the hyphenated UPLC MS and GC MS should separate compounds/metabolites within the extracts based on the difference between their affinity with both the stationary and the mobile phase and then elute in the form of chromatograms.

Based on the assumption that the metabolites common to the wild and the cultivated African ginger will elute at the same retention time (RT) and show same properties (in this case the MS and MS/MS fragmentation pattern), assessment of qualitative similarities and differences should be feasible from the comparison of their related chromatograms.

Matching MS and MS/MS experimental data with that published in databases such as the Dictionary of Natural Products (DNP 24.1) and the National Institute of Standards and Technology library (NIST08) as well as information reported in the literature of known compounds should provide information for the identification of compounds in the UPLC MS and GC MS profiles.

Comparison of GC MS profiles of extracts from fresh rhizomes and dried rhizomes should reveal the impact of the drying processes on the volatile compounds.

2.6. Hypothesis

Secondary metabolites of African ginger can be extracted based on the polarity using appropriate organic solvents or solvent mixtures.

A suitable gradient elution with chromatographic methods should provide a conclusive separation of the compounds present in the extracts and afford reliable chemical fingerprints of the extracts.

Compounds present in the profiles should be identifiable based on matching the experimental data with that reported in the literature and database, and comparison with authentic pure compounds.

The similarities and differences between the chemical profiles of wild and cultivated African ginger can be monitored directly through the comparison of their related chromatograms.

2.7. Methodology

The work herein reported was achieved by conducting the following steps:

- Air and oven drying of the wet rhizomes;
- Grinding of dried rhizomes;
- Solvent extraction of powdered rhizomes;
- Isolation, purification and structure elucidation of relevant compounds.
- UPLC MS and GC MS analysis of the extracts;
- Qualitative evaluation of similarities and/or differences between the chemical profiles of extracts from wild and cultivated plants;
- Assessment of the impact of drying processes on volatiles based on GC MS results;
- Antimalarial screening of the extracts from wild and cultivated plants.

2.8. Material and methods

2.8.1. Material

Analytical and technical grade solvents were supplied by Merck and Radchem. Thin layer chromatography was performed on Merck silica gel 60 F_{254} plates which were later visualized with either iodine or 254 and 366 nm UV lights; column chromatography was performed on Merck silica gel 60 (0.063-0.20 mm).

Ultra performance liquid chromatography profiling was accomplished with an Acquity UPLC, coupled to a Waters Synapt G2 QTOF mass spectrometer using an electrospray ionization (ESI) technique operating in positive or negative modes. Experiments were performed with an Acquity UPLC BEH C18 1.7 µm 2.1 x 100 mm column from Waters. LC MS chromatograms were processed and visualized using the MassLynx v.4.1 software.

GC MS experiments were conducted on a LECO Pegasus 4D GC TOF MS with an Agilent 7890 gas chromatograph, on an apolar Rxi-5SilMS 30 m x 0.25 mm x ID x 0.25 µm df capillary column.

NMR data were recorded on a Bruker Avance III 400 MHz magnet operating at 400.21 MHz for ^{1}H and 100.64 MHz for ^{13}C. Chemical shifts are reported in ppm, *J* coupling constants in hertz (Hz) and the

multiplicity of ^{1}H peaks are denoted with corresponding letters in italic (e.g., *s*: singlet, *d*: doublet, *dd*: doublet of doublets, *t*: triplet, *m*: multiplet, etc.).

X-ray diffraction experiments were realized on a Bruker D8 Venture diffractometer, using a Cu Kα source and a Photon 100 detector.

All the varieties of African ginger used were received from the department of Enterprise Creation and Development at the CSIR. Fresh rhizomes were harvested from cultivation sites in Giyani, Limpopo Province, South Africa, and are of tissue culture origin based on personal communication by the CSIR, which confirmed that the cultivation site in Giyani utilized tissue cultured material originating from KZN and Mpumalanga, South Africa. These two sources of tissue cultured plants were propagated separately in Giyani. The wild plants were collected from the Faraday muthi market, which according to the sellers and the literature are of the wild type.[21] All sample were collected in different seasons.

A voucher specimen for identification could not be deposited due to a few reasons. The leaves, flowers and fruits which are required for this purpose were not available from the cultivation site in Giyani, Limpopo. In addition to the fact that only fresh rhizomes were received from the CSIR, the major reasons were the scarcity of the plant in the wild, the unavailability of fruits, as these mature underground and are difficult to find and the brief seasonal flowering of African ginger.

However, the cultivated and wild plants were confirmed to be African ginger based on personal communication from the CSIR which supplied the plants; and further support came from morphological and olfactory inspections as the rhizomes and the fragrances were characteristic of African ginger.

2.8.2. Methods

2.8.2.1. Drying and extraction methods

Fresh rhizomes from all collections were cut into 1-2 mm slices and portions were left to dry separately in a fume hood and an oven set at 60 °C for approximately 11 days.

The dried rhizomes were ground into fine powder using a coffee grinder.

Extracts for UPLC MS analysis were prepared by stirring overnight 10g of the powder in 100 ml of n-hexane/DCM (1:1) followed by filtration and evaporation of the solvent using a Büchi rotary evaporator.

Extracts for GC MS analysis were prepared by stirring 5g of the dried powder or the ground fresh rhizomes in 50 ml of n-hexane for 2 hours followed by filtration. The n-hexane extracts were analysed by GC MS without evaporation of the solvent.

2.8.2.2. Fractionation, isolation, purification and structure elucidation

Two fractionation steps led to the isolation of the furanoterpenoid (**4**) and the hydroxylactone (**6**) from dried and powdered wild plants, and were both conducted on a silica gel stationary phase, as illustrated in the following flowchart.

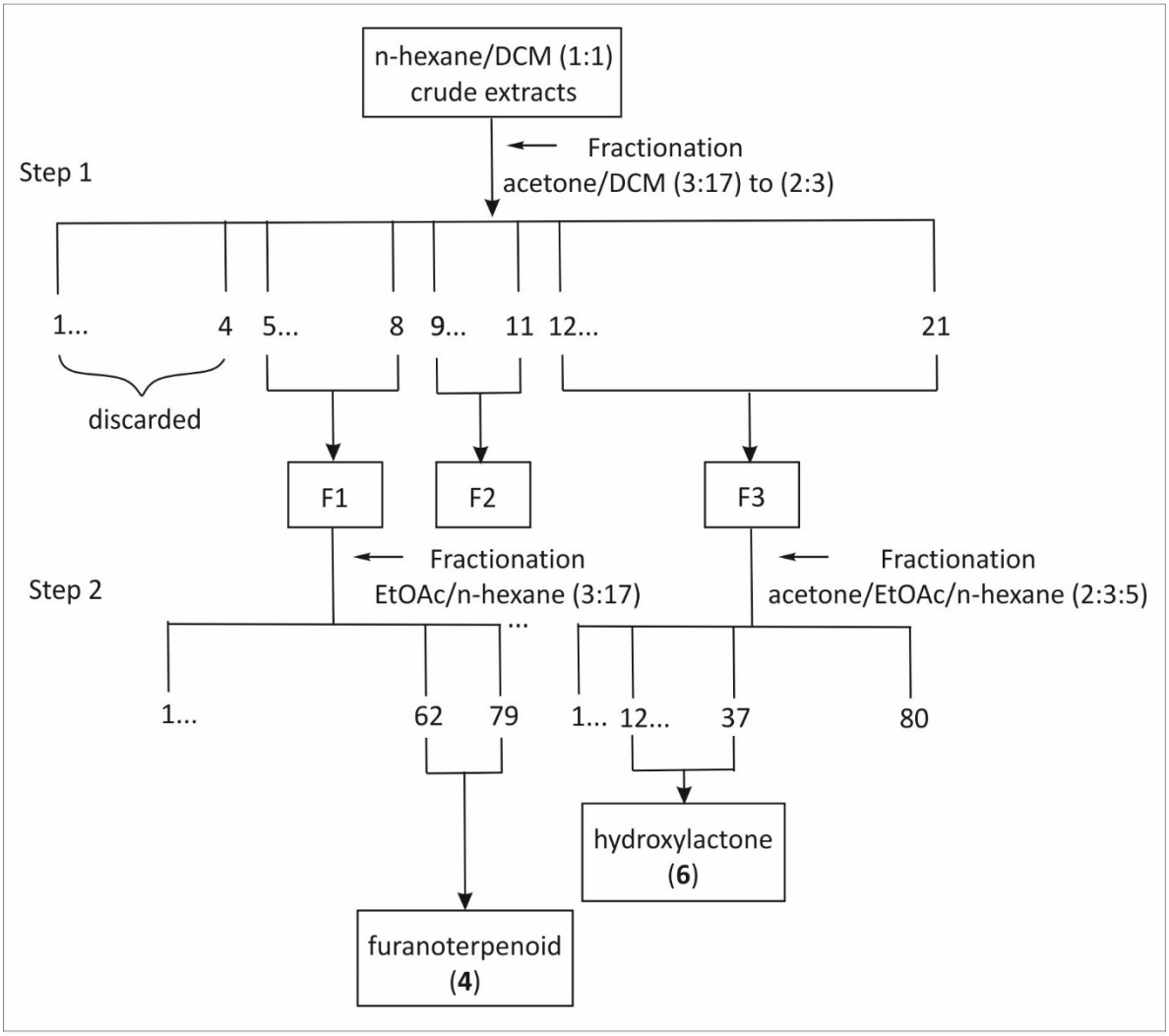

Scheme 2.1: Flowchart toward isolation of the furanoterpenoid (**4**) and the hydroxylactone (**6**).

n-Hexane/DCM (1:1) crude extracts (0.565 g) were first fractionated by gradient elution, starting with acetone/DCM (3:17) and progressively increasing up to acetone/DCM (2:3). A total of 21 fractions of

50 ml each were collected, analyzed by TLC and grouped accordingly. TLC plates were developed with acetone/DCM (1:9) and alternately visualized with iodine and both 254 and 366 nm UV lights.

Fractions 5 to 8 were combined to afford F1, fractions 9 to 11 gave F2 and all the remaining ones yielded F3. Fractions 1 to 4 were discarded, as they did not show any spots on TLC plates.

The second purification step involved further fractionation of F1 and F3. F2 was not considered since the related TLC plate showed the combination of the same spots as those present in both F1 and F3.

The fractionation of F1 with silica gel column chromatography was conducted using an isocratic elution with EtOAc/n-hexane (3:17) and afforded 80 sub-fractions of 10 ml each. The sub-fractions were analyzed by TLC using EtOAc/hexane (3:7), and the visualization of the plates was done using UV lamps and an iodine chamber. The sub-fractions 62 to 79 were mixed and concentrated with a Büchi rotary evaporator to afford F1a. Overnight crystallization of F1a afforded the furanoterpenoid (**4**) as a colorless crystalline compound.

F3 was further fractionated using silica gel column chromatography and an isocratic elution with the mixture acetone/EtOAc/n-hexane (2:3:5). A total of 80 sub-fractions of 8 ml each were collected and analyzed by TLC using acetone/EtOAc/n-hexane (2:3:5). The plates were visualized with an iodine chamber. Based on TLC profiles, sub-fractions 12 to 37 were pooled and concentrated using a Büchi rotary evaporator resulting in the hydroxylactone (**6**) as colorless crystals.

Structure elucidation of the furanoterpenoid (**4**) and the hydroxylactone (**6**) was successfully achieved with ^{1}H, ^{13}C, DEPT-135, HSQC, HMBC, COSY and NOESY NMR experiments, using either CD_2Cl_2 or $CDCl_3$ deuterated solvents; and was independently corroborated by single crystal X-ray diffractions (see appendix).

2.8.2.3. UPLC MS analysis and profiling method

The dried n-hexane/DCM (1:1) extracts, as well as the analyzed pure compounds, were made up to 1 mg ml^{-1}, using a (1:1) mixture of 1% formic acid in deionized water (solvent A) and 1% formic acid in acetonitrile (solvent B). The injection volume was 3 µl with a flow rate of 0.30 ml min^{-1} and a run time of 60 minutes.

TOF MS data were acquired in the range of 100-1200 atomic mass units (amu) for a scan time of 0.5 seconds, using the electrospray positive and negative ionization mode (ESI+ and ESI-). The cone voltage was ramped from 20 to 40 V.

A linear gradient system was used for the UPLC separation as shown in **Table 2.1**, consisting of 1% formic acid in deionized water (Solvent A) and 1% formic acid in acetonitrile (solvent B).

Table 2.1: Gradient method used for UPLC MS analysis.

Time (min)		Flow (ml min^{-1})	Solvent A (%)	Solvent B (%)
1.	initial	0.30	95.00	5.00
2.	2.00	0.30	95.00	5.00
3.	30.00	0.30	1.00	99.00
4.	40.00	0.30	1.00	99.00
5.	45.00	0.30	95.00	5.00
6.	60.00	0.30	95.00	5.00

2.8.2.4. GC MS method

The GC runtime was 35.9 minutes and the method was performed exclusively on n-hexane extracts. The flow rate of the helium carrier gas was set up at 1.40 ml min^{-1} in the constant flow mode and the injection volume was of 1 µl. The GC inlet was maintained at 225 °C and was operated either in splitless mode or in the split mode (50:1 split ratio). The GC oven temperature program was 40 °C (0.9 min) at 8 °C min^{-1} to 280 °C (5 min). The MS transfer line temperature was set up at 280 °C and the ion source temperature at 200 °C. The electron energy was 70 eV in the electron impact ionization mode (EI+), the data acquisition rate was 10 spectra s^{-1}, the mass acquisition range was 40-500 atomic mass units (amu), and the detector voltage was set at 1650 V. Linear retention indices were calculated based on the analysis from C-10 to C-22 n-alkanes, using the Van den Dool and Kratz method.[22]

2.8.2.5. Antimalarial screening

The anti-malarial screening of n-hexane/DCM (1:1) extracts was done in collaboration with the Division of Pharmacology, University of Cape Town, South Africa.

The test samples were tested in triplicate against chloroquine-sensitive (CQS) strain of *Plasmodium falciparum* (NF54). Continuous *in vitro* cultures of asexual erythrocyte stages of *P. falciparum* were maintained using a modified method of Trager and Jensen.[23] Quantitative assessment of antiplasmodial activity *in vitro* was determined *via* the parasite lactate dehydrogenase assay using a modified method described by Makler.[24]

The test samples were prepared to a 20 mg ml^{-1} stock solution in DMSO. Samples were tested as a suspension if not completely dissolved. Stock solutions were stored at -20 °C. Further dilutions were prepared on the day of the experiment. Chloroquine (CQ) and artesunate were used as the reference drugs in all experiments. A full dose-response was performed for all compounds to determine the concentration inhibiting 50 % of parasite growth (IC_{50} value). Test samples were tested at a starting concentration of 100 µg ml^{-1}, which was then serially diluted 2-fold in complete medium to give 10 concentrations; with the lowest concentration being 0.2 µg ml^{-1}. The same dilution technique was used for all samples. Reference drugs were tested at a starting concentration of 1000 ng ml^{-1}. The highest concentration of solvent to which the parasites were exposed to had no measurable effect on the parasite viability (data not shown). The IC_{50}-values were obtained using a non-linear dose-response curve fitting analysis via Graph Pad Prism v.4.0 software.

2.9. Results and discussion

2.9.1. Extraction

The extraction yields after overnight stirring of 10g powders of both air-dried and oven-dried rhizomes in 100 ml n-hexane/DCM (1:1) are shown in **Table 2.2**.

Table 2.2: n-Hexane/DCM (1:1) extraction yields of powdered rhizomes.

African ginger plants	Extract yield[a] (% w/w)	Extract yield[b] (% w/w)
Wild	5.65	5.70
KZN [c]	1.73	1.40
Mpumalanga [c]	1.66	1.88

[a] *air-dried rhizomes*

[b] *oven-dried rhizomes*

[c] *cultivated plants*

The extraction yields (**Table 2.2**) revealed a higher biomass for the wild plants, ca. three times that of the KZN and Mpumalanga cultivated varieties possibly due to high concentrations of the metabolites they contain compared to the cultivated equivalent. This was the first notable difference that could be established between the wild and cultivated plant samples.

2.9.2. Isolation, purification and structure elucidation

Thin layer chromatography (TLC) of the 21 fractions collected after fractionation of the n-hexane/DCM (1:1) crude extracts (see **section 2.8.2.2**) revealed 8 relevant spots on silica gel TLC plates, which were developed with acetone/DCM (1:9). The R_f values of the spots observed were 0.93, 0.86 (most intense spot), 0.78, 0.67, 0.58, 0.53, 0.22 and 0.16.

The most intense spot (R_f 0.86) was assumed to be the major compound reported in literature[4] and was targeted for isolation. Fractions 5 to 8 were combined and labelled F1, as their TLC profiles showed them to contain mainly the supposed major compound. The combination of fractions 9 to 11 were labelled as F2 and that of 12 to 21 labelled F3.

Purification of F1, using column chromatography and elution with EtOAc/n-hexane (3:17), resulted in 80 sub-fractions. TLC analysis developed with EtOAc/hexane (3:7) revealed the presence of an intense spot (R_f 0.68) for the sub-fractions 62 to 79 which were combined and concentrated with a Büchi rotary evaporator. Overnight crystallization in the remaining solvent afforded a colorless crystalline compound which through mass spectrometry, NMR and X-ray diffraction was confirmed to be the furanoterpenoid (**4**) (14.51%).

Time of flight mass spectrometry, using electrospray ionization in positive mode (TOF MS ES+) gave a $[M+H]^+$ with m/z 231.1389 which through MassLynx v.4.1 was calculated to have the molecular formula $C_{15}H_{18}O_2$.

^{13}C and DEPT-135 NMR investigations in CD_2Cl_2 revealed a keto carbonyl (δ_C 204.16), three methyl groups (δ_C 18.92, 16.78 and 8.19), two methylene groups (δ_C 32.30 and 22.83), five methine groups (δ_C 154.76, 137.76, 126.70, 45.32 and 34.64) and four quaternary carbons (δ_C 149. 61, 119.63, 115.32 and 45.25).

^1H NMR experiments in CD_2Cl_2 showed three characteristic olefinic methine protons (δ_H 7.07, *m*; δ_H 6.71, *dd* and δ_H 5.91, *dd*). *J* coupling constants are reported in **Table 2.3**.

^1H and ^{13}C NMR data, as well as relevant HMBC correlations are summarized in **Table 2.3** where the atoms are numbered as shown in **Figure 2.3**.

Table 2.3: ^{1}H, ^{13}C and HMBC data of the furanoterpenoid (**4**) in CD_2Cl_2.

H atoms	δ_H (ppm)	δ_H litt.[Γ]	Multiplicity [*J* (Hz)]	HMBC	C atoms	δ_C (ppm)	δ_C Litt.[Γ]
2	7.07	7.02	*m*	-	2	137.76	137.5
-	-		-	-	3	119.69	119.0
-	-		-	-	3a	115.32	114.6
4a	1.85	1.81	*ddd* (10.9, 9.9, 5.4)	C-4, C-5, C-8a, 8a-Me	4a	45.32	45.0
4*eq* *	2.73	2.68	*ddd* (15.9, 5.4, 1.8)	C-3a, C-4a, C-9a	4	22.83	22.5
4*ax* *	2.16	2.12	*dddd* (15.9, 11.0, 3.1, 1.7)	3-Me			
5	2.44	2.40	*m*	-	5	34.64	34.2
6	6.71	6.66	*dd* (10.1, 2.2)	C-4a, C-5, C-8, 5-Me	6	154.76	154.2
7	5.91	5.91	*dd* (10.1, 2.8)	C-5	7	126.70	126.6
-	-		-	-	8	204.16	204.0
-	-		-	-	8a	45.25	44.9
9*eq* *	2.71	2.73	*dd* (16.8, 1.7)	C-3a, C-4a, C-9a, 8a-Me	9	32.30	31.9
9*ax* *	2.63	2.64	*br d* (16.8)	C-9a, 8a-Me	-		
-	-		-	-	9a	149.61	149.3
3-Me	1.94	1.90	*d* (1.3)	C-2, C-3, C-3a	3-Me	8.19	8.1
5-Me	1.23	1.21	*d* (7.2)	C-4a, C-5, C-6	5-Me	18.92	18.7
8a-Me	1.04	1.02	*s*	C-4a, C-8, C-9	8a-Me	16.78	16.6

eq: equatorial

ax: axial;

** maybe interchangeable (only the relative structure is reported);* [Γ] *NMR data in $CDCl_3$* [4]

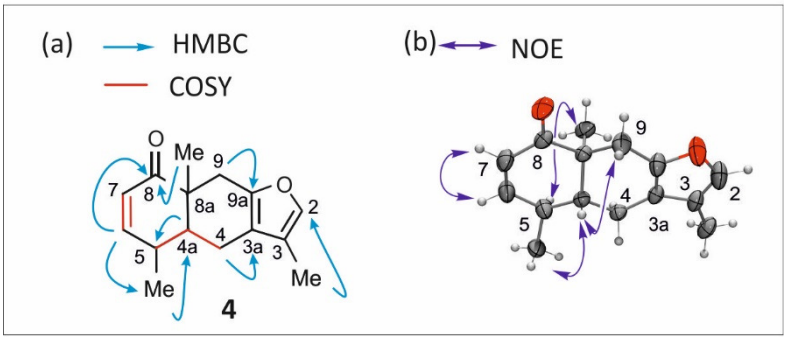

Figure 2.3: (a) Selected HMBC and ^{1}H-^{1}H COSY correlations (b) selected NOE interactions for the furanoterpenoid (**4**).

HMBC correlations between the methine H-6 (δ_H 6.71) and the keto carbonyl at C-8 (δ_C 204.16), and the strong COSY correlation between the H-6 (δ_H 6.71) and H-7 (δ_H 5.91) methine protons revealed the keto carbonyl at C-8 to be α,β unsaturated (**Figure 2.3**).

8a-Me (δ_C 16.78) and 5-Me (δ_C 18.92) locations were assigned based on their respective HMBC correlations with the carbons at C-6 (δ_C 154.76) and C-8 (δ_C 204.16) and were assumed to adopt opposite spatial orientations based on the lack of NOE interactions between them.

With 8a-Me and 5-Me adopting α and β configurational relationship, the spatial distance between them will increase and this will lower all possibilities of through space NOE interactions, which results in the absence of NOESY correlations as observed for the furanoterpenoid (**4**).

Based on mutual HMBC correlations between their related protons and carbons, the methylene carbon C-4 (δ_C 22.83) was linked to the methine C-4a (δ_C 45.32), which itself was attached to the methine C-5 (δ_C 34.64) as their protons and carbons were correlating through HMBC. The methylene C-9 (δ_C 32.30) was attached to the quaternary C-8a (δ_C 45.25), based on the fact that the protons at C-9 and the carbon of 8a-Me (attached to C-8a) were correlating through HMBC. Further HMBC correlations of the methylene protons at C-4 and C-9 revealed C-4 and C-9 to be respectively attached to the quaternary carbons C-3a (δ_C 115.32) and C-9a (δ_C 149.61) which were established as part of a methylated furan ring.

Single crystal X-ray crystallography validated the established relative configuration, and additionally confirmed 8a-Me and 5-Me to be located in opposite spatial regions (**Figure 2.3**).

Further fractionation of F3 on a silica gel column, using acetone/EtOAc/n-hexane (2:3:5) generated 80 sub-fractions. TLC analysis after developing the plate with acetone/EtOAc/hexane (2:3:5) revealed two spots in sub-fractions 12 to 37 with the R_f values of 0.48 (intense) and 0.37. These sub-fractions 12 to 37 were combined and concentrated using a Büchi rotavapor to almost dryness. Crystallization from the remaining solvent gave colorless crystals which were left to grow overnight and filtrated under vacuum thereafter.

Mass spectrometry, NMR and X-ray diffraction experiments revealed the crystalline compound to be the hydroxylactone (**6**) (4.74%).

Time of flight mass spectrometry, using the electrospray negative ionization mode (TOF MS ES-) revealed a $[M-H]^-$ parent peak at m/z 261.1120, which afforded the molecular formula of $C_{15}H_{18}O_4$ (mass calculated 261.1127).

TOF MS ES+ suggested the presence of a molecular ion with the loss of a hydroxyl functional group, as an abundant base peak with m/z 245.1180 $[M+H-H_2O]^{+\cdot}$.

The presence of the hydroxyl group was also confirmed with ^{1}H NMR experiments in $CDCl_3$, which revealed a characteristic OH singlet (δ_H 4.08).

^{13}C NMR experiments displayed 15 signals of which two were assigned to a keto group (δ_C 202.85) and a lactone carbonyl (δ_C 172.07), three were attributed to methyl groups (δ_C 18.14, 16.68 and 8.24), two were allocated to methylene groups (δ_C 24.13 and 43.69), four were ascribed to methine groups (δ_C 153.57, 126.09, 33.82 and 49.93) and four resulted from quaternary carbons (δ_C 158.47, 122.39, 103.48 and 44.88).

Full ^{1}H and ^{13}C NMR data as well as relevant HMBC correlations are reported in **Table 2.4** where atoms are numbered based on the relative structure of the hydroxylactone (**6**).

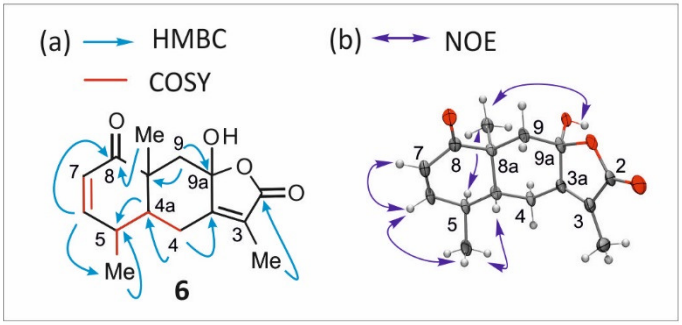

Figure 2.4: (a) Selected HMBC and ^{1}H-^{1}H COSY correlations (b) selected NOE interactions for the hydroxylactone (**6**).

Strong COSY correlations between the methine hydrogens H-6 (δ_H 6.63) and H-7 (δ_H 5.85) and HMBC between H-6 and the C-8 carbonyl (δ_C 202.85) revealed the carbonyl C-8 to be α,β unsaturated (**Figure 2.4**).

The location of 8a-Me (δ_C 16.68) was deduced based on HMBC correlations between the respective protons with the carbonyl at C-8 (δ_C 202.85) and for 5-Me (δ_C 18.14) with both the methine carbons at C-5 (δ_C 33.82) and C-6 (δ_C 153.57). The lack of NOESY correlations between methyl protons proposed their relative spatial arrangement to be opposite.

The methylene C-4 (δ_C 24.13) was assigned based on HMBC correlations between its protons (δ_H 2.81 and 2.38) and the methine C-4a (δ_C 49.93). HMBC correlation between the protons of the methylene C-9 (δ_C 43.69) and both the quaternary carbons C-8a (δ_C 44.88) and C-9a (δ_C 103.48) indicated that C-9 was bonded to both C-8a and C-9a.

Table 2.4: ^{1}H, ^{13}C and HMBC data of the hydroxylactone (**6**) in $CDCl_3$.

H atoms	δ_H (ppm)	δ_H Litt.[Γ]	Multiplicity [*J* (Hz)]	HMBC	C atoms	δ_C (ppm)	δ_C Litt.[Γ]
-	-		-	-	2	172.07	171.6
-	-		-	-	3	122.39	122.4
-	-		-	-	3a	158.47	160.1
4a	1.56	1.62	*ddd* (13.3, 10.0, 3.6)	8a-Me	4a	49.93	51.1
4*eq* *	2.81	2.90	*dd* (13.5, 3.6)	C-3, C-4a, C-8a, C-9a	4	24.13	25.3
4*ax* *	2.38	2.36	*m*	C-3, C-3a, C-4a			
5	2.48	2.53	*dqt* (9.7, 7.1, 2.4)	-	5	33.82	35.3
6	6.63	6.74	*dd* (10.1, 2.0)	C-4a, C-5, C-8, 5-Me	6	153.57	156.0
7	5.85	5.81	*dd* (10.1, 2.7)	C-5	7	126.09	126.8
-	-		-	-	8	202.85	204.3
-	-		-	-	8a	44.88	46.4
9*eq* *	2.64	2.49	*d* (14.5)	C-3a, C-4a, C-8a, C-9a	9	43.69	44.8
9*ax* *	1.65	1.60	*d* (14.5)	C-9a, C-8a, 8a-Me			
-	-		-	-	9a	103.48	104.5
9a-OH	4.08	4.84	*s*	-			
3-Me	1.79	1.78	*d* (1.4)	C-2, C-3, C-3a	3-Me	8.24	8.9
5-Me	1.22	1.22	*d* (7.1)	C-4a, C-5, C-6	5-Me	18.14	18.9
8a-Me	1.33	1.30	*s*	C-4a, C-8, C-8a	8a-Me	16.68	17.8

eq: equatorial

ax: axial

**maybe interchangeable (only the relative structure is reported),* [Γ] *solvent used not specified*[14]

HMBC correlation between the methylene protons of C-4 (δ_H 2.81 and 2.38) and the quaternary carbon C-3a (δ_C 158.47) indicated the bond between C-4 and C-3a. The quaternary carbons C-3a (δ_C 158.47) and C-9a (δ_C 103.48) were determined to be part of an α,β unsaturated five membered ring lactone which HMBC correlation proved to be methylated in the α position given that the lactone carbonyl C-2 (δ_C 172.07) correlated with the protons of 3-Me (δ_H 1.79).

The hydroxyl group (δ_H 4.08) was located at C-9a based on the fact that C-9a was shifted upfield compared to its chemical shift in the closely related structure furanoterpenoid (**4**). NOE indicated that the hydroxyl group was spatially close and of the same orientation as 8a-Me.

2.9.3. Autoxidation of the furanoterpenoid (4)

After isolation and purification of the furanoterpenoid (**4**) it was observed to be a highly unstable compound as the pure colorless crystals turned brownish on standing and $CDCl_3$ solutions of the compound instantaneously turned pink to brown.

UPLC MS analysis on the brownish crystals and comparison with the chromatogram obtained from fresh colorless crystals confirmed decomposition of the furanoterpenoid (**4**).

The chromatogram of the pure colorless crystals showed the presence of one compound while that of the brownish crystals revealed the presence of two new major peaks as shown in **Figure 2.5** and **Table 2.5**.

Table 2.5: MS and MS/MS data of the peaks observed after autoxidation of the furanoterpenoid (**4**).

Peak	RT (min)	$[M+H]^+$ (TOF MS ES+)	Relevant MS/MS ions	MassLynx calculated Molecular formula [a]	MassLynx accurate mass calculated [b]	Compound identified
		m/z	m/z			
a	10.03	263.1282	245.1178 203.1072 173.0970	$C_{15}H_{18}O_4$	263.1283	**6**
b	11.39	247.1338	229.1193 201.1265 159.1180	$C_{15}H_{18}O_3$	247.1334	**5**
c	17.78	231.1387	216.1144 165.0706 135.0812 123.0811	$C_{15}H_{18}O_2$	231.1385	**4**

[a] value based on subtraction of one proton from that calculated for $[M+H]^+$

[b] mass calculated from $[M+H]^+$

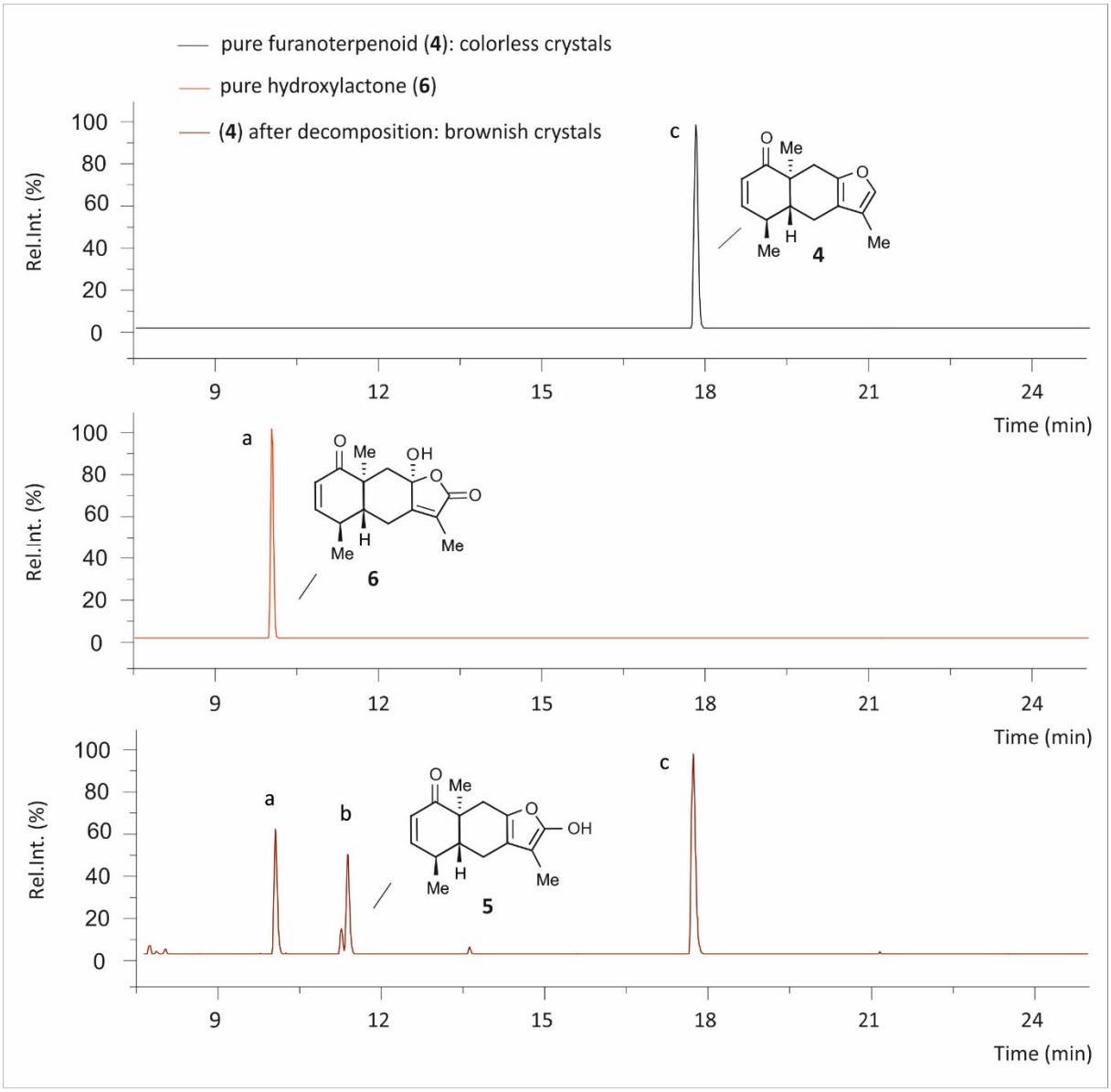

Figure 2.5: UPLC MS analysis of the furanoterpenoid (**4**) after autoxidation.

Analysis of the chromatogram from the brownish crystals through comparison of the retention times and MS/MS fragmentation patterns with that of the pure isolated compounds established the assignment of hydroxylactone (**6**) and the furanoterpenoid (**4**) to peaks labelled as a and c, respectively (**Figure 2.5** and **Table 2.5**).

Investigation of the MS and MS/MS fragmentation patterns also allowed the identification of the compound assigned as peak b. The molecular ion $[M+H]^+$ observed for peak b displayed a m/z of 247.1362 which gave the MassLynx calculated molecular formula of $C_{15}H_{18}O_3$ (mass calculated 247.1334).

A literature search for the molecular formula of $C_{15}H_{18}O_3$ corresponded to that of two sesquiterpenoids previously reported from African ginger (*viz*. compounds **5** and **7** in **Figure 2.2**).

Manual analysis of the fragmentation patterns of the two possible compounds, using ChemBioDraw Ultra 13.0, confirmed peak b to result from the hydroxyfuranoterpenoid (**5**) rather than the lactone (**7**).

The first evidence of the hydroxylated furanoterpenoid (**5**) assigned to peak b was based on the analysis of the abundant base peak with m/z 229.1193 (rel. int. 100%), as reported in **Table 2.5**. This base peak was due to a loss of 18 Da for the molecular ion $[M+H]^+$ (m/z 247.1338) and was characteristic of an hydroxyl group as a neutral loss of H_2O as described in step 1 of **Figure 2.6**.

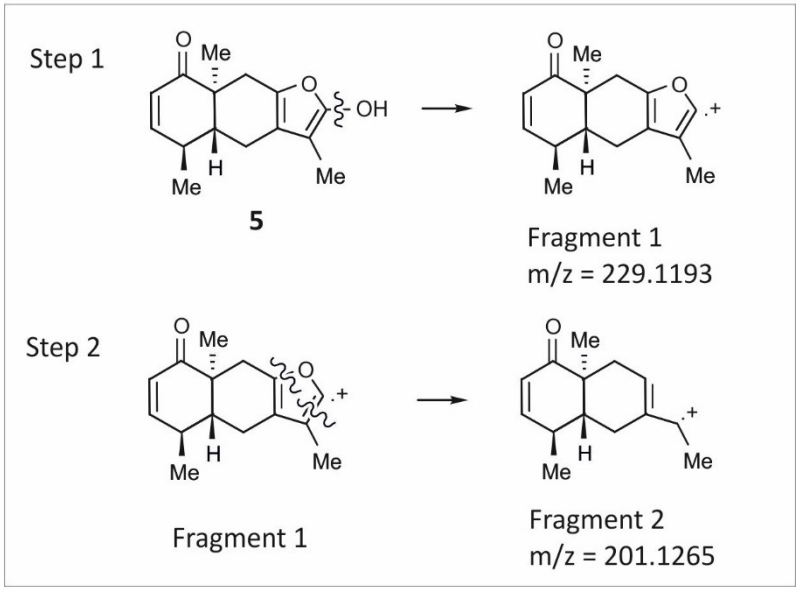

Figure 2.6: Possible MS/MS fragmentation pathway of the hydroxylated furanoterpenoid (**5**).

The second evidence was from the analysis of the MS/MS fragment with m/z 201.1265. This was found to result from a loss of a CO fragment (28 Da) from the ion formed in step 1 (**Figure 2.6,** step 2).

Fragmentation of the furan ring is in fact reported to release a CH=O fragment,[25] however based on the fact that the furan ring in fragment 1 does not carry any proton, only a loss of CO was possible to form fragment 2.

As formation of the hydroxylactone (**6**) and the hydroxyfuranoterpenoid (**5**) was unexpectedly observed after decomposition of the furanoterpenoid (**4**) it was postulated that these sesquiterpenoids, i.e. compounds (**5**) and (**6**) are possibly wrongly reported as naturally occurring in the plants and may be artefacts formed in the plants during storage of dried material as a result of decomposition of the furanoterpenoid (**4**).

To rationalize this, the decomposition of the furanoterpenoid (**4**) was regarded as a result of an autoxidation process through which (**5**) and (**6**) are formed.

Literature reports an autoxidation process of pseudoneolinderane (**9**), a sesquiterpenoid of the furanogermacrane type isolated from the stems of *Neolitsea parvigemma*.[26]

Autoxidation of pseudoneolinderane (**9**) led formation of artefact lactone compounds, i.e., pseudoneolinderane A (**10**) and pseudoneolinderane B (not shown) and was described as resulting from the oxidation of the furan moiety with O_2.[26]

The authors thus proposed a mechanism involving formation of a peroxide bridge, as illustrated in **Scheme 2.2.**

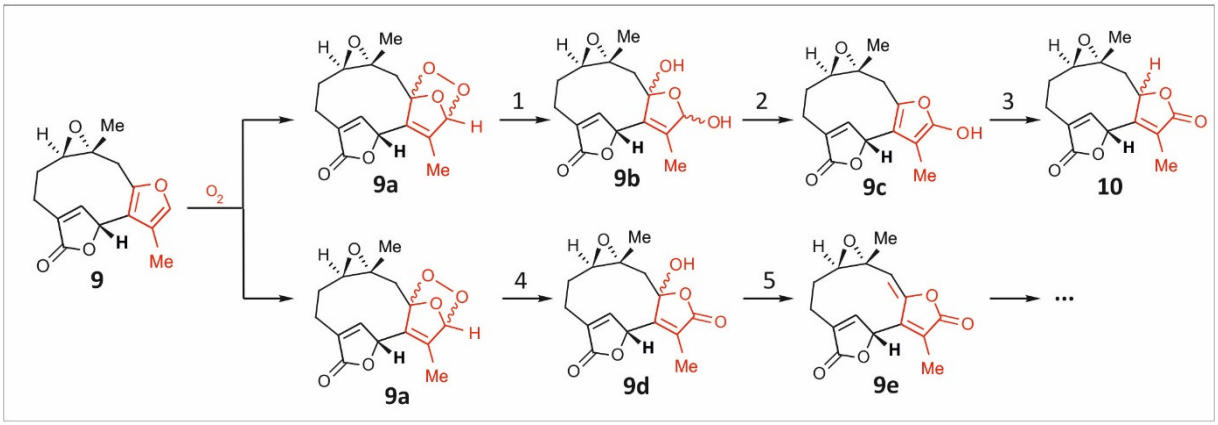

Scheme 2.2: Autoxidation mechanism of pseudoneolinderane (**9**).[26]

As part of the proposed mechanism, oxidation of pseudoneolinderane (**9**) with O_2 forms the peroxide (**9a**) which can then follow two possible routes. In the first route the peroxide (**9a**) is hydrolyzed to form compound (**9b**) which is then dehydrated and stabilized into (**9c**) before the final tautomerization that leads the artefact lactone pseudoneolinderane A (**10**).

In the second route the peroxide (**9a**) is lactonized to form compound (**9d**) which after dehydration affords compound (**9e**).[26]

Comparison between the products and the mechanism described for pseudoneolinderane (**9**) with the products observed after decomposition of the furanoterpenoid (**4**) provided conclusive evidence that the furanoterpenoid (**4**) undergoes an autoxidation which most likely occurs through a similar mechanism to that reported for pseudoneolinderane (**9**) in that the hydroxylactone (**6**) structurally resembles the product (**9d**) and the hydroxyfuranoterpenoid (**5**) can be related to the product (**9c**) (**Scheme 2.2**).

Through this investigation it was shown that the hydroxyfuranoterpenoid (**5**)[4] and the hydroxylactone (**6**)[14] are autoxidation products of the furanoterpenoid (**4**) and most likely formed through a mechanism similar to that shown for pseudoneolinderane (**9**) in **Scheme 2.2**.

2.9.4. Chemical profiling of wild and cultivated plants

2.9.4.1. UPLC MS chemical profiling

The UPLC MS chemical profiling was attempted on n-hexane/DCM (1:1) extracts obtained from air-dried rhizomes of African ginger. The gradient system provided in **Table 2.1** (see **section 2.8.2.3**) was used and the resulting chromatograms for the different extracts are presented in **Figure 2.7**.

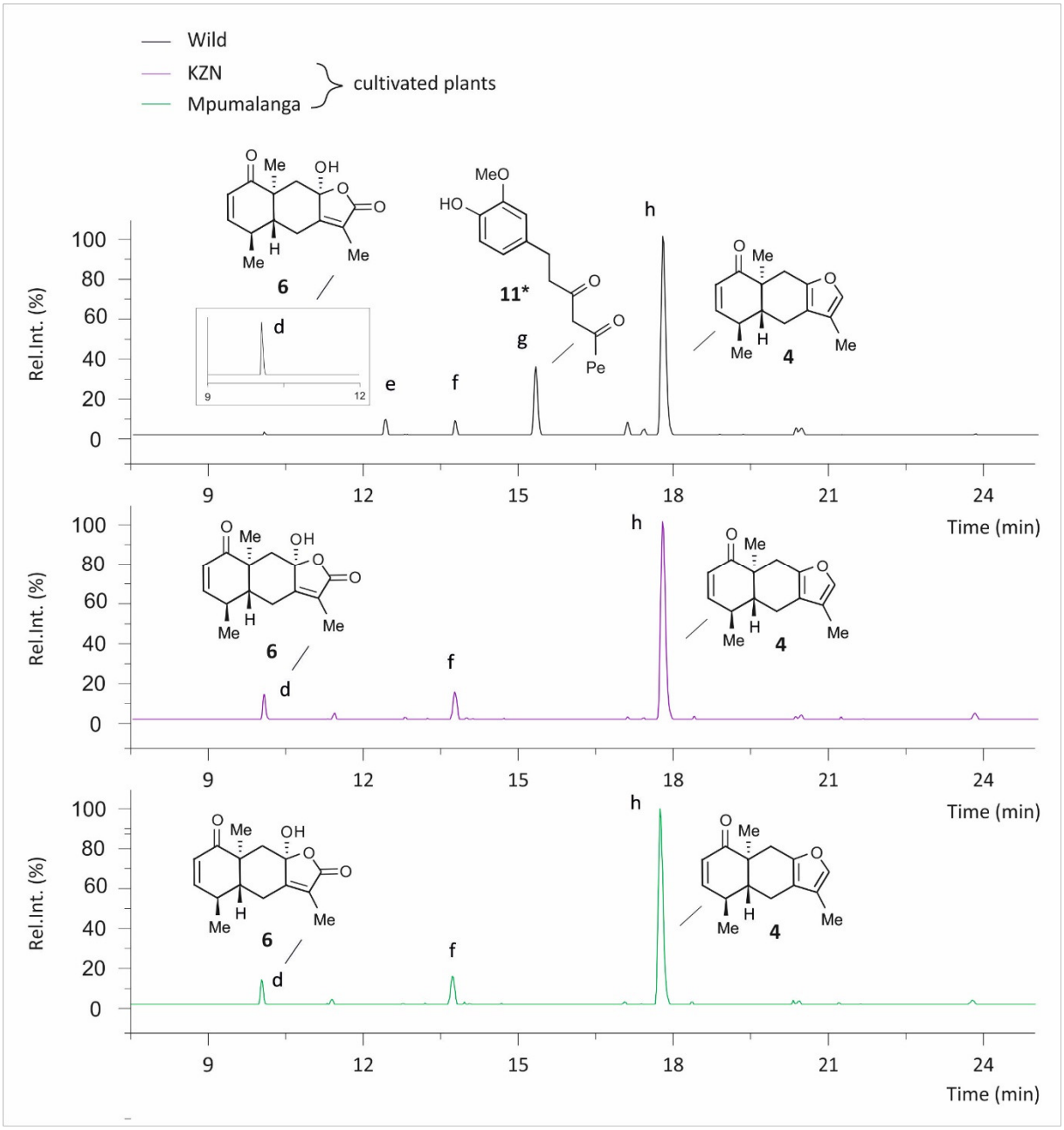

Figure 2.7: UPLC-MS chemical profiles of n-hexane/DCM (1:1) extracts of African ginger (the range between 7.00 to 21.00 min shown for clarity, * provisional structure).

At least five relevant peaks were identified in wild plants and labelled accordingly, as shown in **Figure 2.7** and reported in **Table 2.6**.

Table 2.6: Characterization of the peaks observed in the UPLC-MS chemical profiles of African ginger.

Peak	RT (min)	$[M+H]^+$ (TOF MS ES+)	Relevant MS/MS fragments	MassLynx calculated molecular formula	MassLynx accurate mass calculated	Compound identified	Wild	KZN and Mp.
		m/z	m/z					
d	10.03	263.1282	245.1178 203.1072 173.0970	$C_{15}H_{18}O_4$	263.1283	**6**	✓	✓
e	12.38	249.1496	231.1383 213.1278 173.0967	$C_{15}H_{20}O_3$	249.1491	-	✓	**x**
f	13.73	245.1199	227.1087 183.0604 162.5479	$C_{15}H_{16}O_3$	245.1178	**8***	✓	✓
g	15.28	293.1756	275.1645 233.1538 215.1432	$C_{17}H_{24}O_4$	293.1753	**11***	✓	**x**
h	17.74	231.1387	216.1144 165.0706 135.0812 123.0811	$C_{15}H_{18}O_2$	231.1385	**4**	✓	✓

** provisional structure*
✓: present
X: absent
Mp: Mpumalanga

The peaks d and h were unambiguously identified as the furanoterpenoid (**4**) and the artefact hydroxylactone (**6**) based on the comparison with data from purified standards, *i.e.*, the chromatograms of pure compounds (**4**) and (**6**) in **Figure 2.5**.

Peak f was provisionally identified as the di-unsaturated sesquiterpenoid lactone (**8**) with the calculated molecular formula $C_{15}H_{16}O_3$ and the m/z observed for the $[M+H]^+$ parent ion the same as that reported by Lategan et al.[14]

For the peaks e and g only the molecular formulas were reliably established from the observed $[M+H]^+$ parent ions as MS and MS/MS data were not sufficient enough to unequivocally identify their correct molecular structures especially since no compound with the related m/z have been previously reported from African ginger. Peak e revealed a $[M+H]^+$ with m/z 249.1496 which gave the molecular formula of $C_{15}H_{20}O_3$ (mass calculated 249.1491). The $[M+H]^+$ of peak g was observed with m/z 293.1756 and matched the molecular formula $C_{17}H_{24}O_4$ (mass calculated 293.1753).

Nevertheless peak g was tentatively identified through the useful online tool MetFusion.[27] The $[M+H]^+$ with m/z 293.1756 was uploaded online and the query resulted in two candidate compounds of which the first hit was 6-gingerdione (**11**), an aromatic compound reported to be present in *Zingiber officinale*,[28] another species of the Zingiberaceae family to which African ginger belongs. Investigation of the MS/MS fragmentation pattern of peak g suggested the fragment with m/z 275.1645 as a result of loss of neutral water $[M+H-H_2O]^+$ from the hydroxyl group in the α position of the carbon carrying the methoxy group in 6-gingerdione (**11**) as shown in **Figure 2.8**.

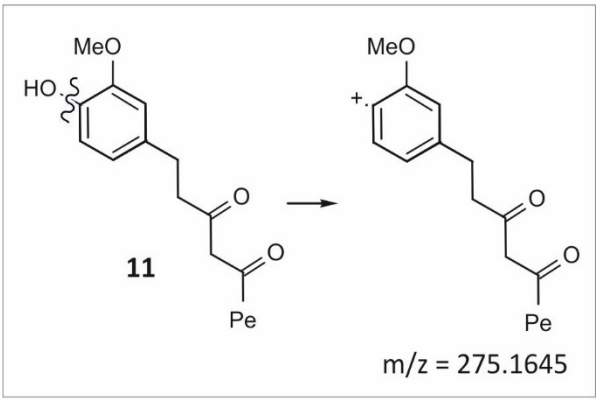

Figure 2.8: Loss of water in 6-gingerdione (**11**) through MS/MS fragmentation.

However, the reported structure should be regarded as provisional as only extensive NMR analysis on the isolated pure compound can unambiguously confirm the structure of the compound.

The furanoterpenoid (**4**) was identified as the major peak labelled h in the extracts from both wild and cultivated plants as it produced an intense speak at 17.74 minutes (m/z 231.1385) (**Figure 2.7**).

The compounds assigned to peaks e and g in the chromatogram were found to only occur in wild plants as no peaks with the same retention time and MS data were observed in the profiles of the cultivated plants.

As the hydroxylactone (**6**) may not occur naturally in the plant due to autoxidation of the furanoterpenoid (**4**), this adds complexity to standardizing the natural chemical compounds produced in the plant. The natural chemical compounds are integral to the chemical profiling.

2.9.4.2. Autoxidation in dried and powdered African ginger rhizomes

To investigate the presence or the absence of the hydroxyfuranoterpenoid (**5**) and hydroxylactone (**6**) in fresh wet plants and in extracts from dried ground rhizomes and powders held under storage at room temperature, extracts were analyzed by UPLC MS and the chemical profiles of these extracts are shown in **Figure 2.9**. Only compounds identified as relevant to the autoxidation are discussed while extracts from fresh cultivated were not analyzed due to insufficient material for recollection.

The extracts from the fresh wet plants showed the furanoterpenoid (**4**) as the major compound labelled as peak h. Both the hydroxyfuranoterpenoid **(5)** and hydroxylactone (**6**) were not detected in the extracts of the fresh plants (**Figure 2.9**).

The furanoterpenoid (**4**) was still the major peak in the extract prepared from powders obtained immediately after completion of the drying and grinding process (chromatogram shown only for wild plants). This extract however, also revealed a small peak of the hydroxylactone (**6**) (labelled d).

The major furanoterpenoid (**4**) compound was not detected in the extracts from powders stored at room temperature for nine months. The two autoxidation products, *viz*. the hydroxyfuranoterpenoid (**5**) and hydroxylactone (**6**) (peaks labelled as d' and d) which were absent in the fresh wet plants, appeared as more intense peaks in the extracts from the samples held under storage.

The results unambiguously proved that the furanoterpenoid (**4**) converts into its autoxidation products, i.e., the hydroxylactone (**6**) and the hydroxyfuranoterpenoid (**5**) in fresh plants that have been dried, ground and held under storage (see the highlighted regions in **Figure 2.9**). Furthermore, peak f, which is assumed to be the di-unsaturated sesquiterpenoid lactone (**8**) reported by Lategan et al.,[14] is also suspected to result from autoxidation, provided that the same peak also appears in the chromatogram from the decomposed furanoterpenid (**4**), and that compound (**8**) could be structurally related to the intermediate (**9e**) of the autoxidation mechanism of pseudoneoliderane (**9**) (see **Scheme 2.2** and **Figure 2.2**). It should be noted that peak f is in trace quantities in the fresh plants which implies it could be the first autoxidation product.

This investigation has proven that the hydroxylactone (**6**) and the hydroxyfuranoterpenoid (**5**) have been incorrectly reported as naturally occurring in African ginger. It has also established that for a conclusive comparison between the chemical profiles of wild and cultivated plants, extracts must be prepared from fresh rhizomes and processed as autoxidation will lead to formation of artefact compounds that can complicate the study and afford incorrect conclusions.

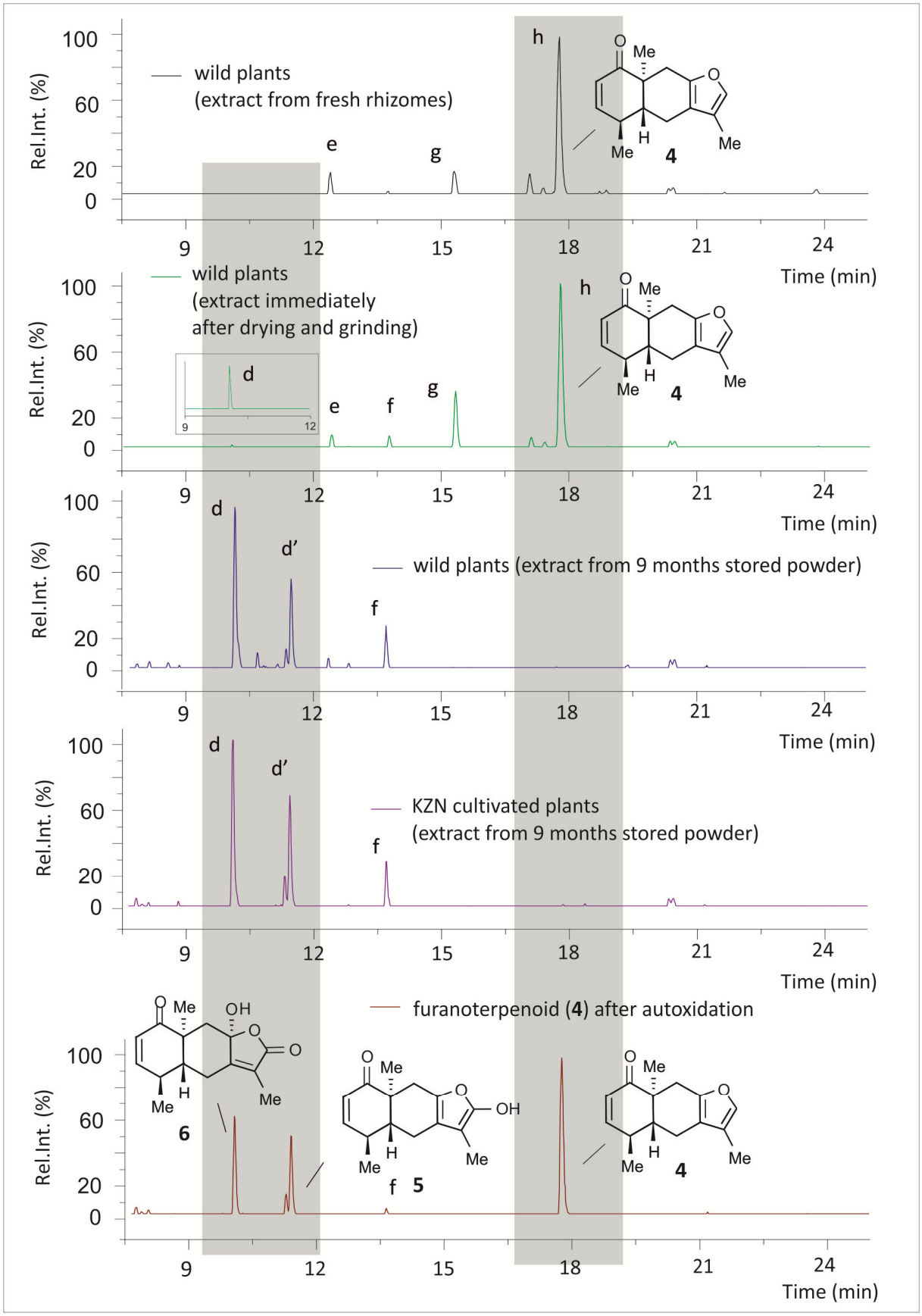

Figure 2.9: Investigation of the hydroxylactone (**6**) and the hydroxyfuranoterpenoid (**5**) in fresh rhizomes which was then dried, ground and held under storage.

2.9.4.3. GC MS chemical profiling

The GC MS chemical profiling was separately investigated on n-hexane extracts from air-dried wild and cultivated African ginger rhizomes. Extracts were prepared according to the protocol described in the **section 2.8.2.1**, and the resulting chromatograms are shown in **Figure 2.10**.

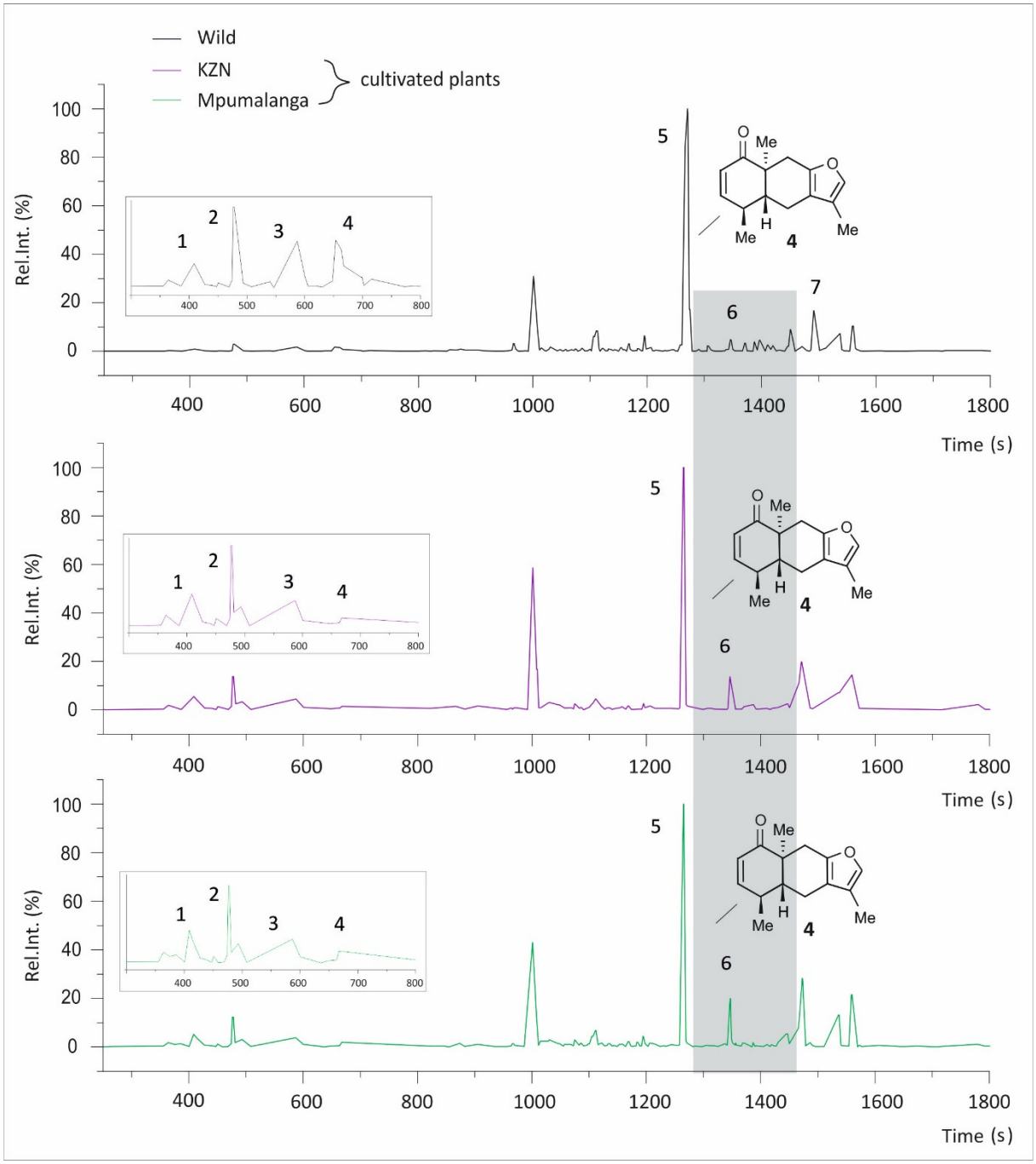

Figure 2.10: GC MS chemical profiles of wild and cultivated African ginger.

The relevant compounds were identified based on the matching with the NIST08 library and only compounds above 90.0 % similarity are reported in **Table 2.7** and numbered as shown in **Figure 2.10**.

Table 2.7: Compounds in the GC MS chemical profiles (* confirmed with authentic standards).

Peak number	RT (s)	Hit compound	Formula	MW	Similarity (%)	RI_{exp}
1	408.7	α-phellandrene	$C_{10}H_{16}$	136	91.8	988
2	477.9	Eucalyptol*	$C_{10}H_{18}O$	154	92.3	1018
3	586.9	Neo-allo-ocimene	$C_{10}H_{16}$	136	91.8	1066
4	653.4	p-cymen-8-ol	$C_{10}H_{14}O$	150	93.9	1096
5	1270.6	Furanoterpenoid (**4**)*	$C_{15}H_{18}O_2$	230	-	1867
6	1347.6	n-hexadecanoic acid	$C_{16}H_{32}O_2$	256	92.4	1969
7	1472.7	Cis-13-octadecenoic acid	$C_{18}H_{34}O_2$	282	92.2	2147

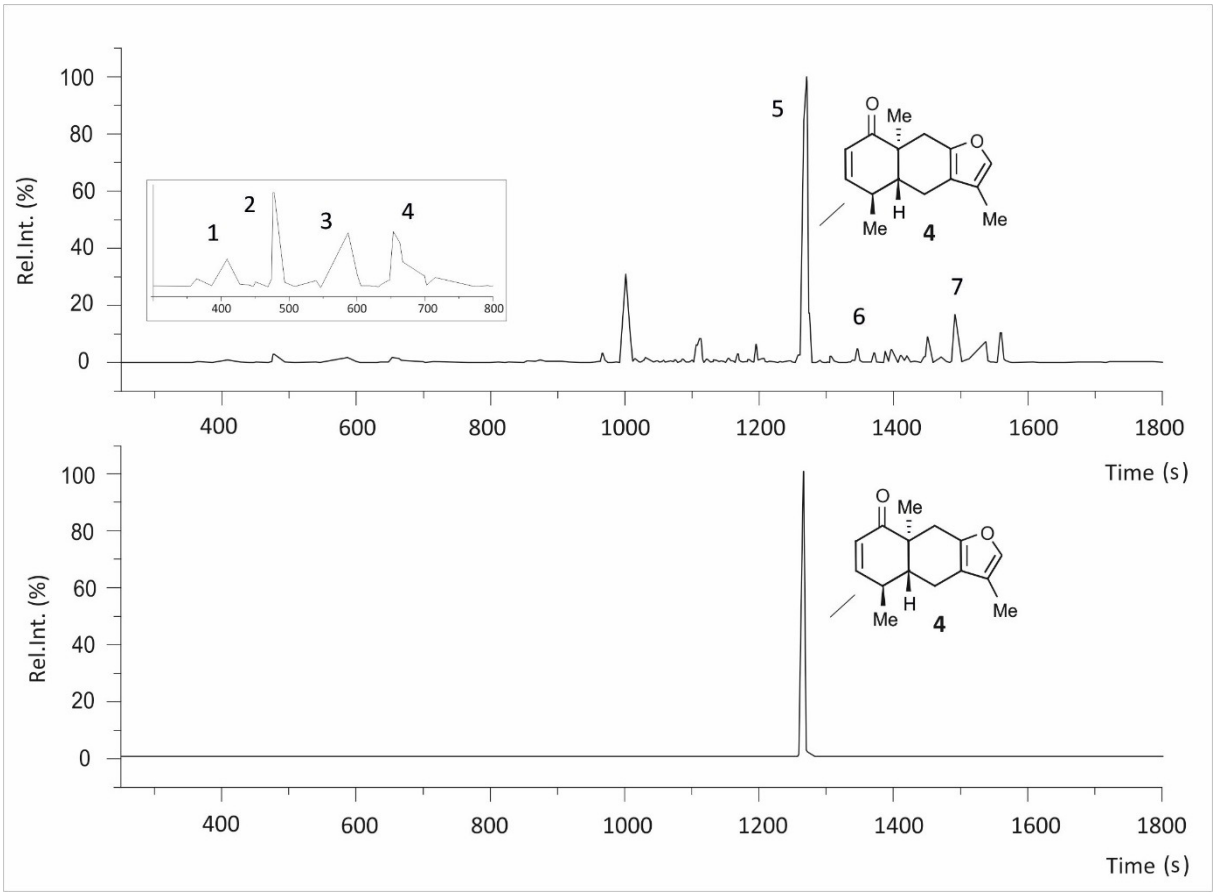

Figure 2.11: Identification of the furanoterpenoid (**4**) in the GC MS chromatograms (chemical profile of wild plants shown).

In addition to the identification of the furanoterpenoid (**4**) (peak labelled 5, see also **Figure 2.11**), eucalyptol (peak labelled as 2) was identified through the NIST08 library match. They were confirmed with authentic standards based on their retention times and the calculated retention indices. The presence of eucalyptol in the essential oil of the plant has previously been reported by Viljoen et al.[16]

The artefact hydroxylactone **(6)** was not detected even after the injection of the pure standard presumably due to poor volatility and/ or the ionization method employed (chromatogram not shown).

In the comparison of both the wild and cultivated plants, the furanoterpenoid (**4**) was identified as the major peak in the chemical profiles (**Figure 2.10**).

The GC MS proved that the cultivated plants sourced from KZN and Mpumalanga were similar based on their overall chemical profiles as these were substantially similar to each other (**Figure 2.10**). Although much similarity was observed for the chemical profiles between the wild and cultivated plants, numerous unidentified signals between the peaks labelled 6 and 7 were found to only occur in the wild plants (**Figure 2.10**, see the highlighted section).

2.9.4.4. Impact of drying processes on eucalyptol and the furanoterpenoid (4)

Since African ginger is traditionally used to treat asthma[6] and that eucalyptol with known anti-asthmatic activity[29, 30] occurs in the extracts of dried plants (**section 2.9.3.2**), the investigation of the impact of the drying process on eucalyptol and the furanoterpenoid (**4**) was further investigated. Eucalyptol is also a volatile compound and it is possible that it may be lost due to evaporation during the drying process. Furthermore, most reported scientific studies on anti-asthmatic properties of African ginger had been conducted on extracts from dried rhizomes while the traditional preparations also use the fresh rhizomes.[6, 31, 32] Impact of the drying process is exclusively reported for wild plants as they were the only ones for which fresh rhizomes were still available at the time of the analysis.

The n-hexane extracts from fresh, air-dried (A-D) and oven-dried (O-D) rhizomes were subjected to GC MS analyses and the results as the related absolute peak areas of the eucalyptol and the furanoterpenoid (**4**) are shown in **Figure 2.12**.

The quantities of the plants extracted, solvents, extraction time, and GC MS method were all the same for the three samples (see **section 2.8.2.1**) substantiating a semi quantitative analysis of the compounds.

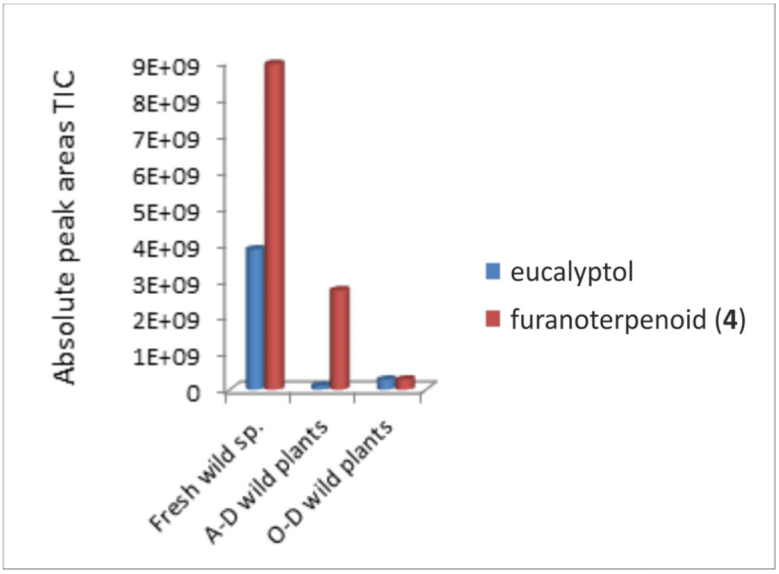

Figure 2.12: Depletion of eucalyptol and the furanoterpenoi (**4**) after drying the plant.

Results proved that any form of drying of the plants leads to loss of eucalyptol and the furanoterpenoid (**4**) as shown in **Figure 2.12**. The oven-drying process was observed to be the most drastic resulting in a substantial decrease in the furanoterpenoid (**4**) compared to the fresh and air dried samples.

The foregoing results suggest that studies on extracts prepared from plants that have been through the drying process should take into consideration the levels of eucalyptol in the extracts as this may influence the outcome of the anti-asthmatic biological efficacy.

2.9.5. Antimalarial screening

In vitro antiplasmodial activity against *P. falciparum* (CQS) NF54 strain for Hexane/DCM (1:1) extracts from air-dried wild and cultivated rhizomes is reported in **Table 2.8**.

Table 2.8: *In vitro* antiplasmodial activity of African ginger extracts.

African ginger plants	IC_{50} (µg/ml)
Wild	2.28 ± 0.11
KZN	2.28 ± 0.30
Mpumalanga	3.05 ± 0.17

CQ: 0.004 ± 0.001; Artesunate: <0.002 ± not determined

Antimalarial IC_{50} values did not reveal significant differences between the activity of the wild and the cultivated plants.

2.10. Conclusion

Extraction of dried powdered wild and cultivated plants of African ginger using n-hexane/DCM (1:1) has demonstrated wild plants to produce greater extraction yields (ca. three times that of the cultivated samples).

Chemical profiling using UPLC MS chromatography confirmed the major peak in the chromatograms of both the wild and cultivated plants to be the furanoterpenoid (**4**) reported by Holzapfel et al.[4] The compound was further characterized using NMR and X-ray crystallography after isolation through column chromatography.

UPLC MS analysis revealed a noticeable difference between the chemical profiles of the extracts from wild and cultivated plants. Extracts of the wild plants displayed two additional peaks, of which one was provisionally identified as the aromatic 6-gingerdione also reported to occur in *Zingiber officinale*.

The furanoterpenoid (**4**), present in both wild and cultivated plants, was observed to be highly unstable and was unambiguously proven to autoxidize to produce two major structurally close sesquiterpenoids. The two autoxidation products were identified as the hydroxylactone (**6**) and the hydroxyfuranoterpenoid (**5**) reported by Lategan et al.[14] and Holzapfel et al.,[4] respectivey to occur in the plant.

The monitoring of the furanoterpenoid autoxidation through UPLC MS analysis in dried and room temperature stored plants clearly demonstrated that the hydroxylactone (**6**) and the hydroxyfuranoterpenoid (**5**) are only formed as the dried powdered plants are held under storage due to the degradation of the parent furanoterpenoid (**4**). The extent of autoxidation of the furanoterpenoid (**4**) proceeds to a point whereby it is completely absent in nine months old stored dried powders. This result was in contradiction with Holzapfel et al.[4] and Lategan et al.[14] who reported the two compounds which we identified as autoxidation artefacts, as naturally occurring in African ginger. The results further suggested that studies on African ginger plants should be conducted with extracts from fresh plants rather than dried and stored powders, as autoxidation generates artefact compounds which are not originally present in the plant.

GC MS chemical profiling was performed on n-hexane extracts from fresh plants as well as powders from air-dried and oven-dried rhizomes. Results showed the furanoterpenoid (**4**) to be the major compound in the profiles of both wild and cultivated plants. The GC MS profile of the extracts from

wild plants revealed a series of several unidentified minor peaks which were not observed in the cultivated plants.

GC MS results also confirmed the presence of eucalyptol in extracts from wild and cultivated plants.

Study of the impact of drying the plant on the composition of selected volatiles revealed air-drying and oven-drying processes to significantly reduce the levels of eucalyptol and the furanoterpenoid (**4**) in the resulting plant extracts.

As eucalyptol has known anti-asthmatic properties, this result suggest that studies on extracts prepared from dried plants should consider the levels of eucalyptol in the extracts as this may affect the outcome of the anti-asthmatic activity.

Antiplasmodial screening of the n-hexane/DCM (1:1) extracts did not show any significant differences between the bioactivities of wild and cultivated plants. This suggests that the additional compounds observed for the wild plants may not contribute to the antimalarial activity of the plant.

References

[1] M. Lock, *Flora of tropical East Africa: Zingiberaceae*, Balkema, Rotterdam, **1985**, p. 14.

[2] R. Smith, *Bothalia* **1998**, *28*, 35-39.

[3] B. Van Wyk, B. V. Oudtshoorn, N. Gericke, *Medicinal Plants of South Africa*, Briza, Pretoria, **2009**, p. 274.

[4] C. W. Holzapfel, W. Marais, P. L. Wessels, B. Van Wyk, *Phytochemistry* **2002**, *59*, 405-407.

[5] M. Mander, *Marketing of indigenous medicinal plants in South Africa: a case study in KwaZulu-Natal*, Food and Agriculture Organization (FAO) of the United Nations, Rome, **1998**, p. 47.

[6] G. Fouche, S. van Rooyen, T. Faleschini, *Int. J. Genuine Trad. Med.* **2013**, *3*, 24-29.

[7] A. Cunningham, *An investigation of the herbal medicine trade in Natal/KwaZulu*, University of Natal Press, Pietermaritzburg, **1988**, p. 4.

[8] N. Crouch, M. Lotter, S. Krynauw, C. Pottas Bircher, *Herbertia* **2000**, *55*, 115-129.

[9] V. Williams, J. Victor, N. Crouch, *S. Afr. J. Bot.* **2013**, *86*, 23-35.

[10] A. Hutchings, *Zulu medicinal plants: an inventory*, University of Natal Press, Pietermaritzburg, **1996**, p. 64.

[11] B. Van Wyk, *S. Afr. J. Bot.* **2011**, *77*, 812-829.

[12] A. Hankey, Y. Reynolds, "*Siphonochilus aethiopicus* (Schweif.) B.L. Burt", can be found under http://www.plantzafrica.com/plantqrs/siphonaeth.htm, **2002**. (accessed 05/05/2015)

[13] N. Crouch, R. Symmonds, *Plantlife* **2002**, *26*, 19-20.

[14] C. A. Lategan, W. E. Campbell, T. Seaman, P. J. Smith, *J. Ethnopharmacol.* **2009**, *121*, 92-97.

[15] M. Light, L. McGaw, T. Rabe, S. Sparg, M. Taylor, D. Erasmus, A. Jäger, J. Van Staden, *S. Afr. J. Bot.* **2002**, *68*, 55-61.

[16] A. Viljoen, B. Demirci, K. Baser, B. Van Wyk, *S. Afr. J. Bot.* **2002**, *68*, 115-116.

[17] N. Makhuvha, B. Van Wyk, H. Van der Bank, M. Van der Bank, *Biochem. Syst. Ecol.* **1997**, *25*, 343-351.

[18] T. Z. Manzini, MSc dissertation, University of Pretoria (South Africa), **2005**.

[19] E. Pichersky, D. R. Gang, *Trends Plant Sci.* **2000**, *5*, 439-445.

[20] R. Akula, G. A. Ravishankar, *Plant Signal Behav.* **2011**, *6*, 1720-1731.

[21] M. Mander, L. Ntuli, N. Diederichs, K. Mavundla, *S. Afr. health rev.* **2007**, 189-196.

[22] H. Van den Dool, P. D. Kratz, *J. Chromatogr. A* **1963**, *11*, 463-471.

[23] W. Trager, J. B. Jensen, *Science* **1976**, *193*, 673-675.

[24] M. T. Makler, J. M. Ries, J. A. Williams, J. E. Bancroft, R. C. Piper, B. L. Gibbins, D. J. Hinrichs, *Am. J. Trop. Med. Hyg.* **1993**, *48*, 739-741.

[25] M. Al-Kahali, T. Ridley, K. Lawley, R. Donovan, *Arab. J. Sci. Eng.* **2008**, *33*, 51-54.

[26] K. Chen, Y. Wu, *Tetrahedron* **1999**, *55*, 1353-1366.

[27] M. Gerlich, S. Neumann, *J. Mass Spectrom.* **2013**, *48*, 291-298.

[28] H. Jiang, A. M. Sólyom, B. N. Timmermann, D. R. Gang, *Rapid Commun. Mass Spectrom.* **2005**, *19*, 2957-2964.

[29] U. R. Juergens, M. Stober, H. Vetter, *Eur. J. Med. Res.* **1998**, *3*, 508-510.

[30] U. R. Juergens, U. Dethlefsen, G. Steinkamp, A. Gillissen, R. Repges, H. Vetter, *Respir. Med.* **2003**, *97*, 250-256.

[31] R. Coopoosamy, K. Naidoo, *Afr. J. Pharm. Pharmacol.* **2012**, *6*, 818-823.

[32] G. Fouche, N. Nieuwenhuizen, V. Maharaj, S. van Rooyen, N. Harding, R. Nthambeleni, J. Jayakumar, F. Kirstein, B. Emedi, P. Meoni, *J. Ethnopharmacol.* **2011**, *133*, 843-849.

Chapter 3

Absolute configurations of compounds from mangroves and *Ancistrocladus* species

3.1. Introduction

In Chemistry, the term "absolute configuration" refers to the spatial distribution of atoms in chiral molecules.[1] It is an important concept in the study of molecular structures.

The investigation of the absolute configurations, especially for chiral compounds with biological benefits, remains a relevant task.[2-7] In fact, when molecular structures of chiral compounds are studied, especially for those that originate from biological sources, the final tridimensional disposal of the constitutive atoms needs to be resolved. This task is particularly important since chiral compounds may exist in two different tridimensional structures that are mirror-image but not superimposable, and referred to as enantiomers.

For the characterization of enantiomers, only few techniques are available and documented in dedicated literature. The techniques used range from the sophisticated NMR[8-10] and X-ray diffraction,[11, 12] the time-demanding partial and total synthesis,[13-15] to the affordable and very sensitive chiroptical methods.[16-20]

Nowadays, chiroptical methods such as circular dichroism (CD), optical rotatory dispersion (ORD), and Raman optical activity (ROA) are accepted and have been widely applied as a tool for solving enantiomers and thus, for the elucidation of the absolute configurations.[17, 21-23]

It is further reported that chiroptical methods have the advantage of not requiring as much preconditions as it is the case for the other techniques previously mentioned, e.g., the use of X-ray diffraction is restricted only to suitable single crystals,[24] the NMR involves chiral derivatizing agents such as Mosher acids,[25] the partial and total synthesis require a starting precursor of known absolute configuration.[13-15] Another reported advantage of chiroptical techniques, and CD in particular, is that they do not require huge amounts of sample and the equipment related is cost affordable.[21]

However, fact is that the investigation of the absolute configurations by means of chiroptical methods strongly relies on the interpretation of the data. In the last decades, advances made in computational

chemistry have made feasible the prediction of chiroptical properties from theoretical formalisms.[26-30] This has given rise to a method of interpretation based on the matching of experimental chiroptical signals with data issued from quantum-chemical computations.

This approach, based on the comparison of experimental and theoretical data, has proved to be successful for a variety of both natural and synthetic products.[3, 4, 31-34]

In the present chapter, the absolute configurations of natural products isolated from mangroves and *Ancistrocladus* species are investigated. The investigation has been conducted using CD and ORD chiroptical methods in combination with quantum-chemical calculations.

3.2. Chiroptical methods

From the interactions between enantiomers and beams of polarized lights, numerous chiroptical phenomena, such as ORD and CD, have been rationalized.[35, 36]

3.2.1. Optical rotation and optical rotatory dispersion

Optical rotatory dispersion emerges from optical rotation,[23, 37] i.e., the ability of enantiomers to deviate a linearly polarized light (*Lpl*) from its plane of polarization.[1] This phenomenon has been described since the early nineteenth century and evidenced in a number of both inorganic and organic substances;[38] *viz.* quartz (by F.J.D. Arago in 1811), turpentine (by J.B. Biot in 1815) and tartaric acid (by L. Pasteur in 1848).

3.2.1.1. Optical rotation

The optical rotation phenomenon is described as being the consequence of the difference between the refractive indexes of the components of a linearly polarized light (Lpl) toward a sample of a chiral molecule.[36, 37] A. Fresnel depicted (**Figure 3.1**) these components as the left and right circularly polarized lights (*lCpl* and *rCpl*, respectively).[37]

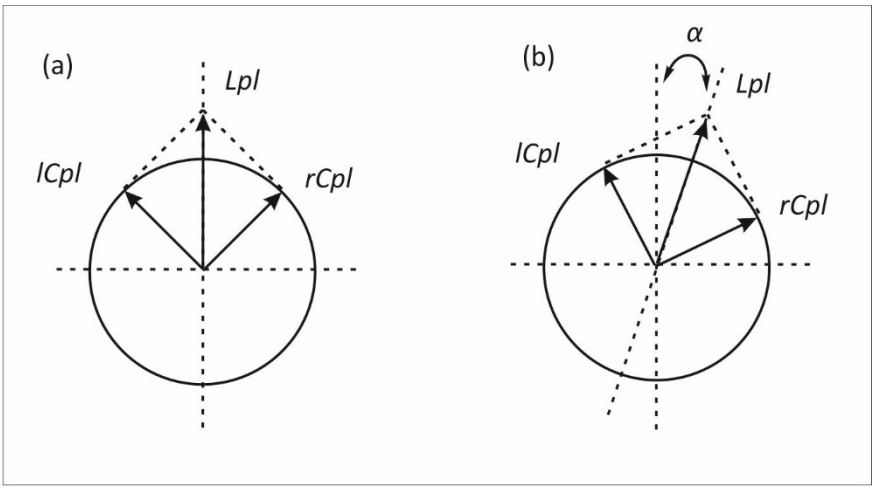

Figure 3.1: (a) An *Lpl* depicted as the resultant of coherent *lCpl* and *rCpl* components; (b) definition of optical rotation.[36]

When an *Lpl* beam travels through an optically active sample of a chiral molecule, the velocities of the *lCpl* and *rCpl* components are differently modified (**Figure 3.1**). This result in that the exiting *lCpl* and *rCpl* are no longer coherent and the resultant that comes out is deviated from the initial plane of polarization by an angle α, referred to as optical rotation (**Figure 3.1b**).

From the experimental view, the optical rotation angle (α) is linearly proportional to the thickness l of the sample cell and the density ρ of the considered substance (**Equation 3.1**).

$$\alpha = k\rho l \tag{3.1}$$

In equation (3.1) the proportional factor k stands for the so-called specific rotation and is usually noted $[\alpha]$. It is commonly expressed in the form of equations (3.2) and (3.3) where, in the latter case, the concentration *c* is given in g/100 ml of solution.[23]

$$[\alpha] = \frac{\alpha}{l\rho} \tag{3.2}$$

$$[\alpha] = \frac{100\alpha}{lc} \tag{3.3}$$

From the specific rotation above, a molar quantity (molar rotation $[\phi]$) is defined[23] when the relative molar mass *M* of the chiral molecule is considered (**Equation 3.4**).

$$[\phi] = \frac{[\alpha]M}{100} \tag{3.4}$$

Enantiomers of a given chiral compound always give rise to optical rotations, and therefore specific rotations, that are equal in magnitude but of opposite signs. This means that they always rotate the light in opposite directions.

In the early days of stereochemistry, enantiomers were exclusively distinguished according to the direction in which they rotate the plane of polarization of an *Lpl*. The terms dextrorotatory (d-) and levorotatory (l-) were used in reference to clockwise-rotating and anticlockwise-rotating enantiomers respectively.

Nowadays, the nomenclature of enantiomers is essentially based on the Cahn-Ingold-Prelog (CIP) protocol, i.e., the *R*/*S* and P/M assignment of chiral elements. [23, 31, 33, 34]

It should be noted that optical and specific rotations depend upon experimental conditions. They may vary with the temperature on the one hand, and with the wavelength of the polarized light on the other hand.[23]

3.2.1.2. Optical rotatory dispersion and absolute configuration assignment from ORD data

Optical rotatory dispersion is the graph obtained when one considers the measurement of optical rotations in dependence with the wavelengths.[37, 39]

The elucidation of absolute configurations upon ORD data is usually done either by comparing the experimental ORD spectra of the investigated compound with that of structurally related molecules of previously established absolute configuration,[40, 41] or according to its fitting with the calculated ORD curves of the possible enantiomers.[39, 42, 43]

3.2.2. Circular dichroism

The mechanism behind the circular dichroism (CD) effect is similar to that of the optical rotation described in the previous sections. The substantial difference is that the *Lpl* lights used for CD have energies that are located in the region where the investigated compound absorbs.[35, 36, 44]

When an optically active sample of a chiral molecule is subjected to an *Lpl* that has a resonating energy, the molecules within the sample do not only alter the speeds of the *lCpl* and *rCpl* components (**Figure 3.2**), but also absorb them with different magnitudes,[36, 44] to the point that the exiting resultant light is elliptically polarized (*Epl*).

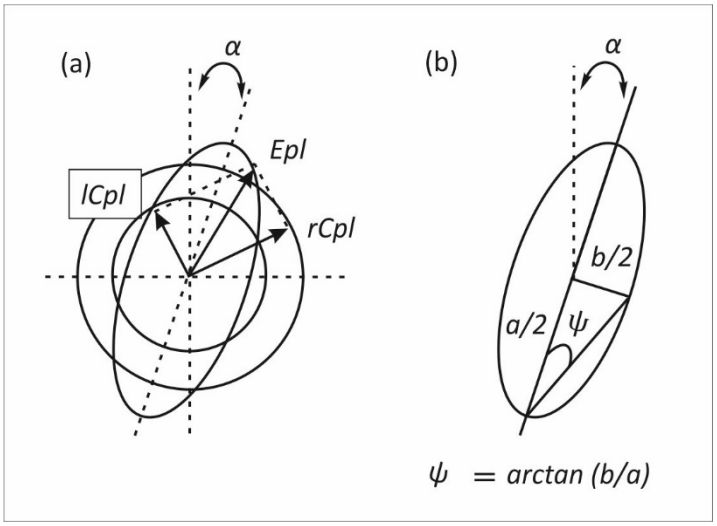

Figure 3.2: (a) Absorption of *lCpl* and *rCpl* components results toward an active sample; (b) Characterization of the ellipticity angle ψ.[36]

Consequently, CD is defined as the difference (**Equation 3.5**) between the absorption of the *lCpl* and *rCpl* components, A^{lCpl} and A^{rCpl} respectively.[36, 44]

$$CD = \Delta A = A^{lCpl} - A^{rCpl} \tag{3.5}$$

From the experimental measurements, CD is commonly reported in terms of a molar quantity (molar CD), which is independent of the concentration *c* of the investigated compound.[36]

This molar CD ($\Delta\varepsilon$) is defined, in agreement with the Lambert-Beer law,[44] as the difference (**Equation 3.6**) between the molar extinction coefficients of the *lCpl* and *rCpl* lights (ε^{lCpl} and ε^{rCpl}).

$$\Delta\varepsilon = (\varepsilon^{lCpl} - \varepsilon^{rCpl}) = \frac{CD}{lc} \tag{3.6}$$

The molar CD quantity is related to the ellipticity angle ψ, described by the elliptically polarized light (*Epl*) and characterized by its major and minor axes halves (**Figure 3.2b**)[36] and the expression that links them is given by the equation (3.7).

$$[\theta] = 3298.2\,\Delta\varepsilon \tag{3.7}$$

In the equation above, the quantity $[\theta]$ stands for the molar ellipticity, whose expression is provided by the Moscowitz equation (3.8).[45]

$$[\theta] = \frac{[\psi]M}{100} \tag{3.8}$$

$[\psi]$ stands for the specific ellipticity (**Equation 2.9**) and M for the relative molar mass of the compound.

$$[\psi] = \frac{\psi}{l\rho} = \frac{100\psi}{lc} \tag{3.9}$$

Similarly to the ORD, a CD curve is plotted from the molar CD values ($\Delta\varepsilon$) recorded within a certain range of the electromagnetic spectrum.

When the considered range involves electronic transitions (e.g., UV range), the CD spectroscopy that results is referred to as the electronic CD (ECD).[7, 21, 44, 46] In the case of vibrational transitions (IR range), a vibrational CD (VCD) is obtained.[47]

While ECD is adequate for compounds with UV-active functions, VCD is quoted additionally suitable for molecules that lack chromophores.[7, 21, 44, 47]

In the framework of the work reported in this chapter, all CD data refer to the ECD spectroscopy, since these have been recorded in the UV region.

3.2.2.1. Absolute configurations from electronic CD data

Enantiomers always display opposite CD spectra.[48] This behavior is the cornerstone of the application of CD spectroscopy in the elucidation of the absolute configurations.

In fact, from the CD data, the absolute configurations can be deduced at various levels of sophistication. These include the application of semi-empirical and non-empirical CD rules,[44, 49-51] the comparison of the CD curve of the investigated compound with that of references of known absolute configuration,[52] and the comparison of experimental CD data with the predicted ones.[7, 21, 31, 33, 34]

3.2.2.1.1. Application of CD rules

The following sections provide a brief description of the most quoted CD rules in the literature, i.e., the octant rule and the exciton chirality method.

3.2.2.1.1.1. CD octant rule

The "octant rule" of saturated ketones is based on the assumption that all the substituents in the vicinity of a carbonyl function contribute to the sign of the Cotton Effect (the CD band) observed in its resonating region (n – π^* transitions), i.e., ca. 300 nm.[35] Therefore, the actual contribution of the substituents is deduced from the signs of the spatial octants (**Figure 3.3**) in which they are located.[35]

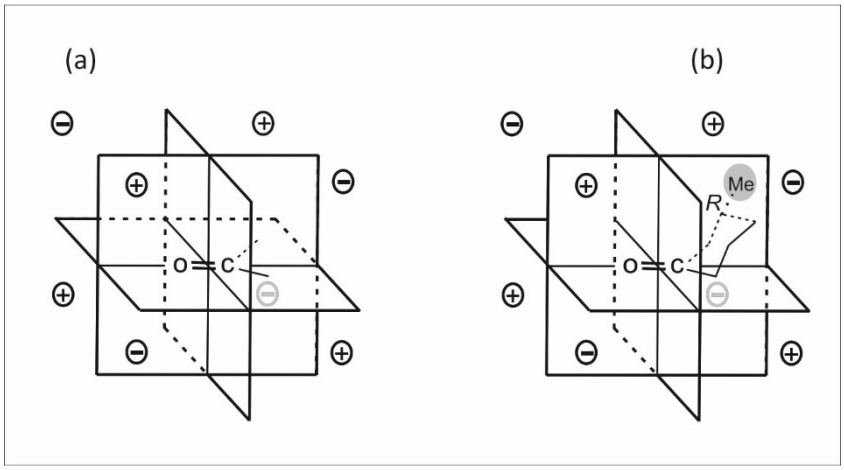

Figure 3.3: (a) Octants defined by the nodal plans of the carbonyl n and π orbitals; (b) absolute configuration assignment of 3-methylcyclohexanone from the octant rule.[35, 44]

The octant CD rule is considered as a semi-empirical technique, since the signs of the octants (**Figure 3.3**) originate from both extrapolation of experimental data and theoretical considerations.[44] The term octant actually refers to the eight spatial sectors (**Figure 3.3**) defined by the three nodal plans of the carbonyl n and π orbitals.[44]

The absolute configuration assignment of 3-methylcyclohexanone (**Figure 3.3b**) through the application of the octant rule is one of the successful study cases usually reported in the literature.[35, 44]

The 3-methylcyclohexanone experimental CD, recorded in the solvent mixture of ethyl ether/isopentane/ethanol (5: 5: 2), shows a positive signal at 284 nm with a $\Delta\varepsilon$ of +0.57.[44] From the disposal of the substituents in the signed octants, this positive CD could only be rationalized with the methyl group occupying a positive octant.[35, 44]

From the **Figure 3.3b**, it could be seen that the contributions of the enantiotopic hydrogen atoms in the positions 2 and 6 cancel each other. At the same time, it appears that the methyl in position 3 breaks the symmetry with the hydrogen in position 5. Consequently, the methyl group was assumed responsible for the overall sign of the CD in the carbonyl absorption region. As a result, only the *R*-

configuration could support the positive CD signal experimentally observed at 284 nm for 3-methylcyclohexanone. Thus, the absolute configuration was successfully assessed.[35, 44]

However, despite the success of the octant rule in the study of 3-methylcyclohexanone, the method is restricted to saturated ketones and is not universally transposable.[35, 44]

3.2.2.1.1.2. CD exciton chirality method

The absolute configuration assignment using the exciton chirality method is done according to the mutual orientation of the transition dipole moments (TDM) of chromophores that interact through space.[44, 51]

Through space dipole-dipole interactions of neighboring chromophores that have close absorption energies give rise to a splitting of the excited state(s). This splitting, known as Davydov splitting,[53] experimentally magnified in a broadened UV band and a bisignate CD couplet (**Figure 3.4**) centered on the UV_{max} wavelengths of the isolated chromophores.[44]

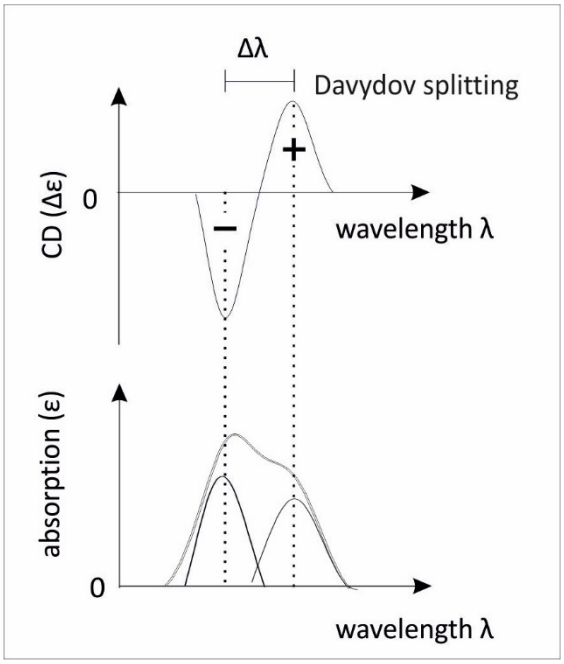

Figure 3.4: Exciton coupling of chromophores; positive couplet arbitrarily shown.[44]

As a result, the absolute configuration can be deduced from the agreement between the mutual orientation of the TDMs of the coupling chromophores and the sign of the experimental CD couplet.[44]

Conventionally, a CD couplet is considered as positive (**Figure 3.4**) when the spectrum starts – from the longer wavelengths – with a positive band (CE) before it drops into a negative one, or as negative the other way around.

In practice, a positive CD couplet is associated with a positive chirality, i.e., an absolute stereostructure where the shortest twist that brings the TDMs to align follows the clockwise turn (**See section 3.5.1.1.2.2.2, Figure 3.20**). In the case of a negative CD couplet, the absolute configuration to be considered should be the one in which the twist follows an anticlockwise fit.[44]

3.2.2.1.2. Experimental CD data versus computed CD curves

This approach is nowadays considered as the most reliable technique in elucidating the absolute configurations of chiral compounds.

Since a number of software packages have made feasible the prediction of CD spectra – from quantum-chemical formalisms,[30] the absolute configurations could consequently be deduced from the matching of the experimental CD spectrum with the ones computed for the possible enantiomers.[20, 21, 54]

The advantage of this technique lies actually in its universal applicability. In fact, quantum-chemical calculations of CD do not require the fulfillment of particular structural preconditions.

One of the limitations is the size of the investigated molecule – which affects the computational-time and thus, the feasibility of the study.

3.2.2.2. Quantum-chemical calculation of CD

3.2.2.2.1. Formalisms behind the rotatory and the oscillator strengths

3.2.2.2.1.1. Rotatory strength

Unlike the experimental CD spectra that are commonly measured and reported in terms of the molar CD ($\Delta\varepsilon$), in quantum-chemical calculations the computed quantity is the rotatory strength $\boldsymbol{R}$[30, 36] – related to the molar CD as follows,

$$\boldsymbol{R} = \frac{3hc(10^3)\ln 10}{32\pi^3 N_A} \int \frac{\Delta\varepsilon(\lambda)}{\lambda}\, d\lambda \qquad (3.10)$$

with N_A standing for the Avogadro number, h the Planck's constant, c the velocity of the light and λ the wavelength.

The rotatory strength is computed, according to the Rosenfeld equation (**Equation 3.11**), as the imaginary part of the scalar product of the electric $\boldsymbol{\mu}_{0i}$ and the magnetic $\mathbf{m}_{i0}$ dipole transition moment vectors.[17, 30, 55]

$$\boldsymbol{R}_{0i} = \mathrm{Im}\,(\boldsymbol{\mu}_{0i}.\,\mathbf{m}_{i0}) \tag{3.11}$$

Its calculation may actually be conducted following two different formalisms,[30, 56] *viz*. the dipole length (**Equation 3.12**) and the dipole velocity (**Equation 3.13**).

$$\boldsymbol{R}_{0i}^{r} = \frac{e^2\hbar}{2mc}\,\langle\psi_0|\mathbf{r}|\psi_i\rangle\cdot\langle\psi_i|\mathbf{r}\times\boldsymbol{\nabla}|\psi_0\rangle \tag{3.12}$$

$$\boldsymbol{R}_{0i}^{\nabla} = \frac{e^2\hbar^3}{2m^2c(E_i-E_0)}\,\langle\psi_0|\boldsymbol{\nabla}|\psi_i\rangle\cdot\langle\psi_i|\mathbf{r}\times\boldsymbol{\nabla}|\psi_0\rangle \tag{3.13}$$

In the above equations, $\boldsymbol{R}_{0i}^{r}$ and $\boldsymbol{R}_{0i}^{\nabla}$ stand respectively for the rotatory strengths in the dipole length and the dipole velocity formalisms. The notation "0" and "*i*" refer respectively to the ground and the ith excited state, while ψ denotes the related wave functions; *e* is the elementary charge, *c* the speed of the light, $\hbar$ the Planck's constant (divided by 2π), *m* the mass of the electron, $(E_i - E_0)$ the transition energy, **r** and **∇** the position and the gradient operators.

The difference reported between the rotatory strength formulated based on the dipole length and the dipole velocity always refer to the origin-dependence and respect of the rotatory strengths sum rule, in the first case; and to the origin-independence and lack of the sum rule respect, in the latter formalism.[21, 30]

In the framework of the present study, the rotatory strengths were computed with both the Gaussian09[57] and ORCA packages.[58] The results reported throughout this chapter issued from the dipole length formalism since this converges faster to the basis set limit.

3.2.2.2.1.2. Oscillator strength

UV and electronic CD (ECD) are intimately linked. The UV and ECD spectroscopies actually involve energetic regions where the electronic transitions occur.

The oscillator strength $\boldsymbol{f}_{0i}$ (**Equation 3.14**) is the quantity computed in the simulation of UV spectra:

$$\boldsymbol{f}_{0i} = \frac{4\pi mc}{3\hbar e^2\lambda}\,|\langle\psi_0|\boldsymbol{\mu}|\psi_i\rangle|^{\,2} \tag{3.14}$$

It is related to the UV extinction coefficient $\varepsilon(\lambda)$ via the dipole strength $\boldsymbol{D}_{0i}$,[36] which is the square of the electric dipole transition moment (**Equation 3.15**).

$$\boldsymbol{D_{0i}} = |\langle\psi_0|\boldsymbol{\mu}|\psi_i\rangle|^2 = \frac{3hc(10^3)\ln 10}{8\pi^3 N_A}\int\frac{\varepsilon(\lambda)}{\lambda}\,d\lambda \qquad (3.15)$$

3.2.2.2.2. Methods and software packages

These days, numerous methods are available for the prediction of CD spectra. These include the semi-empirical approaches such as CNDO/S and ZINDO/S, the time-dependent density functional theory (TD-DFT), the coupled-cluster theory (CC), and the combination of density functional theory with the multireference configuration interaction (DFT/MRCI).[21, 35]

Beside the accuracy/computational-time compromise, each theory has its own advantages and drawbacks, e.g., the semi-empirical methods are very fast but usually restricted to molecules for which they were parameterized; some TD-DFT functionals fail the prediction of charge-transfer (CT) and Rydberg states, the CC methods are time-demanding, especially for large molecules.[35, 55, 59, 60]

However, TD-DFT is documented as being the most prevalent method in the computation of CD spectroscopy.[21]

The accuracy of TD-DFT calculations is reported to be depending on the functional and the basis set.[44, 54] The hybrid functionals, which include a fraction of the exact Hartree-Fock exchange, e.g., B3LYP, BHLYP and PBE0, are the ones commonly employed.[21, 35, 44] This holds as well for the long-range corrected CAM-B3LYP[61, 62] and the double hybrid B2PLYP functionals.[63] The basis set usually used are of the split-valence type such as 6-31G*[64] and the Ahlrich's TZVP set.[21, 35]

In this work, the CD calculations were carried out at both semi-empirical (ZINDO/S) and TD-DFT levels. For the TD-DFT computations, the Random Phase Approximation (RPA) was used in Gaussian09[57] while the ORCA package[58] was using the Tamm-Dancoff Approximation (TDA).

3.2.2.2.3. Simulation of CD and UV curves

The computation of CD and UV does not provide line-shaped curves at once. The line-shaped spectra actually originate from few transformations of the calculated rotatory and oscillator strengths bar spectra.[65] These consist in overlaying of rotatory and oscillator strengths either with Lorentzian (**Equation 3.16**) or Gaussian (**Equation 3.17**) functions.[17, 65]

$$\Delta\varepsilon(E) = \frac{1}{2.297\times 10^{-39}}\times\frac{1}{\sqrt{\pi}}\sum_{i}^{N}\boldsymbol{E_{0i}}\,\boldsymbol{R_{0i}}\frac{\gamma}{(E-\boldsymbol{E_{0i}})^2+\gamma^2} \qquad (3.16)$$

$$\Delta\varepsilon(E) = \frac{1}{2.297 \times 10^{-39}} \times \frac{1}{\sigma\sqrt{\pi}} \sum_{i}^{N} \boldsymbol{E_{0i}}\, \boldsymbol{R_{0i}}\, exp\left[-\left\{\frac{(E - \boldsymbol{E_{0i}})}{\sigma}\right\}^2\right] \qquad (3.17)$$

In the equations above, $\boldsymbol{E_{0i}}$ denotes the transition energy to the i[th] excited state, $\boldsymbol{R_{0i}}$ represents the rotatory strength; γ and σ stand for the half bandwidths, respectively at half peak height and 1/e peak height.[17, 65]

It should be noted that the γ and σ parameters are expressed in energy units and usually located between 0.05 and 0.4 eV.[65]

In the present study, the values used for the simulation of each CD spectrum is provided (see appendix D), especially since the shape of the simulated CD curves does actually depend on either the γ or the σ value (**Figure 3.5**).

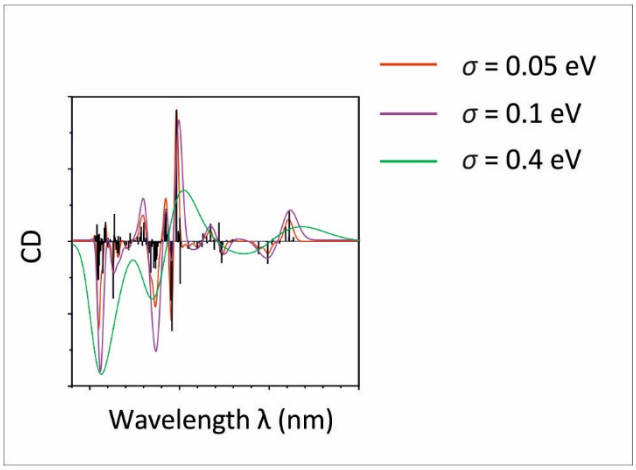

Figure 3.5: Simulation of CD curves from computed rotatory strengths (overlaying with Gaussian functions arbitrarily shown).

The simulation of the line-shaped UV curves from theoretical oscillator strengths follows a similar mechanism. The difference lies just in the substitution of the constant 1/ (2.297×10^{-39}) in the equations (3.16) and (3.17) by the factor 2.870×10^{4}, and the rotatory strength $\boldsymbol{R_{0i}}$ by the oscillator $\boldsymbol{f_{0i}}$ equivalent.[65]

3.3. General flowchart toward absolute configuration via quantum-chemical CD calculations

Basically, the principle behind the elucidation of the absolute configurations, via quantum-chemical CD calculations, relies on the matching of the experimental CD spectra with the simulated curves of the two possible enantiomers.[21, 54]

The following scheme summarizes all the steps involved in the procedure that lead to the absolute configuration assignment through quantum-chemical calculations of CD spectroscopy.

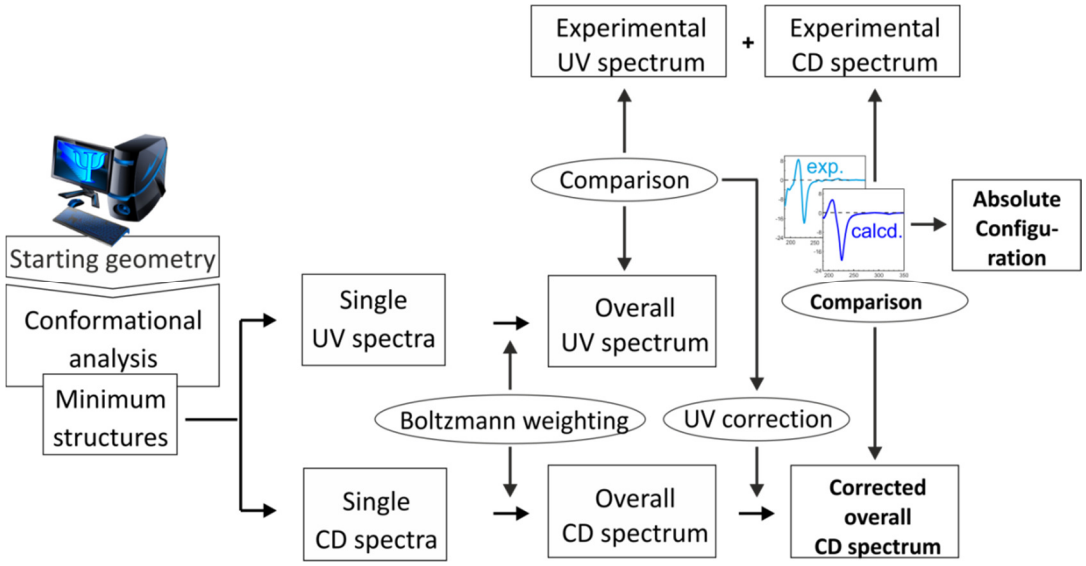

Scheme 3.1: Absolute configuration assignment through quantum-chemical CD calculations.[21]

The main steps of the above flowchart include the conformational analysis of the investigated compound, the UV and CD calculations of single conformers, UV correction of the Boltzmann weighted CD spectrum and absolute configuration assessment from the matching of the theoretical and the experimental CD spectra.

3.3.1. Conformational analysis

Prior to any computation of CD, a starting input geometry of the chiral compound is needed. This is usually one of the enantiomers (arbitrarily chosen), with the relative stereostructure established from methods such as NMR and X-ray diffraction.[20, 21, 54]

The conformational analysis is actually conducted by scanning the potential energy surface (PES) of the investigated compound, in order to find out all the relevant minima structures, i.e., the most populated conformers.[20] According to the Boltzmann statistics, these are the conformers within the energy range of 3 kcal mol^{-1} above the global minimum.[21]

This step is rationalized by the fact that CD is known to be very sensitive to the change in the spatial orientation of chromophores within the molecule.[20]

The conformational analysis of the investigated molecules was performed through the optimization of the structures obtained after manual variations of the flexible parts (e.g., dihedral angles). This was conducted sequentially with the MMFF force field,[66] the semiempirical PM6[67] and a DFT method, using the B97D functional[68] and the TZVP basis set.[69] The choice of these methods was based on its success in Prof Bringmann's laboratory. [22] Subsequently, all the conformers were confirmed as minima (single points) on the PES by the calculation of the harmonic frequencies, using the B3LYP functional[70, 71] and the 6-31 G* basis set.[64] Finally, reliable energies of the B97D conformers were computed, using the spin-component scaled MP2 calculations (SCS-MP2)[72] together with the def2-TZVP basis set,[73] in combination with the so-called RIJCOSX chain-of-spheres approximation[74-76] and the conductor-like screening (COSMO) solvent models.[77]

3.3.2. Calculation and Boltzmann averaging of single CDs and UVs

After the relevant conformers are obtained, the following step consists in performing excited states calculations. These provide the rotatory (CD) and the oscillator (UV) strengths for each single conformer.[21]

Subsequently, the single UV and CD curves are Boltzmann weighted, with respect to the conformers energies. In the present cases, the energies that were used for the Boltzmann weighting resulted from the RI-SCS-MP2/def2-TZVP calculations.[72, 73]

3.3.3. UV shift and absolute configuration assignment

Throughout the comparison of overall CD spectra with experimental CD curves, an adjustment is usually done according to the fitting of the predicted UV curves with the experimental equivalents. This procedure is referred to as UV correction.[2]

In this context, the predicted UV is shifted in order to match the experimental UV curve (**Figure 3.6**). As a result, the same shift is applied to the overall CD spectrum.

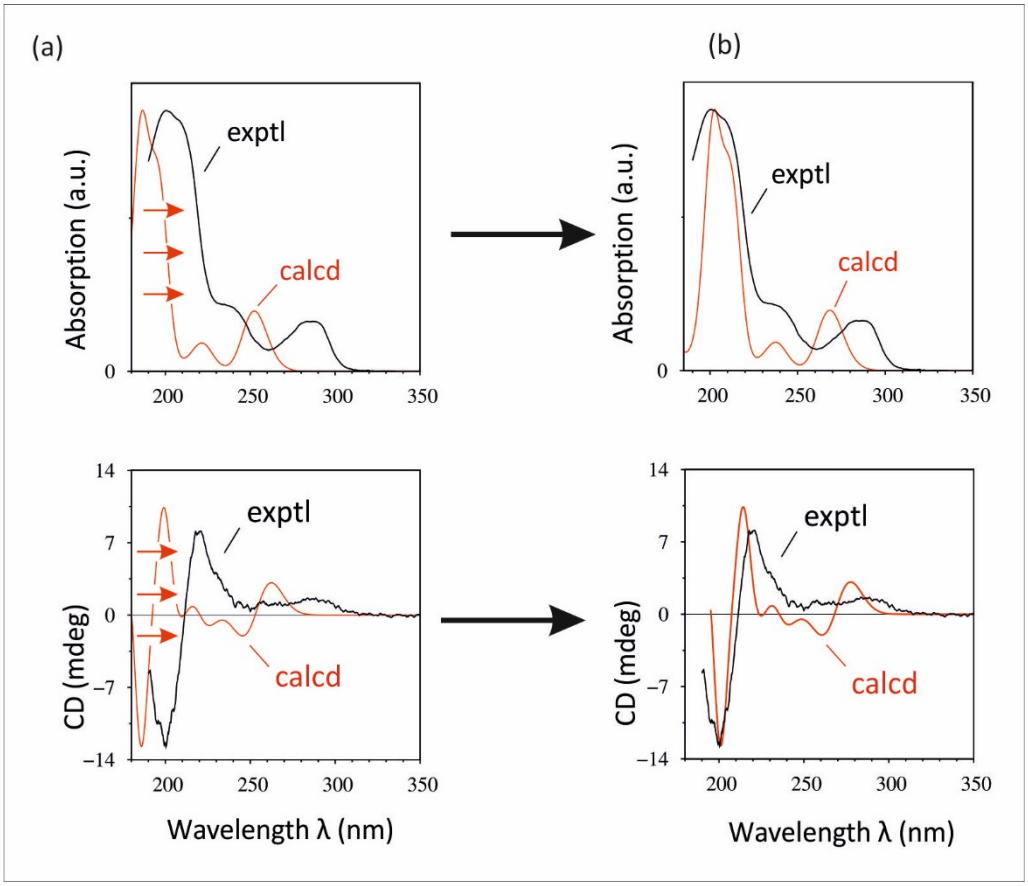

Figure 3.6: Principle of the UV shift.

Once the UV correction is applied to the overall CD curve, the absolute configuration can therefore be established from the comparison with the experimental CD spectrum. This is made feasible by the fact that enantiomers always display opposite CD curves so that only one of the two possible enantiomers, i.e., the true enantiomer, will produce a CD that is going to match with the experimental spectrum.

From the matching of the calculated CD for enantiomers with the experimental curve, the reliability of the determination of the absolute configuration is assessed by the enantiomeric similarity index (Δ_{ESI}), which shows how good the discrimination between the possible enantiomers is. This factor can actually be determined directly using the SpecDis software.[65, 78]

For the study herein reported, the UV shift values that were used in each case are given in appendix D.

3.4. Investigated compounds

The molecules whose absolute configurations are being investigated in this work have been recently isolated from mangroves species (i.e., *Xylocarpus moluccensis* and *Ceriops decandra*) and a newly discovered Congolese *Ancistrocladus* liana.

In the following sections, a brief description of each compound is provided.

3.4.1. Thaixylomolins A and B

Thaixylomolins A (**12**) and B (**13**) are natural products from the limonoid class, which consists of tetranortriterpenoid compounds (**Figure 3.7**). Limonoidic compounds are mainly found in plants from the Meliaceae and Rutaceae families.[79]

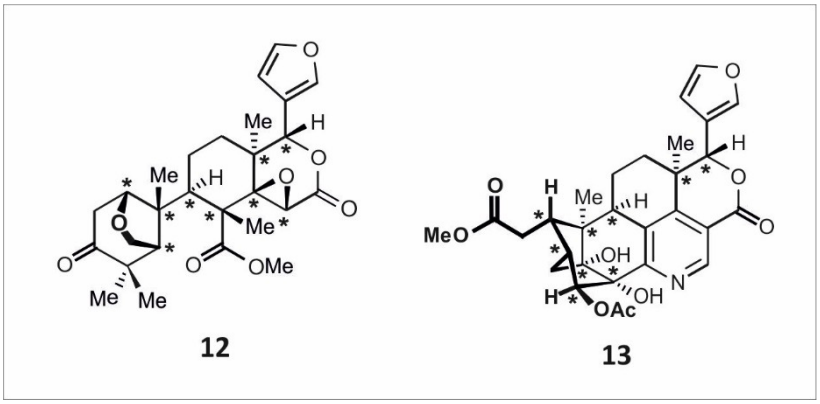

Figure 3.7: Relative configuration of thaixylomolins A (**12**) and B (**13**), (* stereocenters).

The attention paid to the research of limonoids is sustained by their wide bioactivity potential, i.e., insect antifeedant, antibacterial, antimalarial, anticancer and antiviral.[79, 80]

Thaixylomolins A (**12**) and B (**13**) were isolated by J. Li (research group of Prof. J. Wu, Guangzhou, China) from the seeds of the Thai mangrove *Xylocarpus moluccensis* (**Figure 3.8**).

Figure 3.8: *Xylocarpus moluccensis* (source: J. Li).

The relative configurations (**Figure 3.7**) were established from NMR investigations, in addition with X-ray diffraction for thaixylomolin A (**Figure 3.9**).[81]

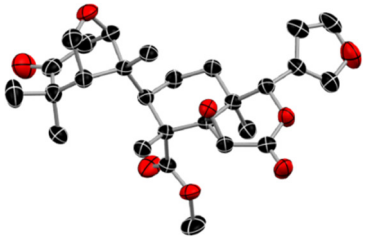

Figure 3.9: X-ray structure of thaixylomolin A (**12**); the hydrogen atoms have been omitted.

3.4.2. Decandrinin

Decandrinin (**14**) is a *seco*-abietane diterpenoid.[22] It was isolated by H. Wang (research group of Prof. J. Wu, Guangzhou, China) from the bark of *Ceriops decandra* (**Figure 3.10**), an Indian mangrove used in the Ayurvedic traditional medicine for the treatment of amoebiasis, diarrhea, hemorrhage and malignant ulcers.[22]

Figure 3.10: *Ceriops decandra* (source: H. Wang).

The relative stereostructure (**Figure 3.11**) was established from extensive NMR analysis.[22]

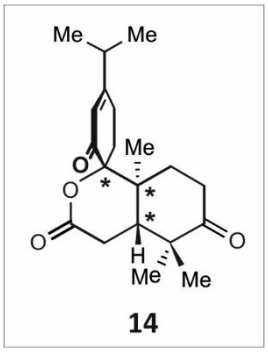

Figure 3.11: Relative configuration of decandrinin (**14**), (*stereocenters).

3.4.3. Mbandakamines A and B

Mbandakamines A (**15a**) and B (**15b**) are dimeric atropo-diastereomers of the naphthylisoquinoline (NIQ) type.[82] They have been recently isolated from a newly discovered and as yet unidentified Congolese *Ancistrocladus* species (**Figure 3.12**) by B.K. Lombe and C. Steinert (research group of Prof. G. Bringmann, University of Würzburg, Germany).

Figure 3.12: Congolese *Ancistrocladus* sp. (source: C. Steinert and B.K. Lombe).

Their relative and absolute configurations (**Figure 3.13**) were previously established from extensive NMR studies (NOESY and ROESY) and Ruthenium-mediated oxidative degradations.[82]

These proved the mbandakamines' structures to be featuring two NIQ moieties, linked via a hindered central biaryl axis.[82]

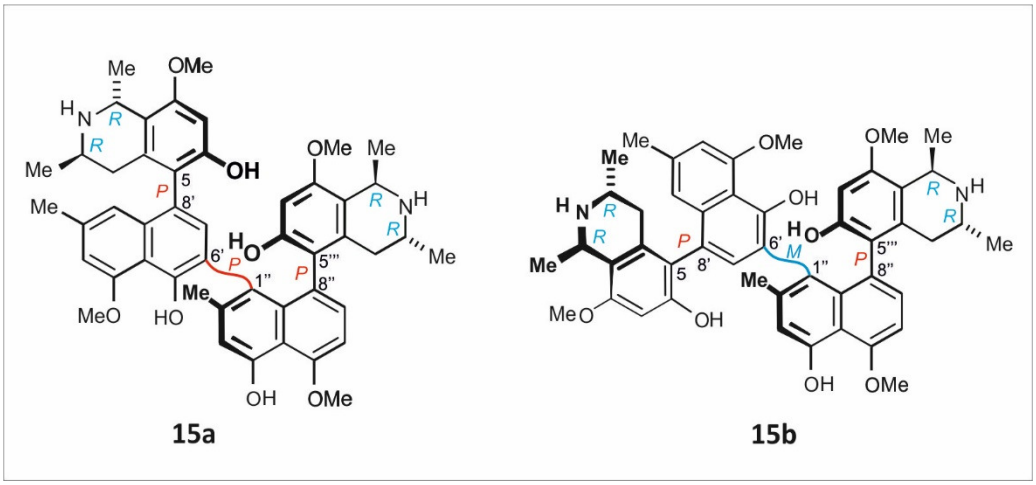

Figure 3.13: Absolute configurations of mbandakamines A (**15a**) and B (**15b**).

The purpose of this study is to confirm the already assigned absolute configurations, by conducting quantum-chemical CD calculations.

This is of a particular relevance, especially since mbandakamines A and B are the first reported NIQ dimers with an unsymmetrical coupling at the central 6'-1" biaryl axis and high antiplasmodial activities.

Most of the known dimers in the NIQ series are C_2 symmetric, e.g., ancistrogriffitine A (**16**), jozimine A_2 (**17**), korundamine A (**18**), michellamine B (**19**), shuangancistrotectorines A (**20a**) and B (**20b**).[13, 33, 83, 84]

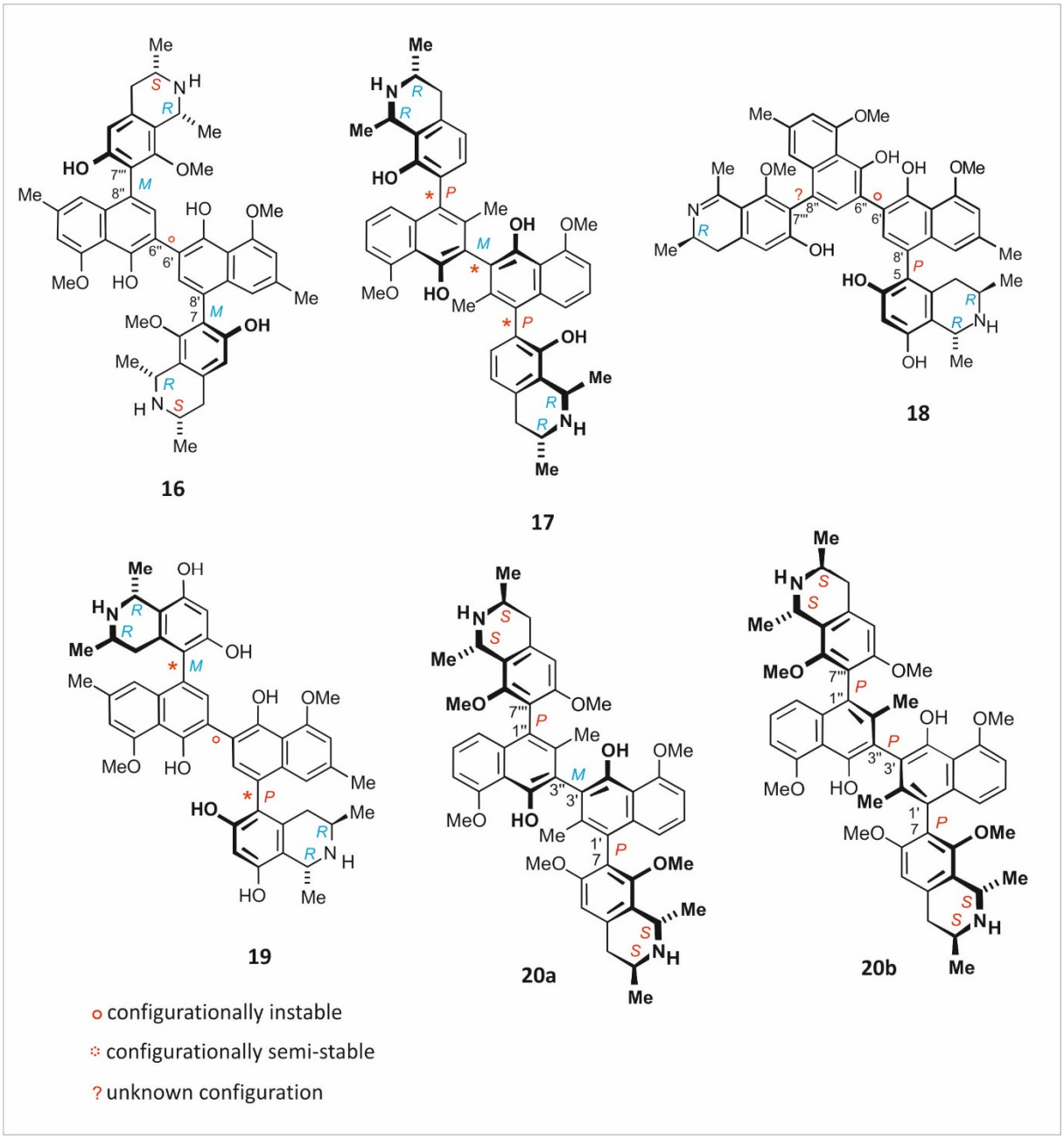

Figure 3.14: Structure of ancistrogriffitine A (**16**), jozimine A_2 (**17**), korundamine A (**18**), michellamine B (**19**), shuangancistrotectorines A (**20a**) and B (**20b**).

3.5. Results and discussion

In the following sections, the results of the quantum-chemical CD and ORD calculations are discussed and the absolute configurations are assessed thereupon.

3.5.1. Thaixylomolins A and B

The results of thaixylomolin B (**13**) CD calculations will be the first to be discussed, especially since the calculations were performed as a benchmarking that should guide the choice of the suitable method for the CD computation of limonoids featuring a pyridine moiety.

3.5.1.1. Thaixylomolin B

3.5.1.1.1. Conformational analysis

The conformational analysis of thaixylomolin B (**13**), sequentially with the MMFF force field,[66] PM6[67] and B97D/TZVP[68, 69] optimizations, yielded 9 conformers within the energy cutoff of 3 kcal mol^{-1} above the global minimum (**Table 3.1**).

Table 3.1: Relative energies of the relevant conformers of thaixylomolin B (**13**).

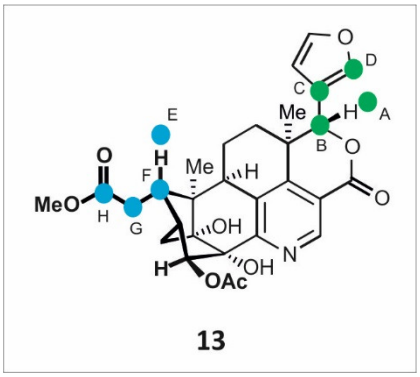

13

Conformer	ΔE (kcal mol^{-1})	Θ_{ABCD} (°)	Θ_{EFGH} (°)
Conf-1	0.00	49	-67
Conf-2	0.09	49	-144
Conf-3	0.36	-143	-67
Conf-4	0.45	49	48
Conf-5	0.52	-143	-142
Conf-6	0.81	-143	48
Conf-7	1.80	-48	-143
Conf-8	1.96	-48	-67
Conf-9	2.25	-49	48

3.5.1.1.2. CD calculations and absolute configuration assignment

3.5.1.1.2.1. ZINDO/S calculations

For each of the 9 single conformers, ZINDO/S calculations[85] provided single CD curves that were Boltzmann weighted and compared thereafter with the experimental CD spectrum (**Figure 3.15**).

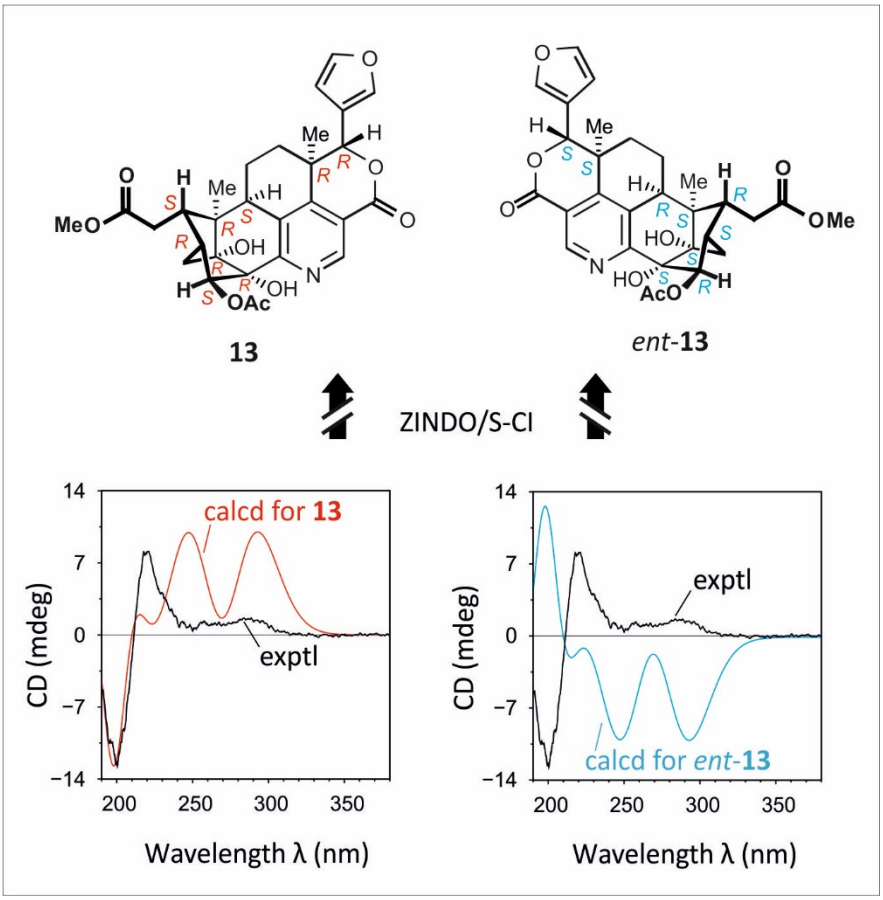

Figure 3.15: Matching of ZINDO/S CD curves of thaixylomolin B enantiomers with the experimental CD spectrum.

From the comparison of the ZINDO/S averaged CD spectra with the experimental CD curve, the absolute configuration of thaixylomolin B (**13**) could be estimated but not completely clarified. In fact, the shape of the predicted CD curve for the 1*R*,2*R*,3*S*,4*R*,5*S*,9*S*,10*R*,13*R*,17*R*-enantiomer (**13**) slightly resembled the experimental CD spectrum (**Figure 3.15**).

Unfortunately, the absolute configuration of thaixylomin B (**13**) could not be decided only based on the semiempiric ZINDO/S calculations, especially since the overall fitting of the predicted spectra to the experimental curve was almost improvable.

3.5.1.1.2.2. TD-DFT calculations

TD-DFT calculations were performed with the B3LYP,[70, 71] CAM-B3LYP[61] and B2PLYP functionals,[63] using the Gaussian09[57] and ORCA[58] software packages.

3.5.1.1.2.2.1. TDB3LYP

A. In Gaussian09

In Gaussian09,[57] the calculations were carried out with the 6-31 G* basis set.[64] As a result, none of the predicted CD curves of thaixylomolin B enantiomers could unambiguously support the CD spectrum experimentally observed. The discrimination between the enantiomers was poor and the overall fitting appeared again improvable (**Figure 3.16**).

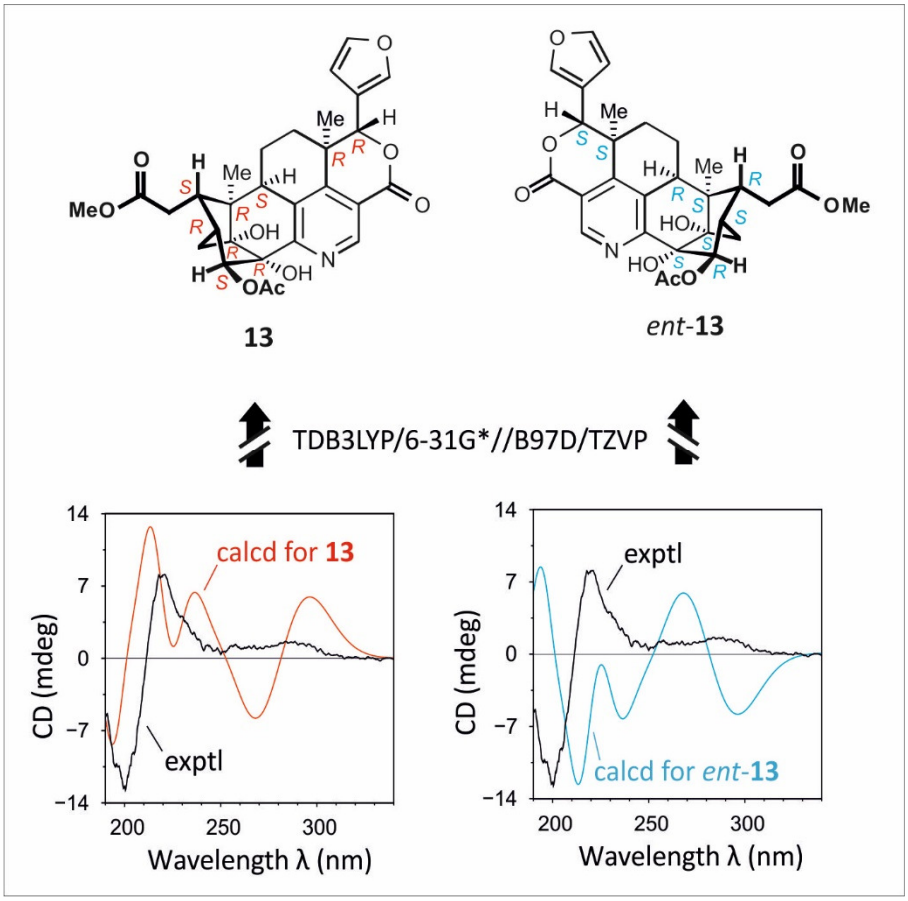

Figure 3.16: Matching of TDB3LYP/6-31G* CD of thaixylomolin B enantiomers with the experimental spectrum.

B. In ORCA

In the ORCA software,[58] the TDB3LYP calculations were achieved using the TZVP basis set[69] in combination with the RIJCOSX chain-of-spheres approximation[74-76] and the COSMO acetonitrile (ACN) solvent model.[77]

Results revealed a fair agreement between the shape of the CD predicted for the 1*R*,2*R*,3*S*,4*R*,5*S*,9*S*,10*R*,13*R*,17*R*-enantiomer (**13**) and the experimental curve (**Figure 3.17**). Unfortunately, this was not enough for an unambiguous assignment of the absolute configuration of thaixylomolin B.

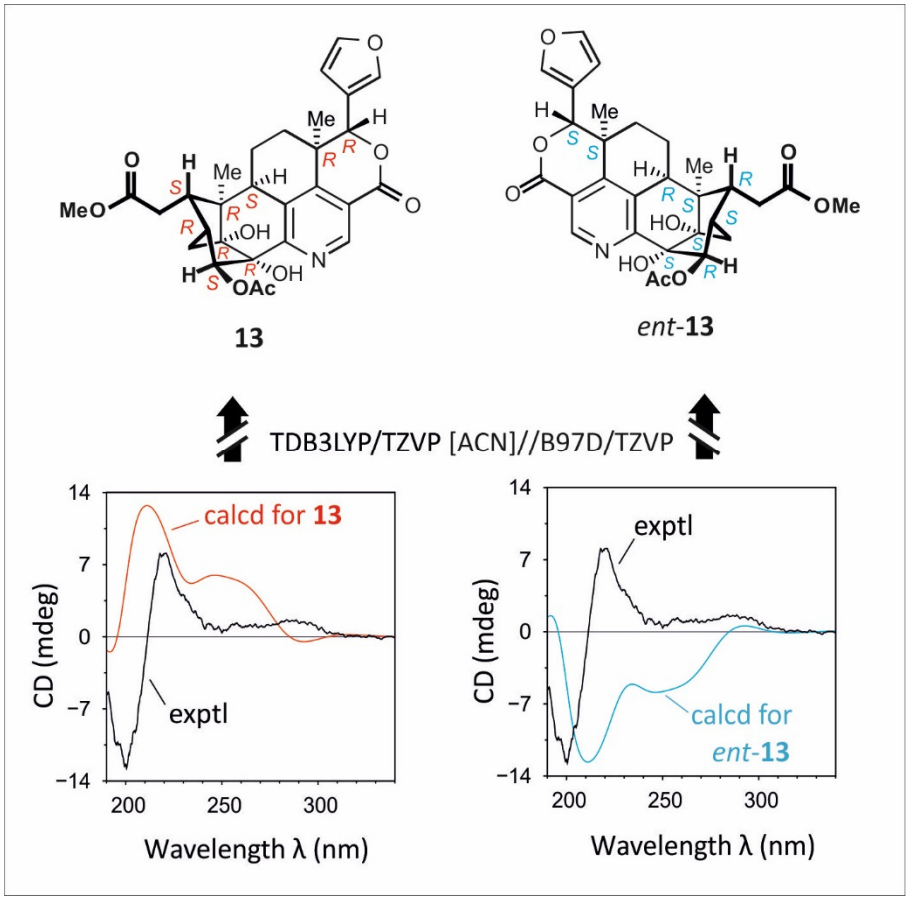

Figure 3.17: Matching of the TDB3LYP/TZVP [ACN] CD curves of the thaixylomolin B enantiomers with the experimental CD spectrum.

Henceforth, the use of the more elaborated functionals, *viz*. the CAM-B3LYP[61, 62] and the double hybrid B2PLYP[63] had been decided.

3.5.1.1.2.2.2. TDCAM-B3LYP and TDB2PLYP

TDCAM-B3LYP calculations[61, 62] were completed with the 6-31 G* basis set,[64] using exclusively the Gaussian09 software package.[57]

The averaged CD spectra that resulted from the Boltzmann weighting of the nine single CD curves were compared with the experimental CD spectrum (**Figure 3.18**).

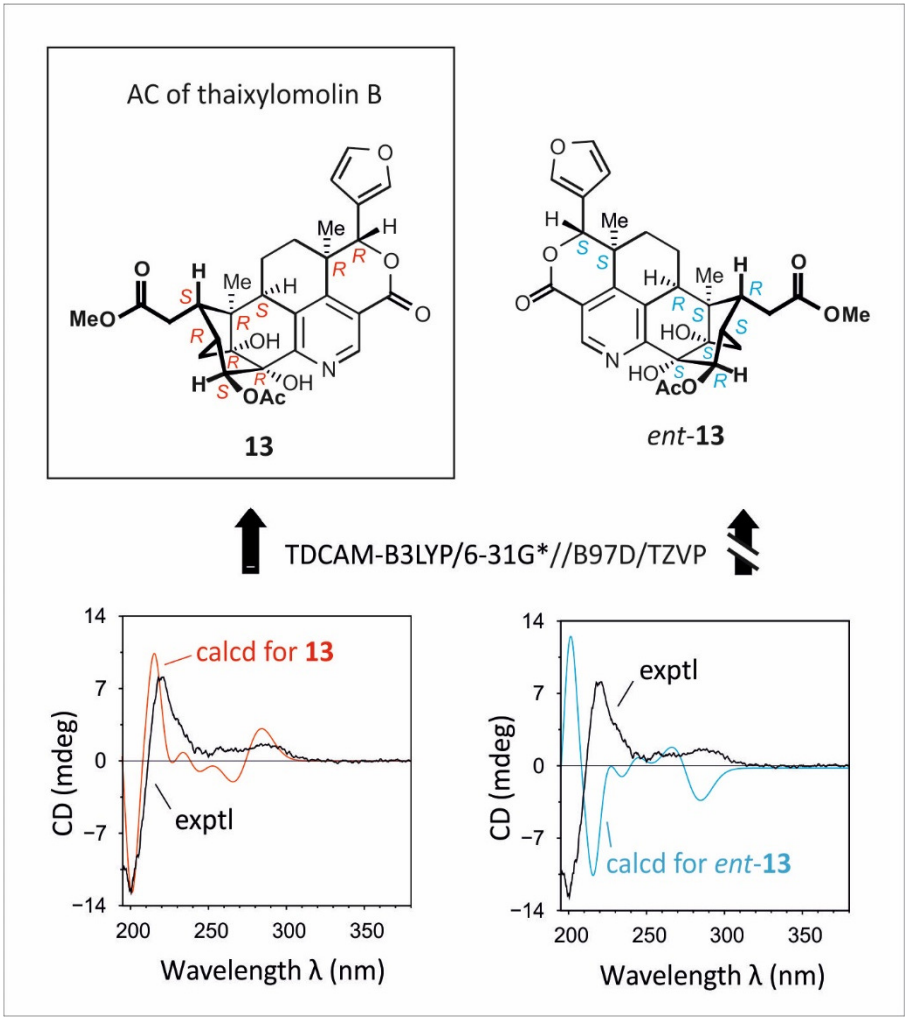

Figure 3.18: Absolute configuration assignment of thaixylomolin B through TDCAM-B3LYP/6-31G* CD calculations.

From **Figure 3.18**, a much better determination of the absolute configuration of thaixylomolin B (**13**) was possible. The method was able to accurately predict the positive couplet observed in the experimental CD spectrum.

Based on the matching of the experimental CD with that calculated for the two thaixylomolin B enantiomers, the 1*R*,2*R*,3*S*,4*R*,5*S*,9*S*,10*R*,13*R*,17*R*-enantiomer (**13**) was reliably assigned as the

absolute configuration of thaixylomolin B with a very good discrimination between the two possible enantiomers (Δ_{ESI} = 80.3%).

The above established absolute configuration of thaixylomolin B was further confirmed by TDB2PLYP/def2-TZVP calculations[46, 63, 69] which were conducted with the ORCA software package,[58] using COSMO acetonitrile solvent model and the RIJCOSX chain-of-spheres approximation (**Figure 3.19**).

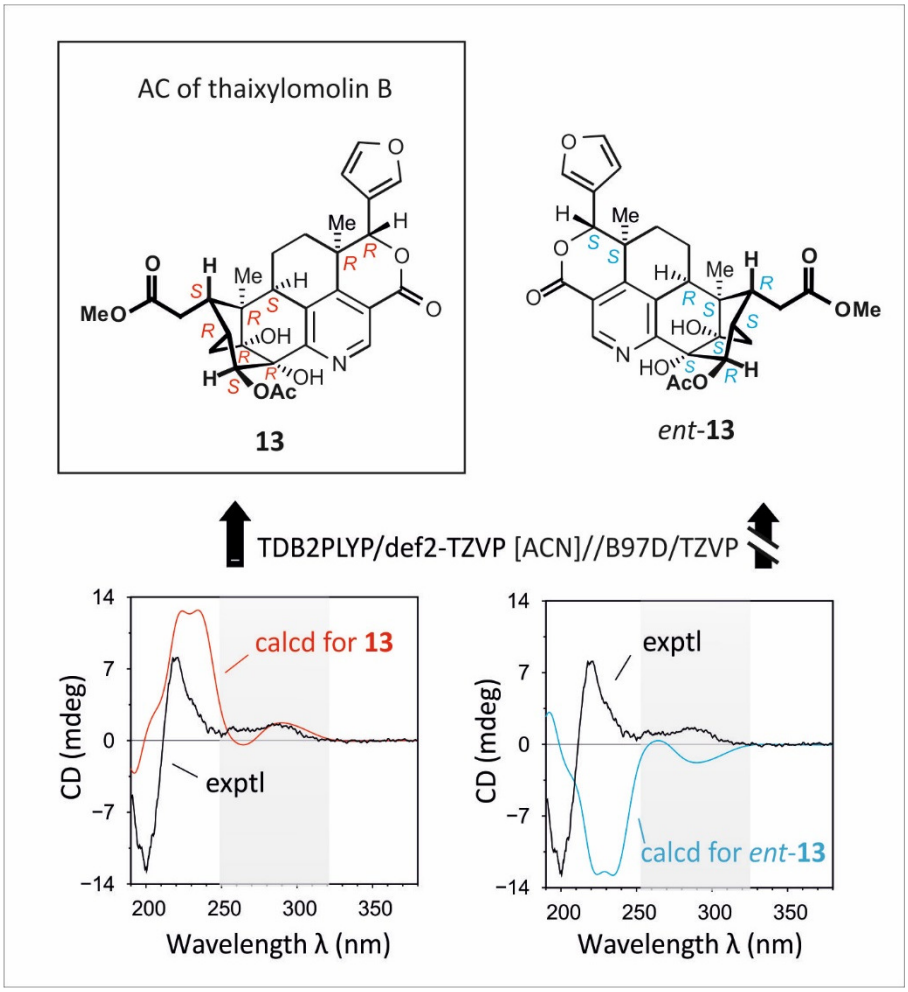

Figure 3.19: Absolute configuration assignment of thaixylomolin B from TDB2LYP/def2-TZVP CD calculations.

Results proved that TDB2PLYP/def2-TZVP computations were able to accurately reproduce the very first Cotton Effect experimentally observed (see the highlighted region in **Figure 3.19**). Accordingly, the first CE in the CD predicted for the 1*R*,2*R*,3*S*,4*R*,5*S*,9*S*,10*R*,13*R*,17*R*-enantiomer (**13**) proved to fit the experimental equivalent, while that of *ent*-(**13**) was completely a mirror-image.

The absolute configuration of thaixylomolin B, as it has been assigned from quantum-chemical circular dichroism calculations, was further corroborated by the application of the exciton chirality method, which was investigated by T. Bruhn, University of Würzburg, Germany.[81]

From the application of the exciton chiralily method, the mutual orientation of the TDMs in the coupling chromophores, *viz*. the furanyl and the nicotinic acid moieties, could support the experimental positive CD couplet only in the case of the 1*R*,2*R*,3*S*,4*R*,5*S*,9*S*,10*R*,13*R*,17*R*-enantiomer (**13**) (**Figure 3.20**).

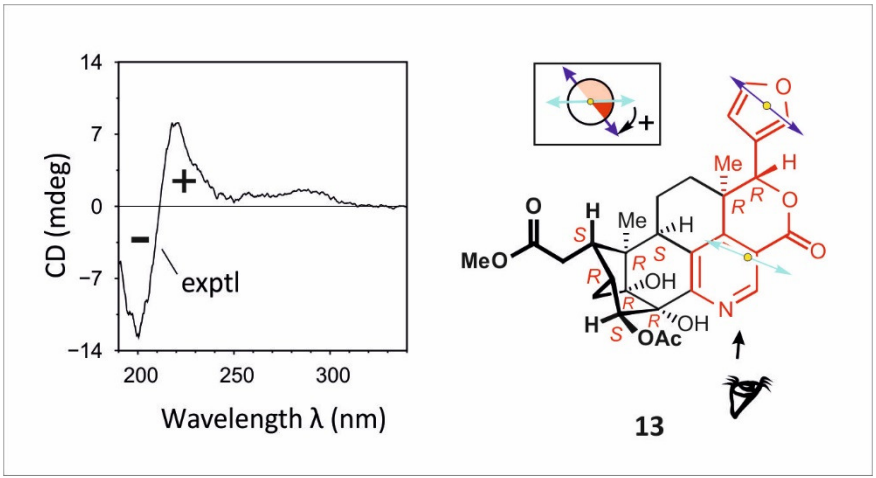

Figure 3.20: Absolute configuration assignment of thaixylomolin B (**13**) via the application of the exciton chirality method.[81]

In summary, the analysis of the results obtained from the ZINDO/S, TDB3LYP, TDCAM-B3LYP and TDB2PLYP calculations proved finally the absolute configuration of thaixylomolin B (**13**) to be 1*R*,2*R*,3*S*,4*R*,5*S*,9*S*,10*R*,13*R*,17*R*.

The benchmarking process has revealed CAM-B3LYP as the most suitable functional for the CD prediction of thaixylomolin B. In view of that, the CAM-B3LYP functional could be recommended and tested in the future for limonoids with related chromophores for the CD prediction and thus, the assignment of the absolute configuration.

3.5.1.2. Thaixylomolin A

3.5.1.2.1. Conformational analysis

The conformational analysis of thaixylomolin A (**12**), performed sequentially at the MMFF,[66] PM6[67] and B97D/TZVP levels,[68, 69] yielded three relevant conformers within the range of 3 kcal mol^{-1} above the global minimum.

The enantiomer obtained from the X-ray diffraction (**Figure 3.9**) was arbitrarily used as the starting input geometry.

Table 3.2: Relative energies of the most populated thaixylomolin A (**12**) conformers.

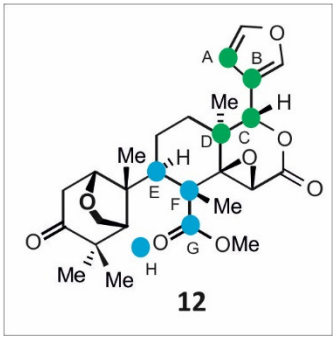

12

Conformer	ΔE (kcal mol^{-1})	Θ_{ABCD} (°)	Θ_{EFGH} (°)
Conf-1	0.00	-95	-13
Conf-2	1.17	95	172
Conf-3	1.23	-95	172

3.5.1.2.2. CD calculations and absolute configuration assignment

CD computations were conducted at the TDB2PLYP/def2-TZVP level,[63, 69] in combination with the RIJCOSX chain-of-spheres approximation[74-76] and the COSMO acetonitrile solvent model,[77] using the ORCA software package.[58]

The choice of the B2PLYP functional was basically based on previous works which proved the aforementioned functional to be suitable for the CD prediction of compounds with likewise chromophores, e.g., andhraxylocarpins A-E.[34]

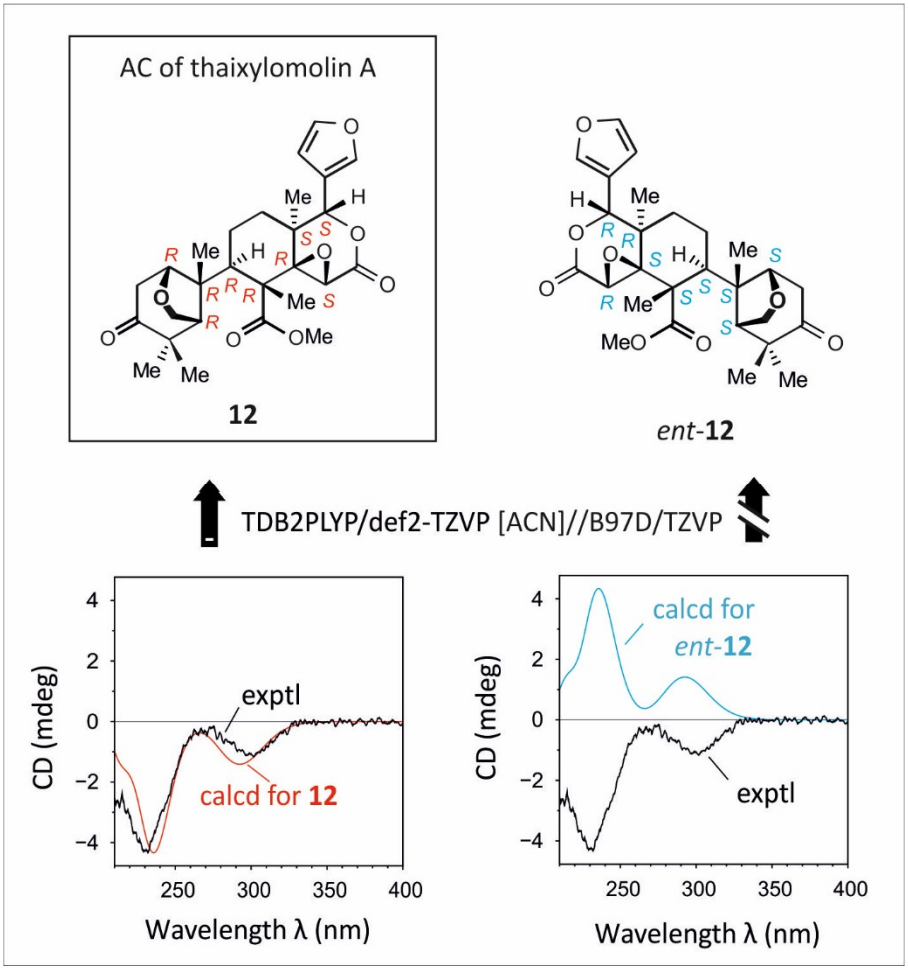

Figure 3.21: Absolute configuration assignment of thaixylomolin A through TDB2PLYP/def2-TZVP CD calculations.

Results revealed the CD predicted for the 1*R*,5*R*,8*R*,9*R*,10*R*,13*S*,14*R*,15*S*,17*S*-enantiomer (**12**) to perfectly fit the experimental curve; while in contrast, the 1*S*,5*S*,8*S*,9*S*,10*S*,13*R*,14*S*,15*R*,17*R*-enantiomer (*ent*-**12**) was displaying a mirror image curve (**Figure 3.21**). Consequently, the absolute configuration of thaixylomolin A was unambiguously assigned as 1*R*,5*R*,8*R*,9*R*,10*R*,13*S*,14*R*,15*S*,17*S*; with a very good discrimination between the two possible enantiomers (Δ_{ESI} = 86%).

3.5.2. Decandrinin

3.5.2.1. Conformational analysis

The conformational analysis of decandrinin (**14**) provided six conformers within the energetic cut-off of 3 kcal mol^{-1} above the global minimum (**Table 3.3**). This was done using the same approach, *viz*. the sequential optimization at the MMFF,[66] PM6 [67] and B97D/TZVP[68, 69] levels.

Table 3.3: Relative energies of the most populated conformers of decandrinin (**14**).

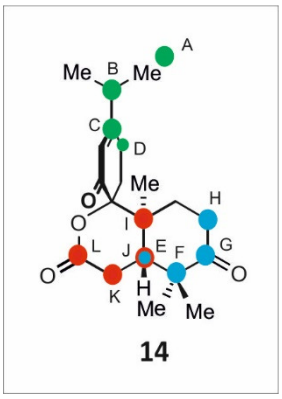

14

Conformer	ΔE (kcal mol^{-1})	Θ_{ABCD} (°)	Θ_{EFGH} (°)	Θ_{IJKL} (°)
Conf-1	0.00	-67	-45	-48
Conf-2	0.05	-68	27	-46
Conf-3	0.40	156	-45	-47
Conf-4	0.41	156	27	-46
Conf-5	2.14	-41	-121	-159
Conf-6	2.55	95	-121	-159

3.5.2.2. CD calculations and absolute configuration assignment

TDB2PLYP/def2-TZVP calculations were here again carried out in combination with the COSMO acetonitrile solvent model,[77] using the RIJCOSX chain-of-spheres approximation implemented in the ORCA software package.[58]

The single CD spectra that resulted were subsequently Boltzmann averaged and the absolute configuration assignment of decandrin was attempted from the fitting of the weighted CD curve with the experimental CD spectrum (**Figure 3.22**).

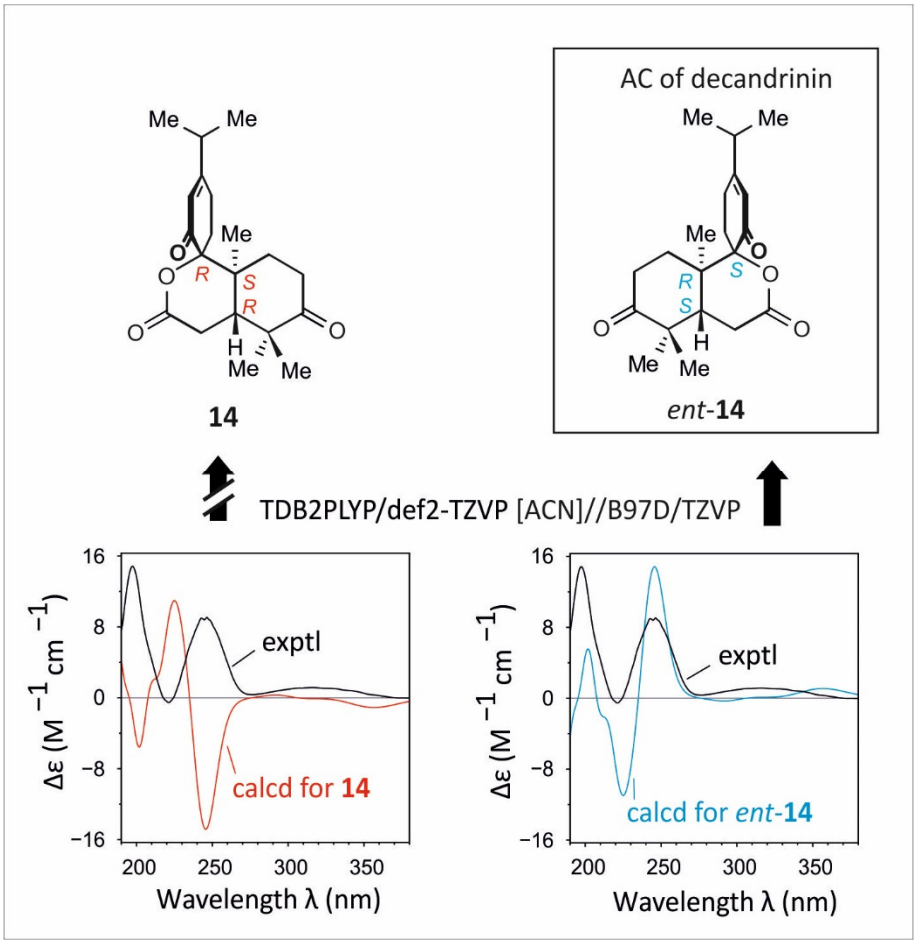

Figure 3.22: Absolute configuration assignment of decandrinin through TDB2PLYP/def2-TZVP CD calculations.

Results revealed the 5*S*,9*S*,10*R*-enantiomer (*ent*-**14**) as the most likely absolute configuration of decandrinin; based on the moderate fitting of its predicted CD curve with the experimental equivalent (**Figure 3.22**).

However, since TDB2PLYP/def2-TZVP computations yielded a low discrimination between the decandrinin's enantiomers (Δ_{ESI} = 58%), the absolute configuration could not be established unambiguously. Thus, ORD investigations were further carried out.

ORD curves of the two enantiomers, *viz*. (**14**) and (*ent*-**14**), were computed in the non-resonating region, using the PBE0/cc-pVDZ method[86, 87] and the Gaussian09 software package.

Comparison of theoretical and experimental ORD data evidenced an agreement between the experimental curve and the ORD spectrum predicted for the 5*S*,9*S*,10*R*-enantiomer (*ent*-**14**) (**Figure 3.23**). Both the theoretical ORD of 5*S*,9*S*,10*R*-enantiomer (*ent*-**14**) and the experimental curve were

displaying positive signals in the considered non-resonating region whereas the 5*R*,9*R*,10*S*-enantiomer was exhibiting negative values.

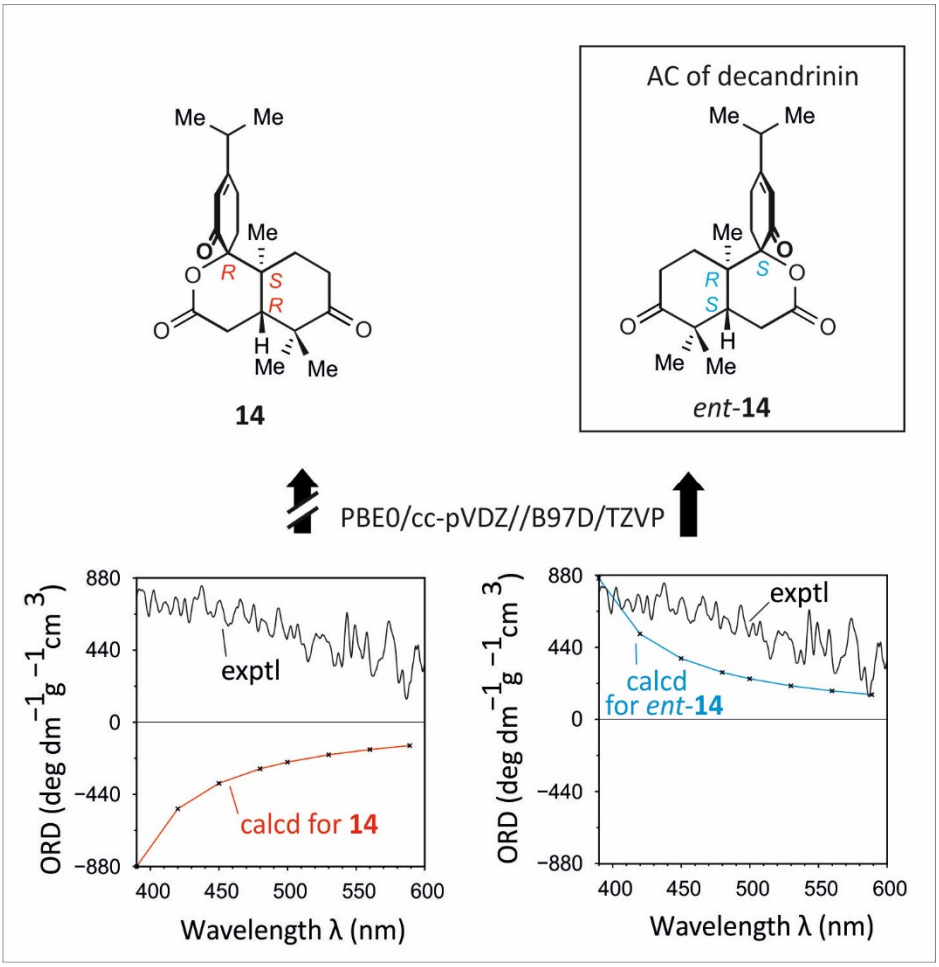

Figure 3.23: Absolute configuration assignment of decandrinin through PBE0/cc-pVDZ ORD calculations.

Accordingly, the 5*S*,9*S*,10*R*-enantiomer (*ent*-**14**) was reliably assigned as the decandrinin's absolute configuration, in addition to the results from CD calculations.

3.5.3. Mbandakamines A and B

3.5.3.1. Mbandakamine A

3.5.3.1.1. Conformational analysis

The conformational analysis of mbandakamine A (**15a**) yielded at the final stage (i.e., B97D/TZVP optimization) six relevant conformers, which were afterward subjected to CD calculations.

Table 3.4: Relative energies of the relevant conformers of mbandakamine A (**15a**).

Conformer	ΔE (kcal mol^{-1})
Conf-1	0.00
Conf-2	0.33
Conf-3	0.54
Conf-4	0.83
Conf-5	2.14
Conf-6	2.60

3.5.3.1.2. CD calculations and absolute configuration assignment

CD computations were started with a low-level theory, *viz.* the semi-empirical ZINDO/S due to the size of the mbandakamines. They are quite large molecules and this would have drastically increased the computational time, especially for high-level methods such as TD-DFT and coupled-cluster calculations.

However, despite the shortcoming related to the size, high-level TD-DFT calculations were nevertheless attempted, using the CAM-B3LYP functional and the 6-31G* basis set in Gaussian09.

3.5.3.1.2.1. ZINDO/S calculations

ZINDO/S calculations were performed on each of the six relevant conformers of mbandakamine A (**15a**), using the ORCA software package. The CDs that resulted were Boltzmann weighted and compared to the experimental curve (**Figure 3.24**).

Surprisingly, the low-level semi-empirical ZINDO/S could accurately predict the CD spectrum of mbandakamine A, which provided an excellent fitting with the experimental CD curve.

Since this investigation was aimed at confirming the already assigned absolute configurations of the mbandakamines,[82] the fitting of the predicted (ZINDO/S) and the observed CD spectrum provided further data on the confidence of the reliability of the absolute configuration assigned.

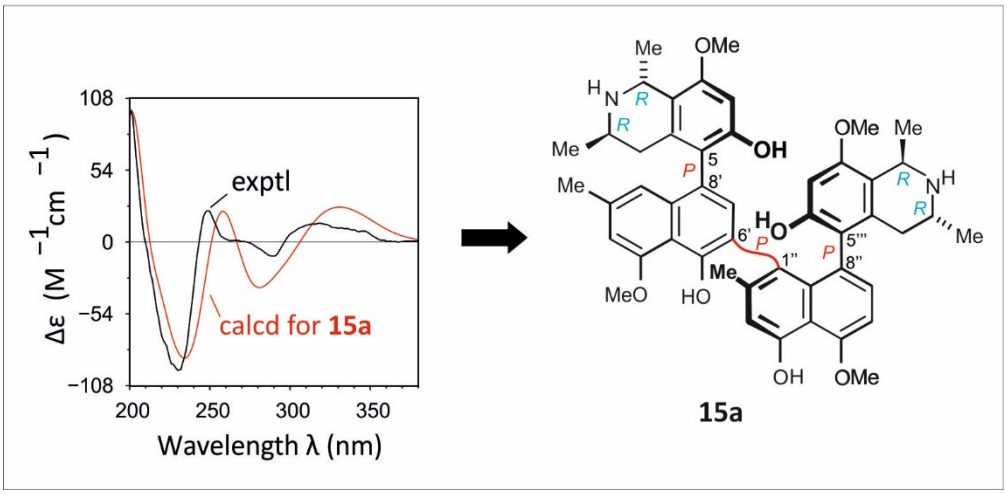

Figure 3.24: Absolute configuration assignment of mbandakamine A (**15a**) from ZINDO/S CD calculations.

3.5.3.1.2.2. TDCAM-B3LYP calculations

Comparison between the experimental CD and the Boltzmann averaged CD curve that resulted from TDCAM-B3LYP/6-31G* calculations, using the Gaussian09 software package, is provided in **Figure 3.25**.

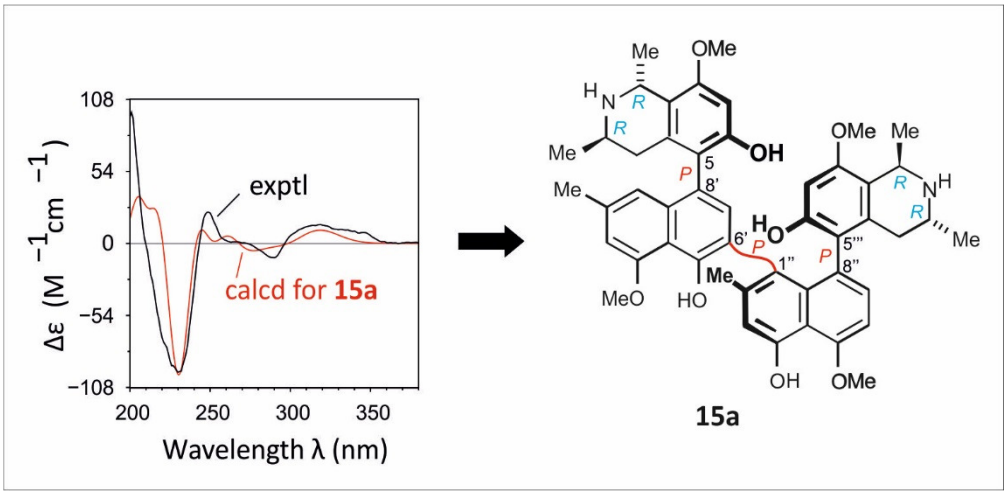

Figure 3.25: Absolute configuration assignment of mbandakamine A (**15a**) from TDCAM-B3LYP/6-31G* CD calculations.

The agreement between the TDCAM-B3LYP CD spectrum and the experimental CD curve proved again reliable in confirming the assigned absolute configuration of mbandakamine A (**15a**).

3.5.3.2. Mbandakamine B

3.5.3.2.1. Conformational analysis

Similar to that of mbandakamine A (**15a**), the conformational analysis of the atropisomer mbandakamine B (**15b**) provided six relevant conformers, on which CD computations were subsequently performed.

Table 3.5: Relative energies of the most populated conformers of mbandakamines B (**15b**).

Conformer	ΔE (kcal mol^{-1})
Conf-1	0.00
Conf-2	0.42
Conf-3	1.16
Conf-4	1.70
Conf-5	2.18
Conf-6	3.00

3.5.3.2.2. CD calculations and absolute configuration assignment

3.5.3.2.2.1. ZINDO/S calculations

Comparison between the experimental spectrum and the Boltzmann averaged curve from ZINDO/S CD calculations is shown in **Figure 3.26**.

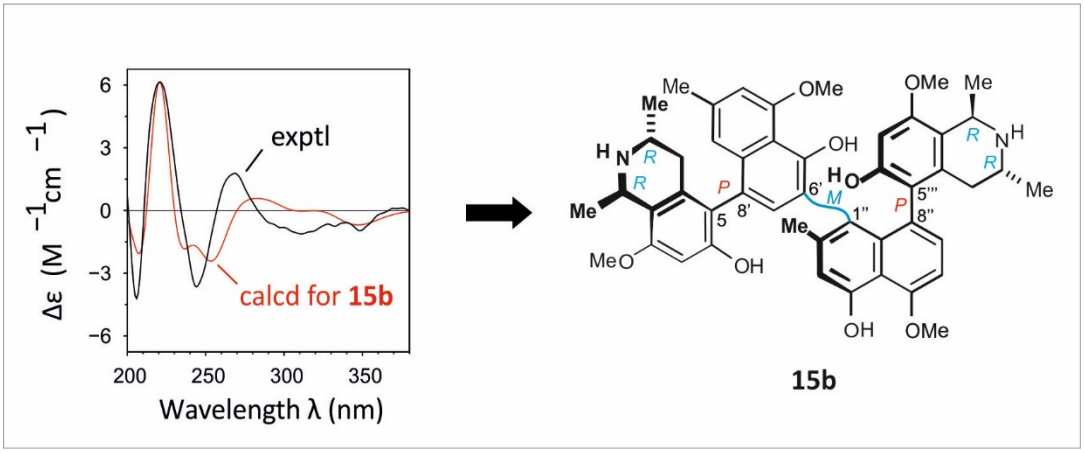

Figure 3.26: Absolute configuration assignment of mbandakamine B (**15b**) from ZINDO/S CD calculations.

Results proved the predicted CD to fit the experimental CD spectrum, thereby suggesting the consistency of the absolute configuration already assigned.[82]

3.5.3.2.2.2. TD CAM-B3LYP calculations

For a more reliable investigation, advanced TD-DFT computations were performed at the CAM-B3LYP/6-31 G* level, using the Gaussian09 software package.[57]

Comparison between the Boltzmann averaged CD spectra and the experimental curve is provided in **Figure 3.27**.

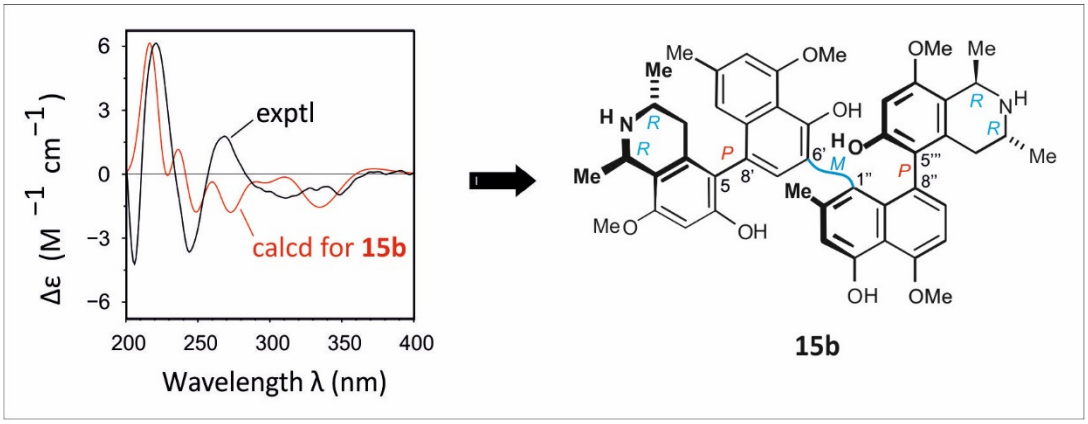

Figure 3.27: Absolute configuration investigation of mbandakamine B (**15b**) from TDCAM-B3LYP/6-31G* CD calculations.

Unfortunately, unlike in the case of mbadakamine A (**15a**), where both the CD spectra predicted at ZINDO/S and TDCAM-B3LYP levels matched the experimental curve, TDCAM-B3LYP predicted a CD of mbandakamine B (**15b**) that did not match with the experimental spectrum and whose overall fitting could not be proven (**Figure 3.27**).

In order to rationalize this, a comprehensive investigation of the electron density of the molecular orbitals involved in the excitations was conducted. This approach was supported by the fact that the commonly used functionals have well-known shortcomings (e.g., poor description of excited states with CT character).

The mapping of the electron density differences (**Figure 3.28**) between the molecular orbitals engaged in the electronic transitions, using the Chemcraft software,[88] evidenced CT character of some excitations (e.g., the 274.24 and 228.03 nm excitations).

For both the 274.24 nm and 228.03 nm transitions, TDCAM-B3LYP/6-31G* predicted wrong rotatory strengths in the case of mbandakamine B (**15b**).

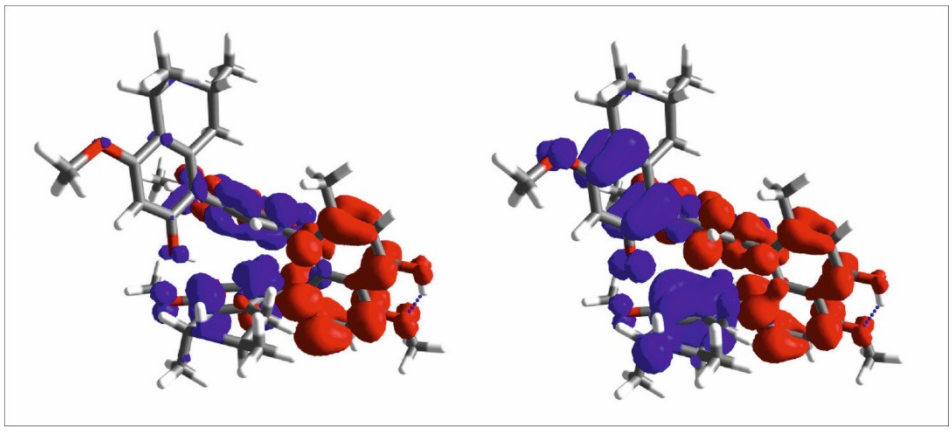

Figure 3.28: Charge transfer excitations in mbandakamine B.

The charge transfer character of the 274.24 and 228.03 nm excitations (**Figure 3.28**, left and right respectively) can be seen in the figure above.

These excitations involve two spatial regions, well-separated within the molecule: the red color indicates the region where the electron density decreases, while the blue shows the increasing of the same quantity during the excitation.

However, this unpredicted shortcoming of the CAM-B3LYP functional could be bypassed by carrying out higher computations (i.e., coupled-cluster calculations). Unfortunately, this could not be attempted mainly because of the size of the mbandakamines, which would have required extreme computational time.

With the intention to understand why the CAM-B3LYP functional successfully predicted the CD curve of mbandakamine A (**15a**) while it failed to do the same for the B atropisomer (**15b**), the plot of the electron density differences was also investigated for mbandakamine A (**Figure 3.29**).

Surprisingly, some excitations possessed the same CT character in mbandakamine A (**15a**) as well.

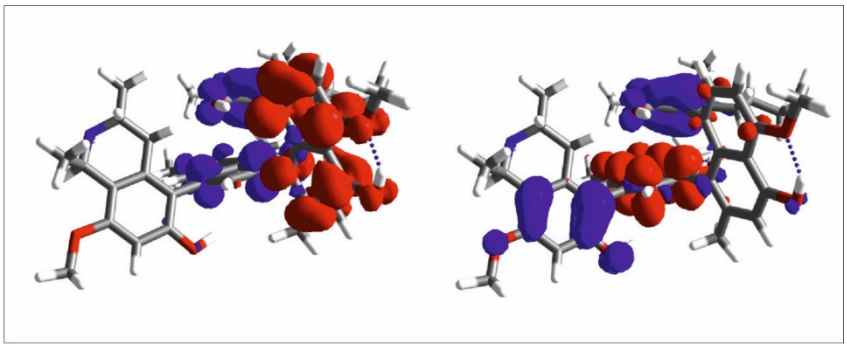

Figure 3.29: Charge transfer excitations in mbandakamine A.

Accordingly, the success of the CAM-B3LYP functional in predicting the CD of mbandakamine A, despite the CT character of certain excitations, could only be attributed to a possible cancellation of errors in the computational process.

This fact could definitely be evidenced only by performing computations with high-level theories such as coupled-cluster calculations, which could then be used reliably.

Nevertheless, if one considers the low-level ZINDO/S calculations, the absolute configuration of mbandakamine B (**15b**) as already assigned by Bringmann et al. [82] could be considered as fairly reliable, especially since the same ZINDO/S calculations successfully worked for both atropisomers (**15a** and **15b**).

3.6. Conclusion

The work presented in this chapter was aimed at elucidating the absolute configurations of some naturally occurring compounds, isolated from mangroves and Ancistrocladus plants. Specifically, *Xylocarpus moluccensis*, *Ceriops decandra* and an *Ancistrocladus* sp. collected in Mbandaka, Democratic Republic of the Congo.

Two limonoids (thaixylomolins A and B), one diterpenoid (decandrinin) and two naphthylisoquinoline alkaloids (mbandakamines A and B) were subjected to quantum-chemical circular dichroism calculations.

The approach consisted of assessing the absolute configurations according to the matching of the computed CD curves with the experimental CD spectra.

In this regard, the 1*R*,2*R*,3*S*,4*R*,5*S*,9*S*,10*R*,13*R*,17*R*-enantiomer was found to be the absolute stereostructure of thaixylomonin B (**13**), while the one for thaixylomolin A (**12**) was established as the

1*R*,5*R*,8*R*,9*R*,10*R*,13*S*,14*R*,15*S*,17*S*-enantiomer. In the case of decandrinin (**14**), CD and ORD calculations both confirmed the 5*S*,9*S*,10*R*-enantiomer as the absolute configuration.

The absolute configurations of mbandakamines A and B (**15a** and **15b**) have been verified at ZINDO/S level to be the same as the ones published.[82] However, since the more elaborate TD-DFT calculations, using the CAM-B3LYP functional and the 6-31 G* basis set, could not accurately predict the CD of mbandakamine B (presumably because of the CT character of some transitions), high-level methods such as coupled-cluster calculations have been found advisable for a more reliable absolute configuration assessment of the mbandakamines, especially for the B atropisomer.

From this work, two manuscripts have been published in high ranking journals in collaboration with partners that were involved.[22, 81]

References

[1] G. Moss, *Pure Appl. Chem.* **1996**, *68*, 2193-2222.

[2] G. Bringmann, S. Busemann in *Natural Products Analysis* (Eds.: P. Schreier, M. Herderich, H. U. Humpf, W. Schwab), Vieweg, Wiesbaden, **1998**, pp. 195-212.

[3] G. Bringmann, J. Kraus, D. Menche, K. Messer, *Tetrahedron* **1999**, *55*, 7563-7572.

[4] G. Bringmann, J. Kraus, U. Schmitt, C. Puder, A. Zeeck, *Eur. J. Org. Chem.* **2000**, *2000*, 2729-2734.

[5] M. Landoni, A. Soraci, *Curr. Drug Metab.* **2001**, *2*, 37-51.

[6] J. McConathy, M. J. Owens, *Prim. Care. Companion J. Clin. Psychiatry.* **2003**, *5*, 70-73.

[7] G. Bringmann, T. A. Gulder, M. Reichert, T. Gulder, *Chirality* **2008**, *20*, 628-642.

[8] J. M. Seco, E. Quiñoá, R. Riguera, *Tetrahedron: Asymmetry* **2001**, *12*, 2915-2925.

[9] J. M. Seco, E. Quinoá, R. Riguera, *Chem. Rev.* **2004**, *104*, 17-118.

[10] T. J. Wenzel, C. D. Chisholm, *Chirality* **2011**, *23*, 190-214.

[11] N. Harada, *Chirality* **2008**, *20*, 691-723.

[12] H. D. Flack, G. Bernardinelli, *Chirality* **2008**, *20*, 681-690.

[13] T. R. Hoye, M. Chen, B. Hoang, L. Mi, O. P. Priest, *J. Org. Chem.* **1999**, *64*, 7184-7201.

[14] D. R. Williams, D. C. Kammler, A. F. Donnell, W. R. Goundry, *Angew. Chem.* **2005**, *117*, 6873-6876.

[15] T. Yoshino, F. Ng, S. J. Danishefsky, *J. Am. Chem. Soc.* **2006**, *128*, 14185-14191.

[16] D. Slade, D. Ferreira, J. P. Marais, *Phytochemistry* **2005**, *66*, 2177-2215.

[17] P. L. Polavarapu, *Chem. Rec.* **2007**, *7*, 125-136.

[18] P. J. Stephens, F. J. Devlin, J. Pan, *Chirality* **2008**, *20*, 643-663.

[19] X. Li, D. Ferreira, Y. Ding, *Curr. Org. Chem.* **2010**, *14*, 1678-1697.

[20] G. Bringmann, D. Götz, T. Bruhn in *Comprehensive chiroptical spectroscopy* (Eds.: N. Berova, R. W. Woody, P. Polavarapu, K. Nakanishi), John Wiley & Sons, Hoboken, USA, **2012**, pp. 355-386.

[21] G. Bringmann, T. Bruhn, K. Maksimenka, Y. Hemberger, *Eur. J. Org. Chem.* **2009**, *17*, 2717-2727.

[22] H. Wang, M. Li, F. Z. Katele, T. Satyanandamurty, J. Wu, G. Bringmann, *Beilstein J. Org. Chem.* **2014**, *10*, 276-281.

[23] P. L. Polavarapu, *Chirality* **2002**, *14*, 768-781.

[24] L. Kong, P. Wang, *Chin. J. Nat. Med.* **2013**, *11*, 193-198.

[25] D. A. Allen, A. E. Tomaso Jr, O. P. Priest, D. F. Hindson, J. L. Hurlburt, *J. Chem. Educ.* **2008**, *85*, 698-700.

[26] J. Sandström, *Chirality* **2000**, *12*, 162-171.

[27] C. Diedrich, S. Grimme, *J. Phys. Chem. A* **2003**, *107*, 2524-2539.

[28] D. McCann, P. Stephens, *J. Org. Chem.* **2006**, *71*, 6074-6098.

[29] P. Stephens, D. McCann, F. Devlin, A. Smith, *J. Nat. Prod.* **2006**, *69*, 1055-1064.

[30] J. Autschbach, *Chirality* **2009**, *21*, E116-E152.

[31] G. Bringmann, K. Maksimenka, J. Mutanyatta-Comar, M. Knauer, T. Bruhn, *Tetrahedron* **2007**, *63*, 9810-9824.

[32] A. G. Petrovic, S. E. Vick, P. L. Polavarapu, *Chirality* **2008**, *20*, 501-510.

[33] M. Xu, T. Bruhn, B. Hertlein, R. Brun, A. Stich, J. Wu, G. Bringmann, *Chem. Eur. J.* **2010**, *16*, 4206-4216.

[34] J. Li, M. Li, T. Bruhn, D. C. Götz, Q. Xiao, T. Satyanandamurty, J. Wu, G. Bringmann, *Chem. Eur. J.* **2012**, *18*, 14342-14351.

[35] G. Pescitelli, L. Di Bari, N. Berova, *Chem. Soc. Rev.* **2011**, *40*, 4603-4625.

[36] G. Snatzke in *Circular Dichroism: Principles and Applications* (Eds.: K. Nakanishi, N. Berova, R. W. Woody), VCH, New York, USA, **1994**, pp. 1-38.

[37] D. G. Dimitriu, D. O. Dorohoi, *Spectrochim. Acta Mol. Biomol. Spectrosc.* **2014**, *131*, 674-677.

[38] H. Flack, *Acta Crystallogr. Sect. A* **2009**, *65*, 371-389.

[39] E. Giorgio, R. G. Viglione, R. Zanasi, C. Rosini, *J. Am. Chem. Soc.* **2004**, *126*, 12968-12976.

[40] H. Musso, W. Steckelberg, *Justus Liebigs Ann. Chem.* **1966**, *693*, 187-196.

[41] L. A. Mitscher, Y. H. Park, D. Clark, J. L. Beal, *J. Nat. Prod.* **1980**, *43*, 259-269.

[42] S. Grimme, A. Bahlmann, G. Haufe, *Chirality* **2002**, *14*, 793-797.

[43] P. L. Polavarapu, J. He, J. Crassous, K. Ruud, *Chem. Phys. Chem.* **2005**, *6*, 2535-2540.

[44] N. Berova, L. Di Bari, G. Pescitelli, *Chem. Soc. Rev.* **2007**, *36*, 914-931.

[45] A. Moscowitz in *Modern Quantum Chemistry* (Ed.: O. Sinanoglu), Academic Press, New York, USA, **1965**, pp. 1-4.

[46] L. Goerigk, S. Grimme, *J. Phys. Chem. A* **2008**, *113*, 767-776.

[47] G. Magyarfalvi, G. Tarczay, E. Vass, *Wiley Interdiscip. Rev. Comput. Mol. Sci.* **2011**, *1*, 403-425.

[48] S. Knoppe, I. Dolamic, A. Dass, T. Bürgi, *Angew. Chem. Int. Ed.* **2012**, *51*, 7589-7591.

[49] W. Moffitt, R. Woodward, A. Moscowitz, W. t. Klyne, C. Djerassi, *J. Am. Chem. Soc.* **1961**, *83*, 4013-4018.

[50] N. Harada, K. Nakanishi, *Acc. Chem. Res.* **1972**, *5*, 257-263.

[51] N. Harada, K. Nakanishi, N. Berova in *Comprehensive chiroptical spectroscopy* (Eds.: N. Berova, R. W. Woody, P. Polavarapu, K. Nakanishi), John Wiley & Sons, Hoboken, USA, **2012**, pp. 115-166.

[52] G. Bringmann, M. Dreyer, H. Rischer, K. Wolf, H. A. Hadi, R. Brun, H. Meimberg, G. Heubl, *J. Nat. Prod.* **2004**, *67*, 2058-2062.

[53] A. Davydov, *Zhur. Eksptl. Teoret. Fiz* **1948**, *18*, 201-209.

[54] A. E. Nugroho, H. Morita, *J. Nat. Med.* **2014**, *68*, 1-10.

[55] C. Bertucci, D. Tedesco, *J. Chromatogr. A* **2012**, *1269*, 69-81.

[56] R. A. Harris, *J. Chem. Phys.* **1969**, *50*, 3947-3951.

[57] M. J. Frisch, G. W. Trucks, H. B. Schlegel, G. E. Scuseria, M. A. Robb, J. R. Cheeseman, G. Scalmani, V. Barone, B. Mennucci, G. A. Petersson, H. Nakatsuji, M. Caricato, X. Li, H. P. Hratchian, A. F. Izmaylov, J. Bloino, G. Zheng, J. L. Sonnenberg, M. Hada, M. Ehara, K. Toyota, R. Fukuda, J. Hasegawa, M. Ishida, T. Nakajima, Y. Honda, O. Kitao, H. Nakai, T. Vreven, J. A. Montgomery, J. E. Peralta, F. Ogliaro, M. Bearpark, J. J. Heyd, E. Brothers, K. N. Kudin, V. N. Staroverov, T. Keith, R. Kobayashi, J. Normand, K. Raghavachari, A. Rendell, J. C. Burant, S. S. Iyengar, J. Tomasi, M. Cossi, N. Rega, J. M. Millam, M. Klene, J. E. Knox, J. B. Cross, V. Bakken, C. Adamo, J. Jaramillo, R. Gomperts, R. E. Stratmann, O. Yazyev, A. J. Austin, R. Cammi, C. Pomelli, J. W. Ochterski, R. L. Martin, K. Morokuma, V. G. Zakrzewski, G. A. Voth, P. Salvador, J. J. Dannenberg, S. Dapprich, A. D. Daniels, O. Farkas, J. B. Foresman, J. V. Ortiz, J. Cioslowski, D. J. Fox in *Gaussian 09,* revision B.01, Gaussian, Inc., Wallingford CT, **2010**.

[58] F. Neese, *Wiley Interdiscip. Rev. Comput. Mol. Sci.* **2012**, *2*, 73-78.

[59] A. Dreuw, J. L. Weisman, M. Head-Gordon, *J. Chem. Phys.* **2003**, *119*, 2943-2946.

[60] M. J. Peach, P. Benfield, T. Helgaker, D. J. Tozer, *J. Chem. Phys.* **2008**, *128*, 044118-044118-8.

[61] T. Yanai, D. P. Tew, N. C. Handy, *Chem. Phys. Lett.* **2004**, *393*, 51-57.

[62] D. Shcherbin, K. Ruud, *Chem. Phys.* **2008**, *349*, 234-243.

[63] S. Grimme, F. Neese, *J. Chem. Phys.* **2007**, *127*, 154116-154116-18.

[64] P. C. Hariharan, J. A. Pople, *Theor. Chim. Acta* **1973**, *28*, 213-222.

[65] T. Bruhn, A. Schaumlöffel, Y. Hemberger, G. Bringmann, *Chirality* **2013**, *25*, 243-249.

[66] T. A. Halgren, *J. Comput. Chem.* **1996**, *17*, 490-519.

[67] J. J. Stewart, *J. Mol. Mod.* **2007**, *13*, 1173-1213.

[68] S. Grimme, *J. Comput. Chem.* **2006**, *27*, 1787-1799.

[69] A. Schäfer, C. Huber, R. Ahlrichs, *J. Chem. Phys.* **1994**, *100*, 5829-5835.

[70] A. D. Becke, *J. Chem. Phys.* **1993**, *98*, 5648-5652.

[71] C. Lee, W. Yang, R. G. Parr, *Phys. Rev. B* **1988**, *37*, 785-789.

[72] M. Gerenkamp, S. Grimme, *Chem. Phys. Lett.* **2004**, *392*, 229-235.

[73] F. Weigend, R. Ahlrichs, *Phys. Chem. Chem. Phys.* **2005**, *7*, 3297-3305.

[74] F. Neese, F. Wennmohs, A. Hansen, U. Becker, *Chem. Phys.* **2009**, *356*, 98-109.

[75] S. Kossmann, F. Neese, *J. Chem. Theory Comput.* **2010**, *6*, 2325-2338.

[76] T. Petrenko, S. Kossmann, F. Neese, *J. Chem. Phys.* **2011**, *134*, 054116-054129.

[77] J. Tomasi, E. Cancès, C. S. Pomelli, M. Caricato, G. Scalmani, M. J. Frisch, R. Cammi, M. V. Basilevsky, G. N. Chuev, B. Mennucci in *Continuum Solvation Models in Chemical Physics: From Theory to Applications* (Eds.: B. Mennucci, R. Cammi), John Wiley & Sons, Chichester, UK, ***2007***, pp. 1-123.

[78] T. Bruhn, A. Schaumlöffel, Y. Hemberger, G. Bringmann, *SpecDis version 1.53*, *University of Wuerzburg*, Germany, **2012**.

[79] A. Roy, S. Saraf, *Biol. Pharm. Bull.* **2006**, *29*, 191-201.

[80] Q. Tan, X. Luo, *Chem. Rev.* **2011**, *111*, 7437-7522.

[81] J. Li, M. Li, T. Bruhn, F. Z. Katele, Q. Xiao, P. Pedpradab, J. Wu, G. Bringmann, *Org. Lett.* **2013**, *15*, 3682-3685.

[82] G. Bringmann, B. K. Lombe, C. Steinert, K. N. Ioset, R. Brun, F. Turini, G. Heubl, V. Mudogo, *Org. Lett.* **2013**, *15*, 2590-2593.

[83] P. D. Hobbs, V. Upender, J. Liu, D. J. Pollart, D. W. Thomas, M. I. Dawson, *Chem. Commun.* **1996**, 923-924.

[84] G. Bringmann, S. Harmsen, J. Holenz, T. Geuder, R. Götz, P. A Keller, R. Walter, Y. F Hallock, J. H Cardellina II, M. R Boyd, *Tetrahedron* **1994**, *50*, 9643-9648.

[85] J. Ridley, M. Zerner, *Theor. Chim. Acta* **1973**, *32*, 111-134.

[86] C. Adamo, V. Barone, *J. Chem. Phys.* **1999**, *110*, 6158-6170.

[87] T. H. Dunning Jr, *J. Chem. Phys.* **1989**, *90*, 1007-1023.

[88] G. Zhurko, D. Zhurko, *ChemCraft version 1.6*, **2009**.

Chapter 4

General conclusion

The work reported in the present dissertation was aimed at investigating the differences and or similarities between the chemical profiles of extracts from wild and cultivated plants of African ginger; as well as assessing the absolute configurations of chiral natural products isolated from mangrove plants (i.e., *Xylocarpus moluccensis* and *Ceriops decandra*) and a newly discovered but as yet unidentified Congolese *Ancistrocladus* species.

The chemical profiling study which was conducted using hyphenated UPLC MS and GC MS chromatographic techniques revealed clear similarities, but also unambiguous differences between wild and cultivated African ginger plants. The investigation has highlighted a non-reported, but highly relevant finding, responsible for several misreports in a number of previous publications. In alignment with previous studies the results have confirmed that extracts of wild and cultivated plants of African ginger to both contain the same major ingredient, i.e., a characteristic furanoterpenoid (**4**) known as Siphonochilone[1] but in contrast demonstrated an autoxidation process through which this furanoterpenoid (**4**) is degraded to produce closely related sesquiterpenoid artefacts {*viz*., the hydroxyfuranoterpenoid (**5**) and the hydroxylactone (**6**)} which have been previously reported in publications as naturally occurring in the plants.[1, 2]

The furanoterpenoid (**4**) was found to be highly unstable and the study clearly demonstrated that it in all likelihood degrades through autoxidation. This was demonstrated for both the pure crystals of the compound and in the dried rhizomes. In the latter case it was shown to gradually convert into artefacts during the storage at room temperature of the dried and powdered plants.

These results suggest that for any future work to be conducted on dried, powdered and stored plants, cognizance of the finding that processed stored rhizomes do not exhibit the same chemical profile as fresh African ginger plants, must be taken into consideration.

Moreover drying the plant was found to result in a substantial loss of eucalyptol, a monoterpene with reported anti-asthmatic properties.[3, 4] It is therefore recommended that the eucalyptol content in extracts prepared from processed rhizomes, especially for the validation of the anti-asthma activity of African ginger, should be taken into consideration including further investigation on the effect of drying the plants on the biological activity.

The assignment of the absolute configurations of the limoinoids thaixylomolin A (**12**) and B (**13**) (isolated from the Thai mangrove *Xylocarpus moluccensis*), the diterpenoid decandrinin (**14**) (purified from the Indian mangrove *Ceriops decandra*) and the naphthylisoquinoline atropisomers mbandakamine A (**15a**) and B (**15b**) (obtained from a Congolese *Ancistrocladus* sp.) was conducted by means of quantum-chemical circular dichroism calculations. The approach consisted in comparing the predicted CD curves for the possible enantiomers with the spectrum experimentally observed.

The results have unambiguously proved the absolute configuration of thaixylomolin A (**12**) to be 1*R*,5*R*,8*R*,9*R*,10*R*,13*S*,14*R*,15*S*,17*S* and that of thaixylomolin B (**13**) as 1*R*,2*R*,3*S*,4*R*,5*S*,9*S*,10*R*,13*R*,17*R*. decandrinin (**14**) was found to be 5*S*,9*S*,10*R*-configured.

The study has revealed TDCAM-B3LYP/6-31G* to be very suitable for CD predictions of a limonoidic compound with chromophores featuring pyridine and nicotinic acid moieties (e.g., thaixylomolin B) and therefore suggests it as a reliable TD-DFT method for compounds with likewise absorbing groups.

Although TDCAM-B3LYP/6-31G* calculations were not conclusive for mbandakamine B (**14b**) due to the CT character of several excitations, the semi-empirical ZINDO/S could reliably confirm the absolute configurations of the mbandakamines A (**14a**) and B (**14b**) to be in agreement with data published by Bringmann et al.[5] However, the recommendation is to perform CD calculations with high-level theories such as the coupled-cluster method (CC), to bypass failures encountered with the CAM-B3LYP functional for mbandakamine B (**14b**). This could not be done due to both, the time constraint and the molecular size of the mbandakamines.

From the work reported herein, two articles had been published in peer-reviewed and high-ranking journals.[6, 7]

References

[1] C. W. Holzapfel, W. Marais, P. L. Wessels, B. Van Wyk, *Phytochemistry* **2002**, *59*, 405-407.

[2] C. A. Lategan, W. E. Campbell, T. Seaman, P. J. Smith, *J. Ethnopharmacol.* **2009**, *121*, 92-97.

[3] U. R. Juergens, U. Dethlefsen, G. Steinkamp, A. Gillissen, R. Repges, H. Vetter, *Respir. Med.* **2003**, *97*, 250-256.

[4] U. R. Juergens, M. Stober, H. Vetter, *Eur. J. Med. Res.* **1998**, *3*, 508-510.

[5] G. Bringmann, B. K. Lombe, C. Steinert, K. N. Ioset, R. Brun, F. Turini, G. Heubl, V. Mudogo, *Org. Lett.* **2013**, *15*, 2590-2593.

[6] J. Li, M. Li, T. Bruhn, F. Z. Katele, Q. Xiao, P. Pedpradab, J. Wu, G. Bringmann, *Org. Lett.* **2013**, *15*, 3682-3685.

[7] H. Wang, M. Li, F. Z. Katele, T. Satyanandamurty, J. Wu, G. Bringmann, *Beilstein J. Org. Chem.* **2014**, *10*, 276-281.

Appendix

A. X-ray crystallography data

A.1: Crystallographic data for the furanoterpenoid (**4**).

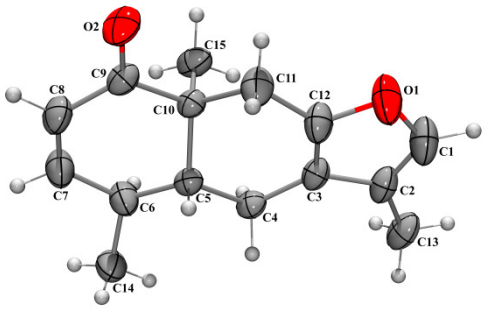

A.1.1: Crystal data.

Chemical formula	$C_{15}H_{18}O_2$	
Molecular weight	230.29 g mol $^{-1}$	
Crystal size	0.071 x 0.220 x 0.223 mm	
Crystal habit	colorless thick-plate	
Crystal system	orthorhombic	
Space group	P 21 21 21	
Unit cell dimensions	a = 7.92774(17) Å	α = 90°
	b = 12.2063(3) Å	β = 90°
	c = 13.3886(3) Å	γ = 90°
Volume	1295.59(5) Å^3	
Z	4	
Density (calculated)	1.181 g cm^{-3}	
Absorption coefficient	0.608 mm^{-1}	
F(000)	496	

Tab

A.1.2: Bond lengths.

Bond	Length (Å)	Bond	Length (Å)	Bond	Length (Å)	Bond	Length (Å)
O1-C12	1.361(4)	C8-H8	0.95(3)	C1-C2	1.327(5)	C10-C11	1.536(3)
O2-C9	1.218(3)	C10-C15	1.537(3)	C2-C3	1.436(3)	C11-H11A	1.00(4)
C1-H1	0.97(5)	C11-C12	1.490(4)	C3-C12	1.331(4)	C13-H13A	0.96
C2-C13	1.496(4)	C11-H11B	0.86(4)	C4-C5	1.543(3)	C13-H13C	0.96
C3-C4	1.481(4)	C13-H13B	0.96	C4-H4B	1.01(3)	C14A-H14B	0.96
C4-H4	0.98(3)	C14A-H14A	0.96	C5-C10	1.544(3)	C14B-H14D	0.96
C5-C6	1.527(4)	C14A-H14C	0.96	C6-C14B	1.459(12)	C14B-H14F	0.96
C5-H5	0.96(3)	C14B-H14E	0.96	C6-C14A	1.70(3)	C15-H15B	0.96
C6-C7	1.492(4)	C15-H15A	0.96	C7-C8	1.316(4)		
C6-H6	0.92(4)	C15-H15C	0.96	C8-C9	1.449(4)		
C7-H7	0.95(5)	O1-C1	1.370(5)	C9-C10	1.524(3)		

A.1.3: Bond angles.

Attached atoms	Angle (°)	Attached atoms	Angle (°)	Attached atoms	Angle (°)
C12-O1-C1	104.9(3)	C3-C12-O1	111.2(3)	C7-C6-C14A	108.1(7)
C2-C1-H1	135.(3)	O1-C12-C11	120.8(3)	C14B-C6-H6	93.(3)
C1-C2-C3	105.2(3)	C2-C13-H13B	109.5	C5-C6-H6	104.(2)
C3-C2-C13	126.8(3)	C2-C13-H13C	109.5	C8-C7-C6	124.6(3)
C12-C3-C4	122.2(2)	H13B-C13-H13C	109.5	C6-C7-H7	117.(3)
C3-C4-C5	111.60(19)	C6-C14A-H14B	109.5	C7-C8-H8	124.6(19)
C5-C4-H4	108.0(19)	C6-C14A-H14C	109.4	O2-C9-C8	120.8(2)
C5-C4-H4B	108.7(16)	H14B-C14A-H14C	109.5	C8-C9-C10	117.9(2)
C6-C5-C10	111.5(2)	C6-C14B-H14E	109.5	C9-C10-C11	108.78(18)
C10-C5-C4	112.49(18)	C6-C14B-H14F	109.5	C9-C10-C5	110.46(18)
C10-C5-H5	106.6(16)	H14E-C14B-H14F	109.5	C11-C10-C5	109.9(2)
C14B-C6-C7	110.8(6)	C10-C15-H15B	109.5	C12-C11-H11A	108.(2)
C7-C6-C5	111.7(2)	C10-C15-H15C	109.5	C12-C11-H11B	116.(3)
C5-C6-C14A	100.2(18)	H15B-C15-H15C	109.5	H11A-C11-H11B	103.(4)
C7-C6-H6	115.(2)	C2-C1-O1	112.1(3)	C3-C12-C11	128.0(2)
C14A-C6-H6	117.(3)	O1-C1-H1	113.(3)	C2-C13-H13A	109.5
C8-C7-H7	118.(3)	C1-C2-C13	128.0(3)	H13A-C13-H13B	109.5
C7-C8-C9	121.8(2)	C12-C3-C2	106.7(2)	H13A-C13-H13C	109.5
C9-C8-H8	113.6(19)	C2-C3-C4	131.1(2)	C6-C14A-H14A	109.5
O2-C9-C10	121.2(2)	C3-C4-H4	113.(2)	H14A-C14A-H14B	109.5
C9-C10-C15	105.81(19)	C3-C4-H4B	111.4(16)	H14A-C14A-H14C	109.5
C15-C10-C11	110.6(3)	H4-C4-H4B	104.(3)	C6-C14B-H14D	109.5
C15-C10-C5	111.17(19)	C6-C5-C4	110.9(2)	H14D-C14B-H14E	109.5
C12-C11-C10	107.9(2)	C6-C5-H5	108.6(16)	H14D-C14B-H14F	109.5
C10-C11-H11A	111.(2)	C4-C5-H5	106.5(16)	C10-C15-H15A	109.5
C10-C11-H11B	111.(3)	C14B-C6-C5	120.9(7)	H15A-C15-H15B	109.5
				H15A-C15-H15C	109.5

A.1.4: Torsion angles (°).

Attached atoms	Angle (°)	Attached atoms	Angle (°)
C12-O1-C1-C2	0.3(5)	O1-C1-C2-C3	-0.7(4)
O1-C1-C2-C13	177.8(3)	C1-C2-C3-C12	0.8(4)
C13-C2-C3-C12	-177.8(3)	C1-C2-C3-C4	177.7(3)
C13-C2-C3-C4	-0.8(5)	C12-C3-C4-C5	-9.2(4)
C2-C3-C4-C5	174.3(2)	C3-C4-C5-C6	165.4(2)
C3-C4-C5-C10	39.8(3)	C10-C5-C6-C14B	-179.3(12)
C4-C5-C6-C14B	54.5(12)	C10-C5-C6-C7	-46.2(3)
C4-C5-C6-C7	-172.3(3)	C10-C5-C6-C14A	-160.5(11)
C4-C5-C6-C14A	73.4(11)	C14B-C6-C7-C8	157.0(12)
C5-C6-C7-C8	19.0(5)	C14A-C6-C7-C8	128.(2)
C6-C7-C8-C9	2.2(6)	C7-C8-C9-O2	-178.4(3)
C7-C8-C9-C10	5.5(4)	O2-C9-C10-C15	-88.7(3)
C8-C9-C10-C15	87.4(3)	O2-C9-C10-C11	30.2(4)
C8-C9-C10-C11	-153.8(3)	O2-C9-C10-C5	150.9(2)
C8-C9-C10-C5	-33.0(3)	C6-C5-C10-C9	53.1(3)
C4-C5-C10-C9	178.37(18)	C6-C5-C10-C15	-64.1(3)
C4-C5-C10-C15	61.2(3)	C6-C5-C10-C11	173.1(2)
C4-C5-C10-C11	-61.6(3)	C9-C10-C11-C12	169.4(3)
C15-C10-C11-C12	-74.8(4)	C5-C10-C11-C12	48.3(4)
C2-C3-C12-O1	-0.6(4)	C4-C3-C12-O1	-177.9(3)
C2-C3-C12-C11	176.6(3)	C4-C3-C12-C11	-0.7(5)
C1-O1-C12-C3	0.2(4)	C1-O1-C12-C11	-177.3(4)
C10-C11-C12-C3	-19.7(5)	C10-C11-C12-O1	157.2(3)

A.2: Crystallographic data for the hydroxylactone (**6**).

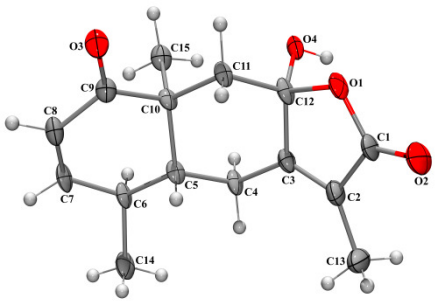

A.2.1: Crystal data.

Chemical formula	$C_{15}H_{18}O_4$	
Formula weight	262.29 g/mol	
Crystal size	0.127 x 0.179 x 0.251 mm	
Crystal habit	colorless prism	
Crystal system	orthorhombic	
Space group	P 21 21 21	
Unit cell dimensions	a = 7.6843(3) Å	α = 90°
	b = 12.7508(5) Å	β = 90°
	c = 13.5252(5) Å	γ = 90°
Volume	1325.21(9) $Å^3$	
Z	4	
Density (calculated)	1.315 g/cm^3	
Absorption coefficient	0.778 mm^{-1}	
F(000)	560	

A.2.2: Bond lengths.

Bond	Length (Å)	Bond	Length (Å)	Bond	Length (Å)	Bond	Length (Å)
O1-C1	1.363(3)	C8-C9	1.466(3)	O4-H4	0.84(4)	C11-C12	1.515(3)
O2-C1	1.200(3)	C9-C10	1.523(3)	C2-C3	1.325(4)	C11-H11B	0.97(3)
O4-C12	1.396(3)	C10-C15	1.548(3)	C3-C4	1.494(3)	C13-H13B	0.99(5)
C1-C2	1.485(4)	C11-H11A	0.93(3)	C4-C5	1.544(3)	C14-H14A	0.97(4)
C2-C13	1.485(4)	C13-H13A	0.95(5)	C4-H4B	0.92(3)	C14-H14C	0.91(4)
C3-C12	1.511(3)	C13-H13C	0.90(5)	C5-C10	1.559(3)	C15-H15B	0.96(3)
C4-H4A	0.98(3)	C14-H14B	0.95(4)	C6-C7	1.489(3)		
C5-C6	1.535(3)	C15-H15A	1.01(3)	C6-H6	0.93(3)		
C5-H5	0.96(3)	C15-H15C	0.99(4)	C7-H7	0.99(3)		
C6-C14	1.534(3)	O1-C12	1.456(3)	C8-H8	0.97(4)		
C7-C8	1.335(4)	O3-C9	1.227(3)	C10-C11	1.547(3)		

A.2.3: Bond angles (°).

Attached atoms	Angle (°)	Attached atoms	Angle (°)	Attached atoms	Angle (°)
C1-O1-C12	109.07(18)	O1-C12-C11	109.58(19)	O3-C9-C8	121.0(2)
O2-C1-O1	121.8(2)	C2-C13-H13A	107.(3)	C8-C9-C10	116.7(2)
O1-C1-C2	109.4(2)	H13A-C13-H13B	111.(4)	C9-C10-C15	104.14(19)
C3-C2-C13	131.8(3)	H13A-C13-H13C	107.(4)	C9-C10-C5	108.45(18)
C2-C3-C4	132.1(2)	C6-C14-H14A	112.(2)	C15-C10-C5	112.71(18)
C4-C3-C12	117.0(2)	H14A-C14-H14B	105.(3)	C12-C11-H11A	109.1(19)
C3-C4-H4A	111.1(18)	H14A-C14-H14C	110.(3)	C12-C11-H11B	109.5(19)
C3-C4-H4B	113.(2)	C10-C15-H15A	108.6(19)	H11A-C11-H11B	107.(3)
H4A-C4-H4B	106.(3)	H15A-C15-H15B	112.(3)	O4-C12-C3	113.33(19)
C6-C5-C10	111.99(18)	H15A-C15-H15C	103.(3)	O4-C12-C11	109.92(19)
C6-C5-H5	109.8(18)	C12-O4-H4	108.(2)	C3-C12-C11	111.55(19)
C10-C5-H5	105.4(18)	O2-C1-C2	128.7(3)	C2-C13-H13B	114.(3)
C7-C6-C5	110.42(19)	C3-C2-C1	107.2(2)	C2-C13-H13C	110.(3)
C7-C6-H6	108.(2)	C1-C2-C13	121.0(2)	H13B-C13-H13C	108.(4)
C5-C6-H6	109.(2)	C2-C3-C12	110.5(2)	C6-C14-H14B	109.(2)
C8-C7-H7	117.7(19)	C3-C4-C5	108.44(19)	C6-C14-H14C	112.(2)
C7-C8-C9	122.5(2)	C5-C4-H4A	110.1(19)	H14B-C14-H14C	109.(3)
C9-C8-H8	117.9(19)	C5-C4-H4B	108.(2)	C10-C15-H15B	111.(2)
O3-C9-C10	122.1(2)	C6-C5-C4	111.55(19)	C10-C15-H15C	114.(2)
C9-C10-C11	109.21(19)	C4-C5-C10	110.64(19)	H15B-C15-H15C	108.(3)
C11-C10-C15	111.46(18)	C4-C5-H5	107.2(18)		
C11-C10-C5	110.59(18)	C7-C6-C14	109.6(2)		
C12-C11-C10	112.87(18)	C14-C6-C5	113.3(2)		
C10-C11-H11A	108.6(19)	C14-C6-H6	106.5(19)		
C10-C11-H11B	109.8(19)	C8-C7-C6	124.3(2)		
O4-C12-O1	108.62(18)	C6-C7-H7	118.0(18)		
O1-C12-C3	103.59(18)	C7-C8-H8	119.6(19)		

A.2.4: Torsion angles (°).

Attached atoms	Angle (°)	Attached atoms	Angle (°)
C12-O1-C1-O2	-178.5(3)	C12-O1-C1-C2	-1.0(3)
O2-C1-C2-C3	175.2(3)	O1-C1-C2-C3	-2.1(3)
O2-C1-C2-C13	-3.0(5)	O1-C1-C2-C13	179.7(3)
C1-C2-C3-C4	-168.0(3)	C13-C2-C3-C4	10.0(5)
C1-C2-C3-C12	4.2(3)	C13-C2-C3-C12	-177.9(3)
C2-C3-C4-C5	116.8(3)	C12-C3-C4-C5	-55.0(3)
C3-C4-C5-C6	-177.83(19)	C3-C4-C5-C10	56.8(2)
C4-C5-C6-C7	-172.7(2)	C10-C5-C6-C7	-48.1(3)
C4-C5-C6-C14	63.9(3)	C10-C5-C6-C14	-171.4(2)
C14-C6-C7-C8	143.1(3)	C5-C6-C7-C8	17.7(3)
C6-C7-C8-C9	3.0(4)	C7-C8-C9-O3	-177.5(2)
C7-C8-C9-C10	7.9(4)	O3-C9-C10-C11	27.7(3)
C8-C9-C10-C11	-157.7(2)	O3-C9-C10-C15	-91.5(2)
C8-C9-C10-C15	83.1(2)	O3-C9-C10-C5	148.3(2)
C8-C9-C10-C5	-37.1(3)	C6-C5-C10-C9	57.9(2)
C4-C5-C10-C9	-177.00(18)	C6-C5-C10-C11	177.60(19)
C4-C5-C10-C11	-57.3(2)	C6-C5-C10-C15	-56.9(3)
C4-C5-C10-C15	68.2(2)	C9-C10-C11-C12	172.03(19)
C15-C10-C11-C12	-73.5(2)	C5-C10-C11-C12	52.8(2)
C1-O1-C12-O4	-117.5(2)	C1-O1-C12-C3	3.3(3)
C1-O1-C12-C11	122.4(2)	C2-C3-C12-O4	112.8(2)
C4-C3-C12-O4	-73.8(3)	C2-C3-C12-O1	-4.7(3)
C4-C3-C12-O1	168.73(19)	C2-C3-C12-C11	-122.5(2)
C4-C3-C12-C11	50.9(3)	C10-C11-C12-O4	78.6(2)
C10-C11-C12-O1	-162.13(18)	C10-C11-C12-C3	-48.0(3)

B. NMR data

B.1: Furanoterpenoid (4) in CD_2Cl_2.

B.1.1: ^1H data.

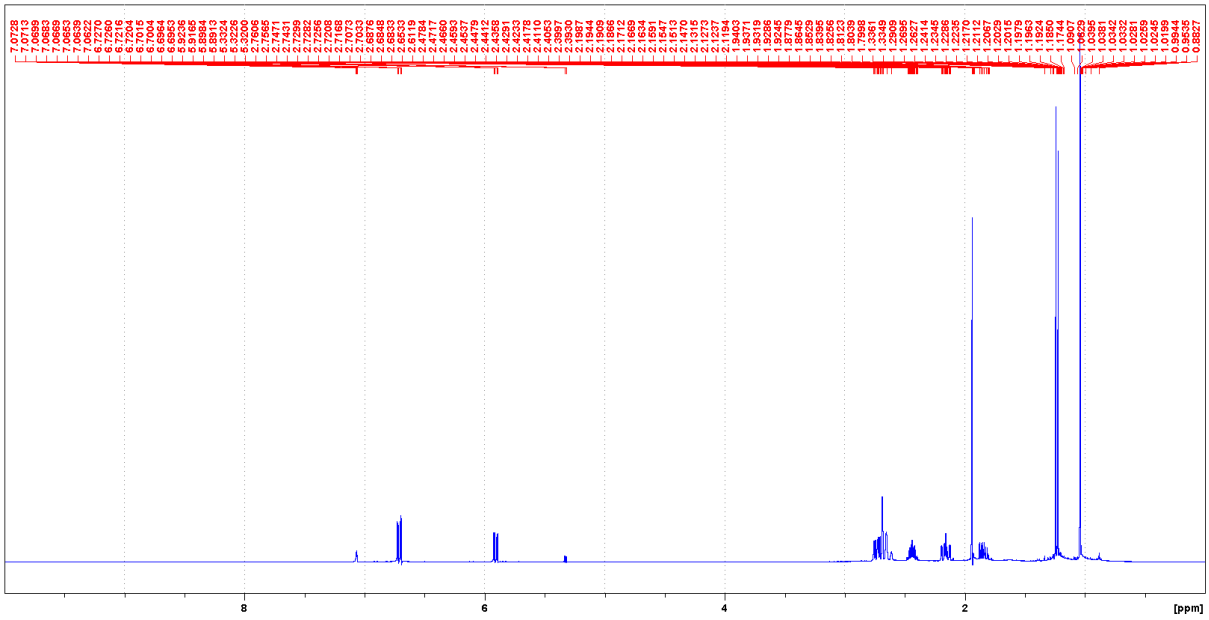

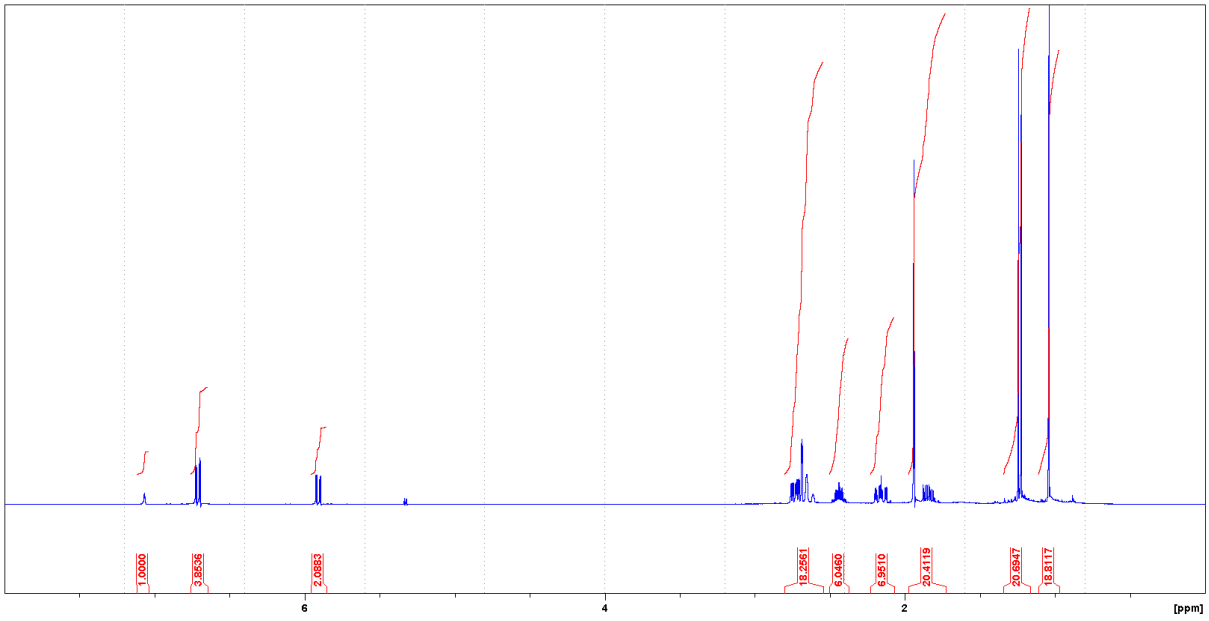

B.1.2: ^{13}C data.

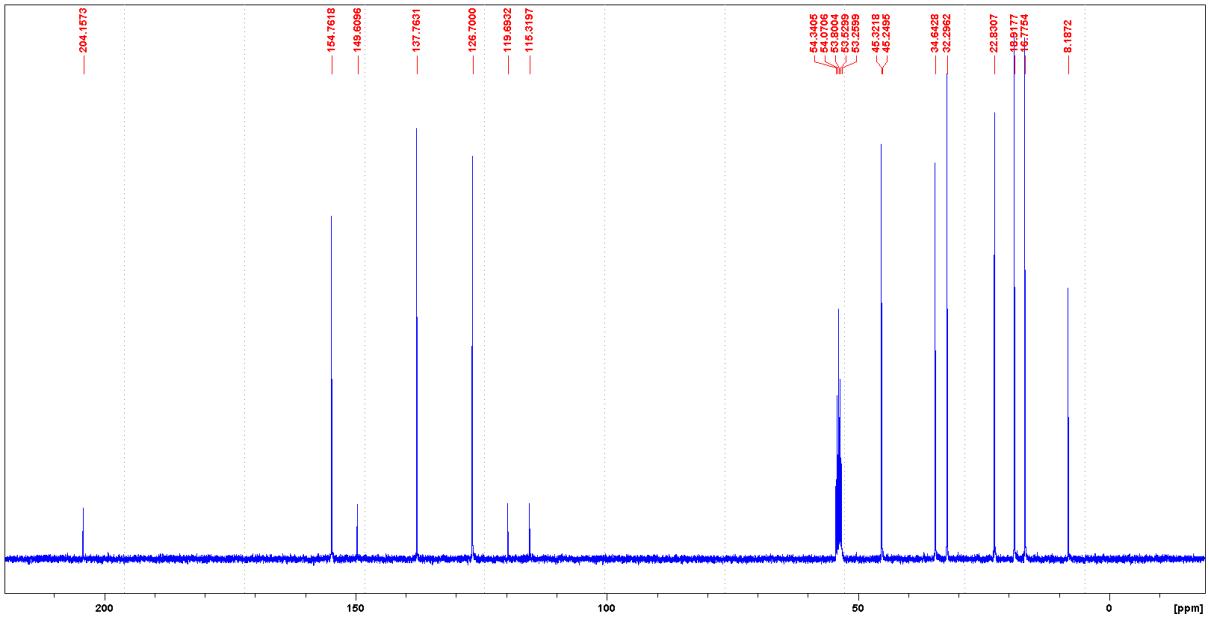

B.1.3: DEPT 135.

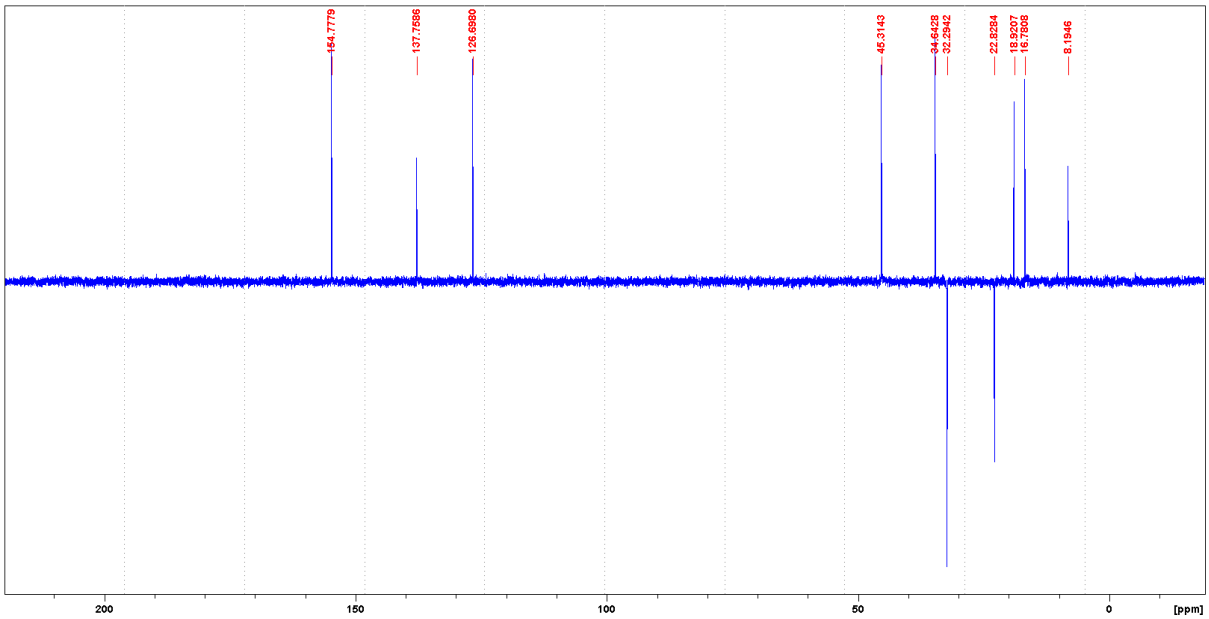

B.1.4: ^{1}H-^{1}H COSY.

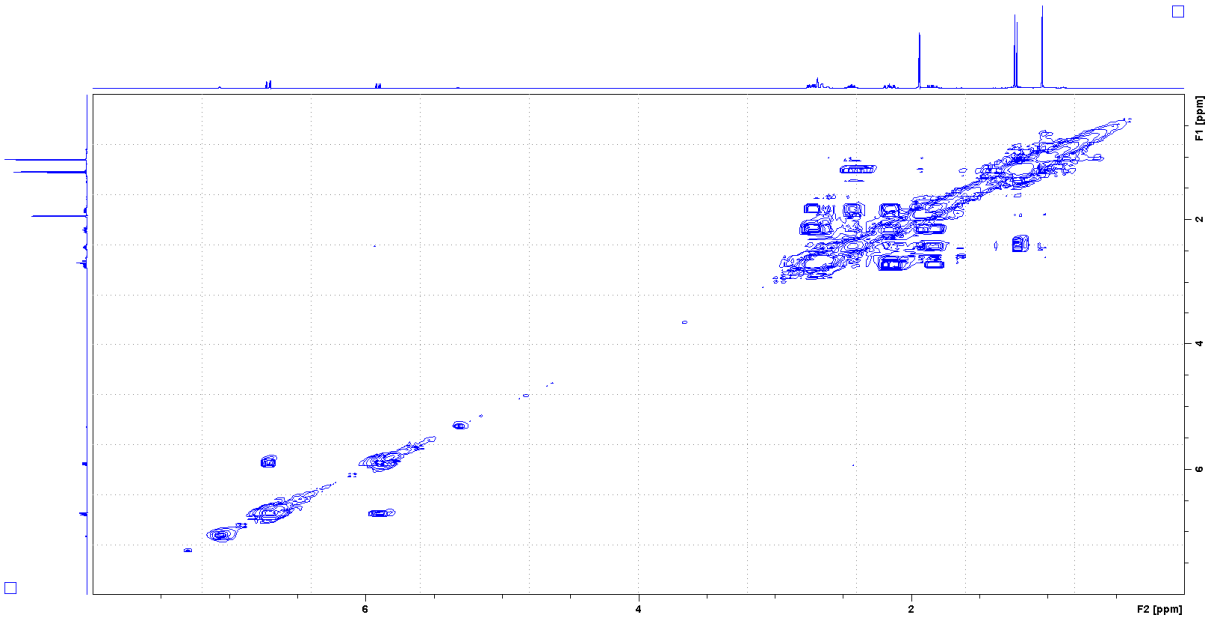

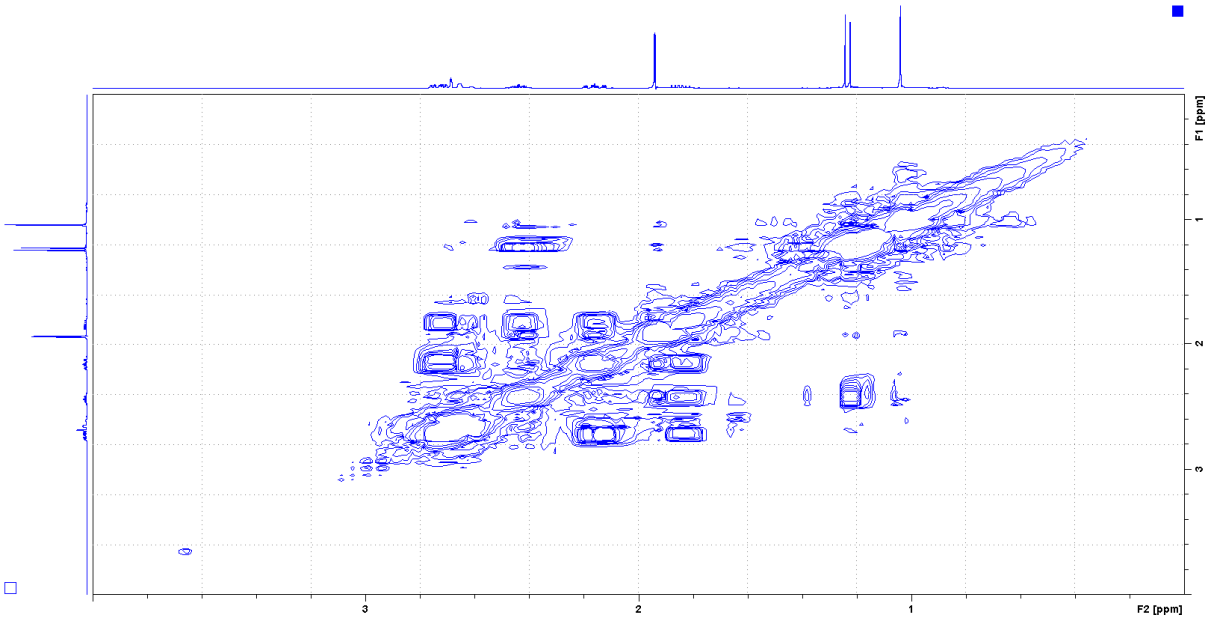

B.1.5: HSQC.

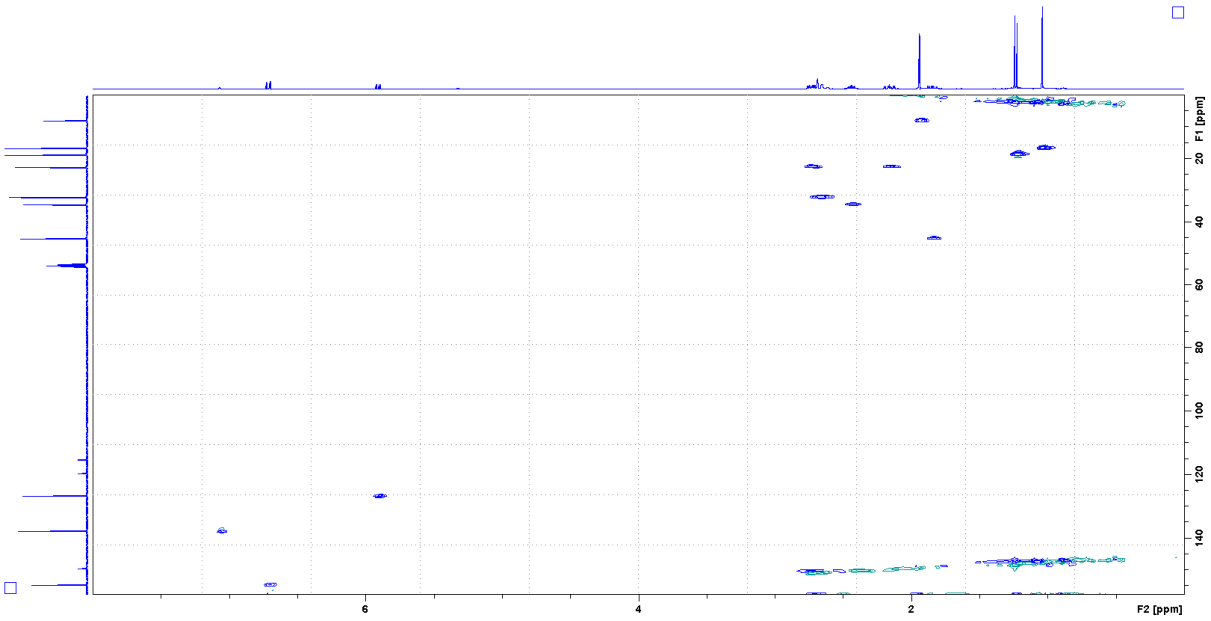

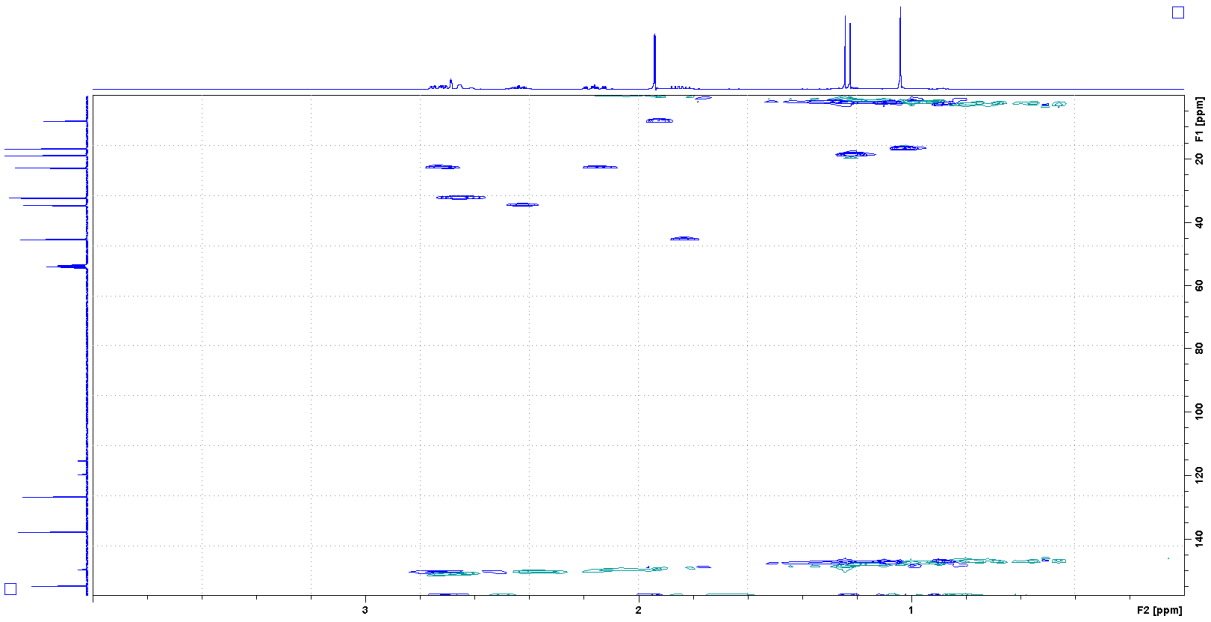

B.1.6: HMBC.

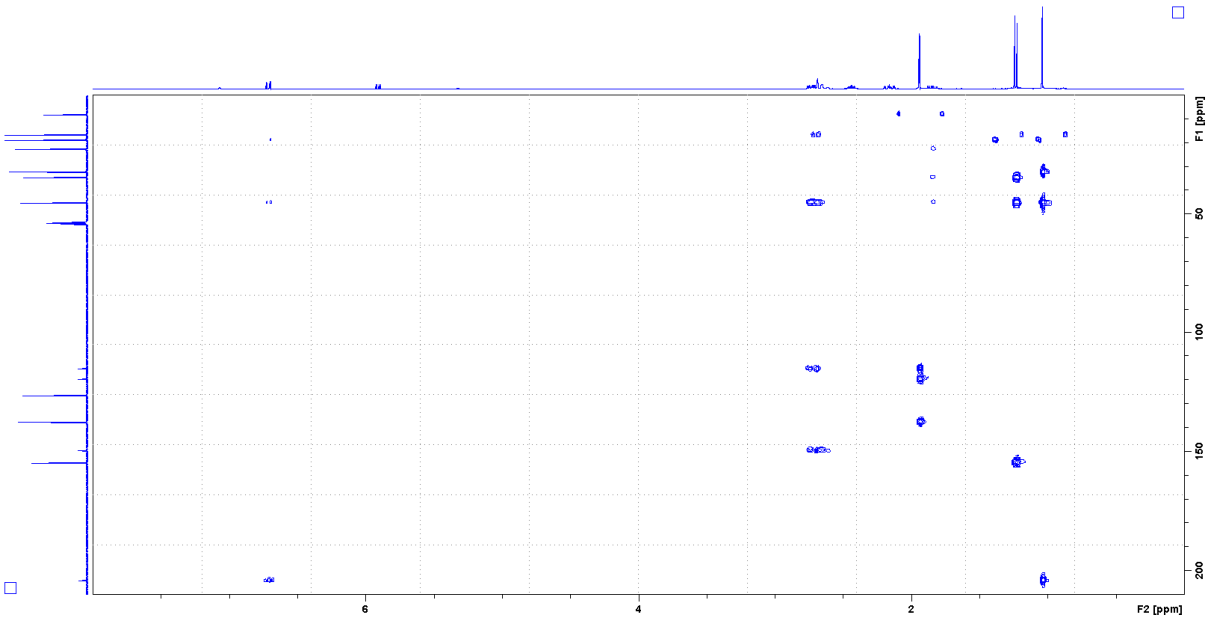

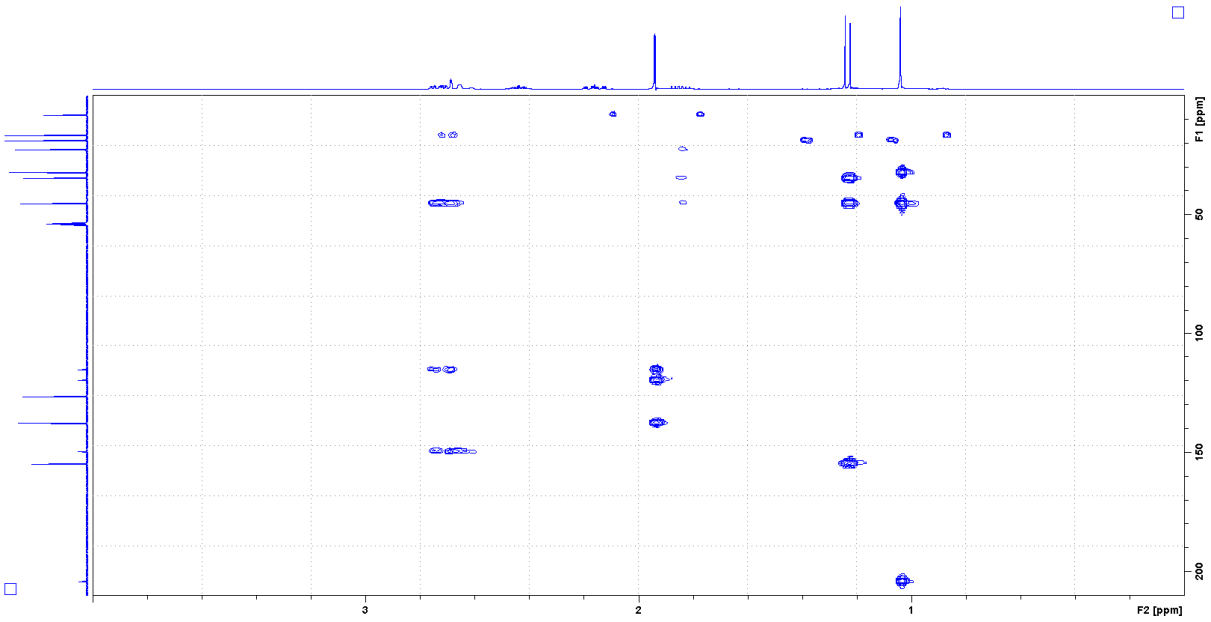

B.1.7: NOESY.

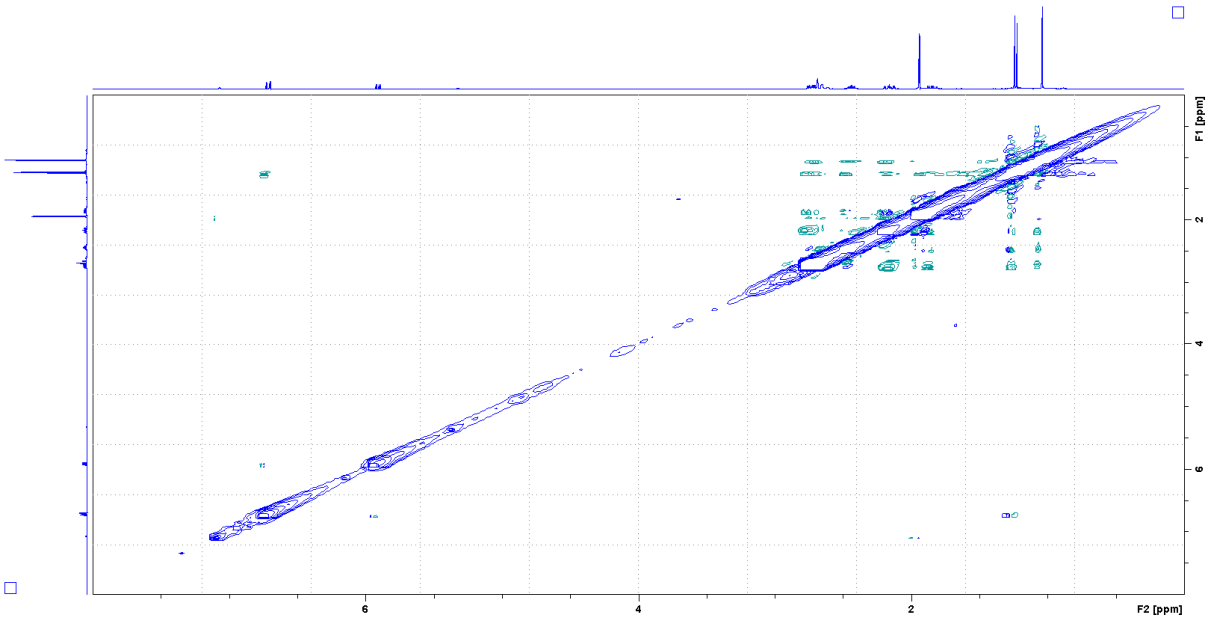

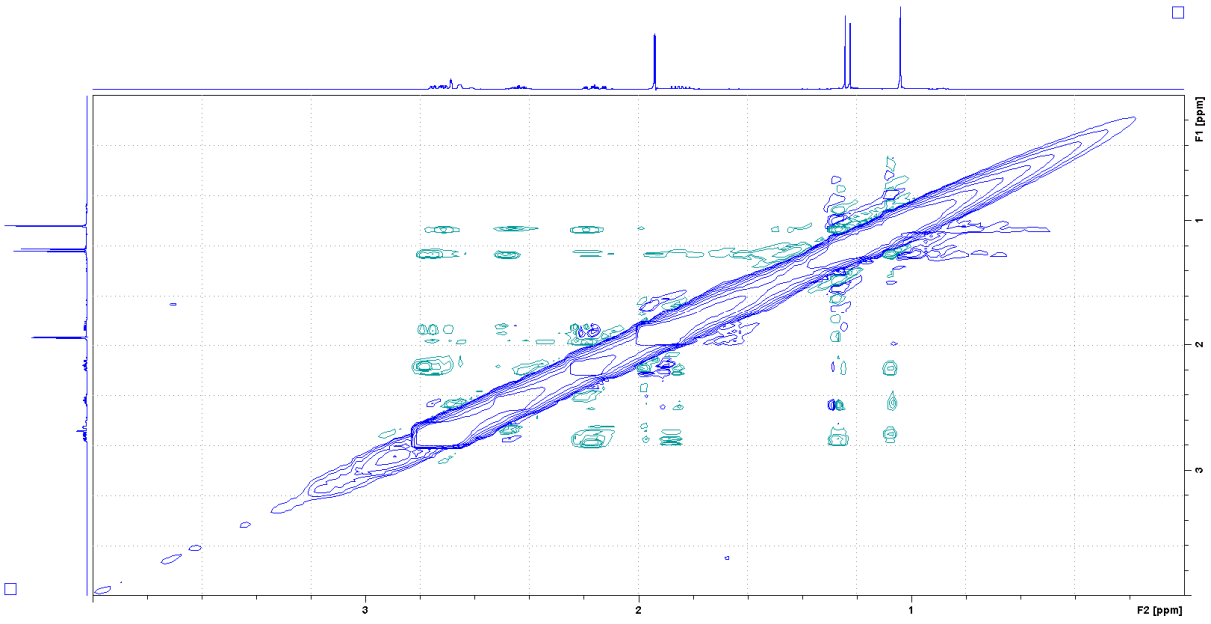

B.2: Hydroxylactone (6) in $CDCl_3$.

B.2.1: ^1H data.

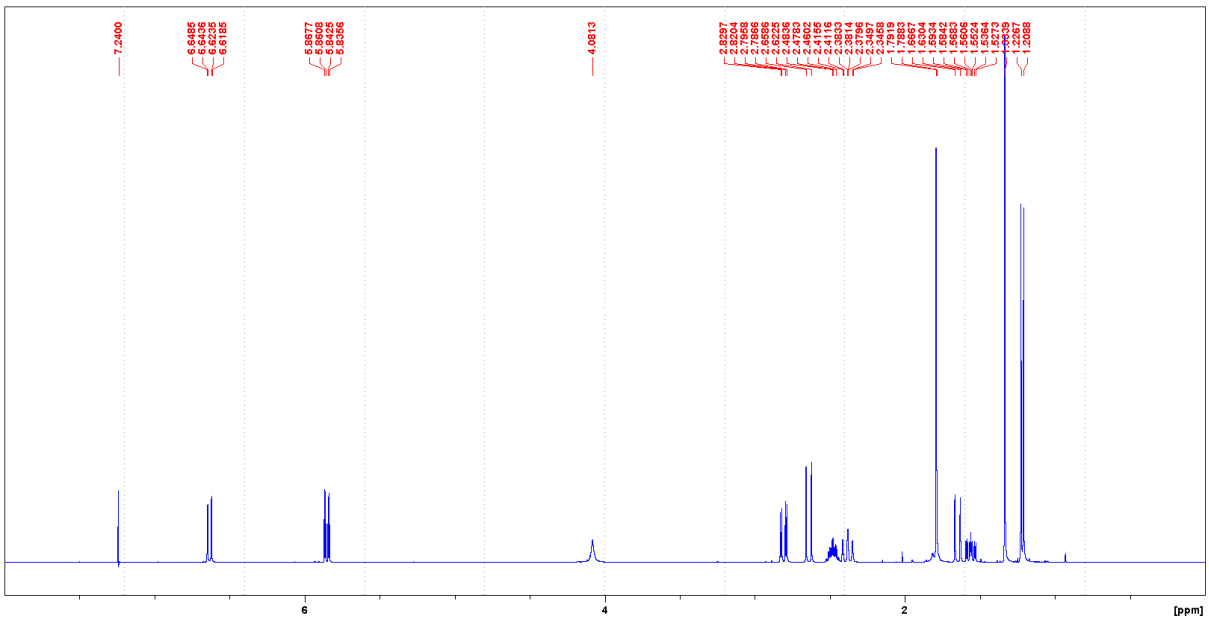

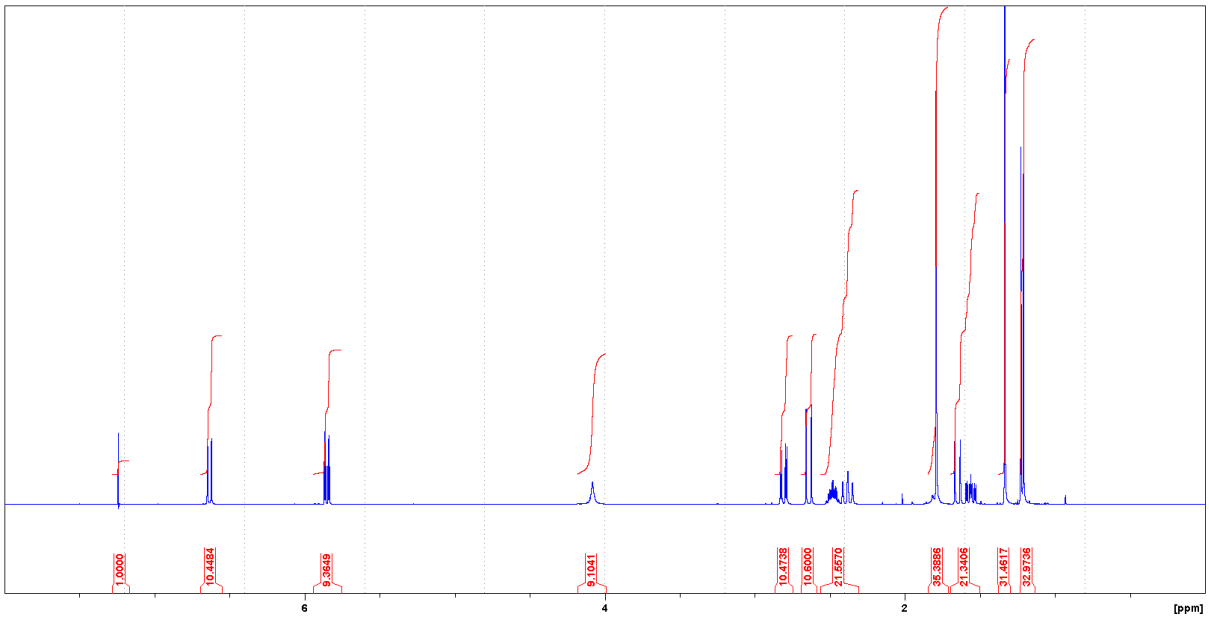

B.2.2: ^{13}C data.

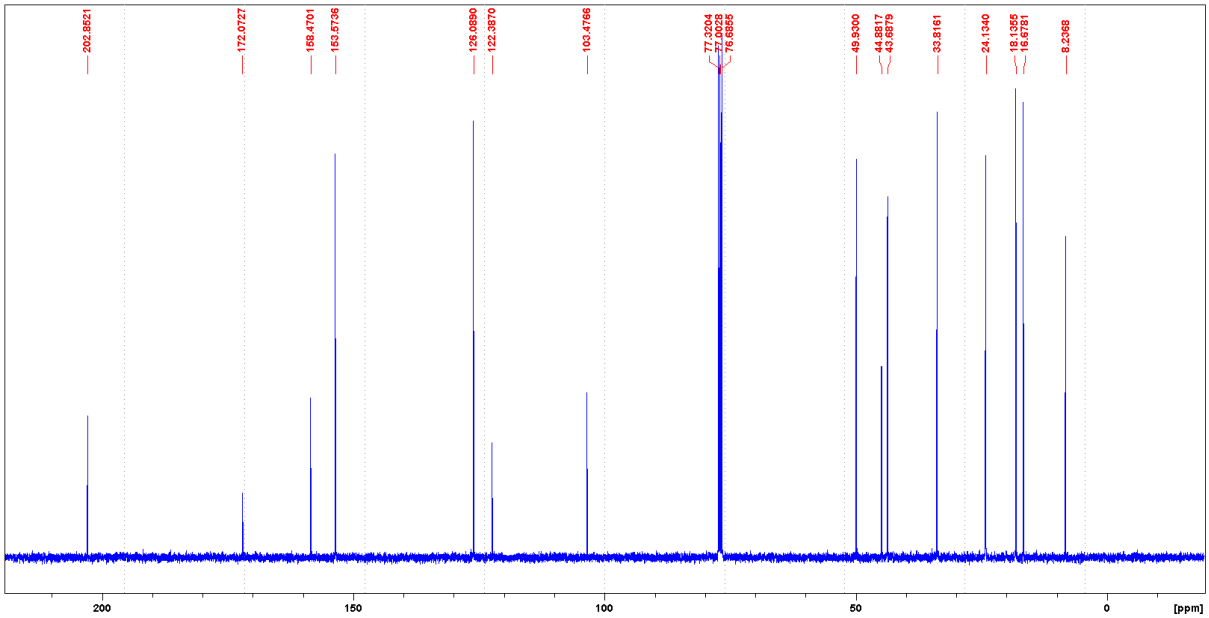

B.2.3: DEPT 135.

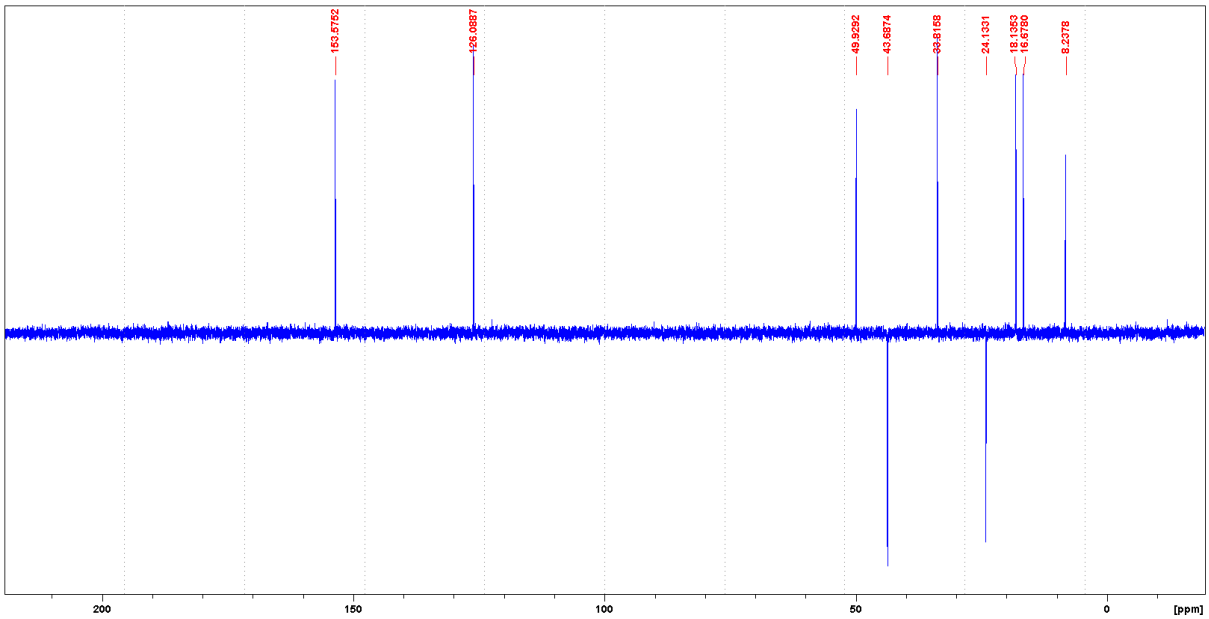

B.2.4: ^{1}H-^{1}H COSY.

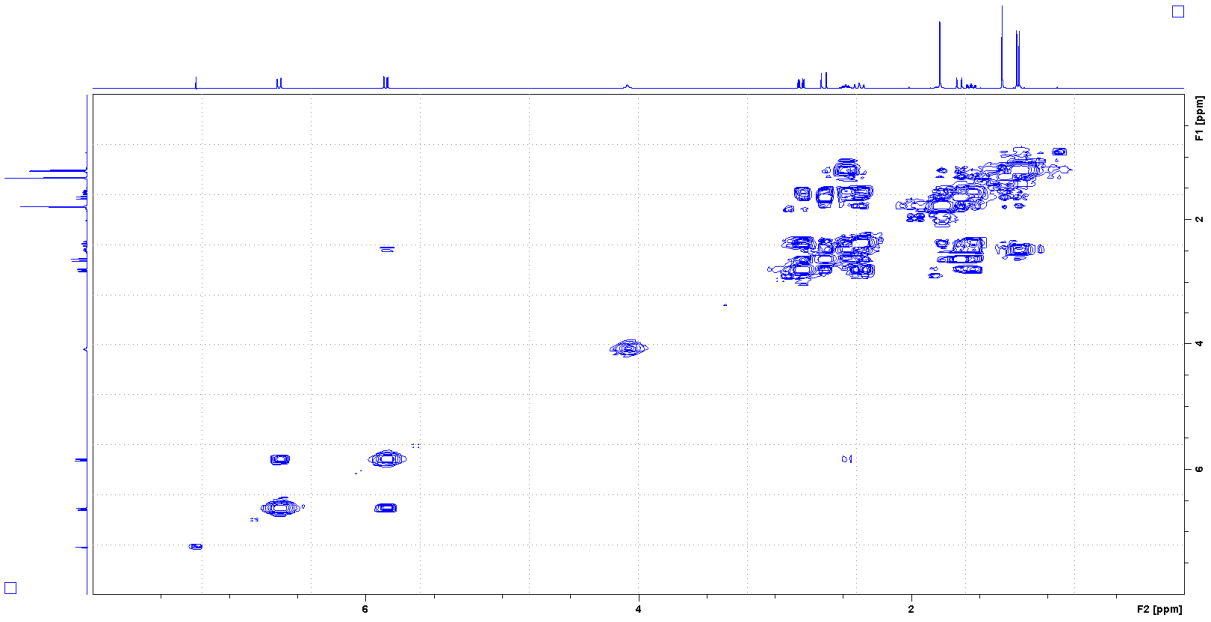

B.2.5: HSQC.

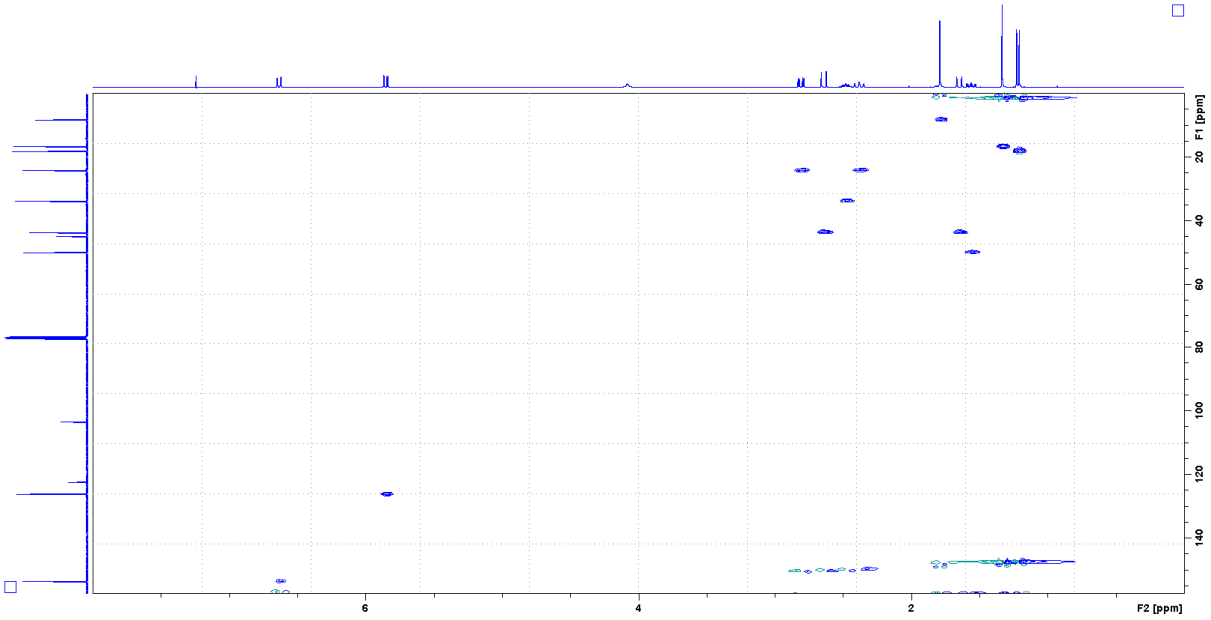

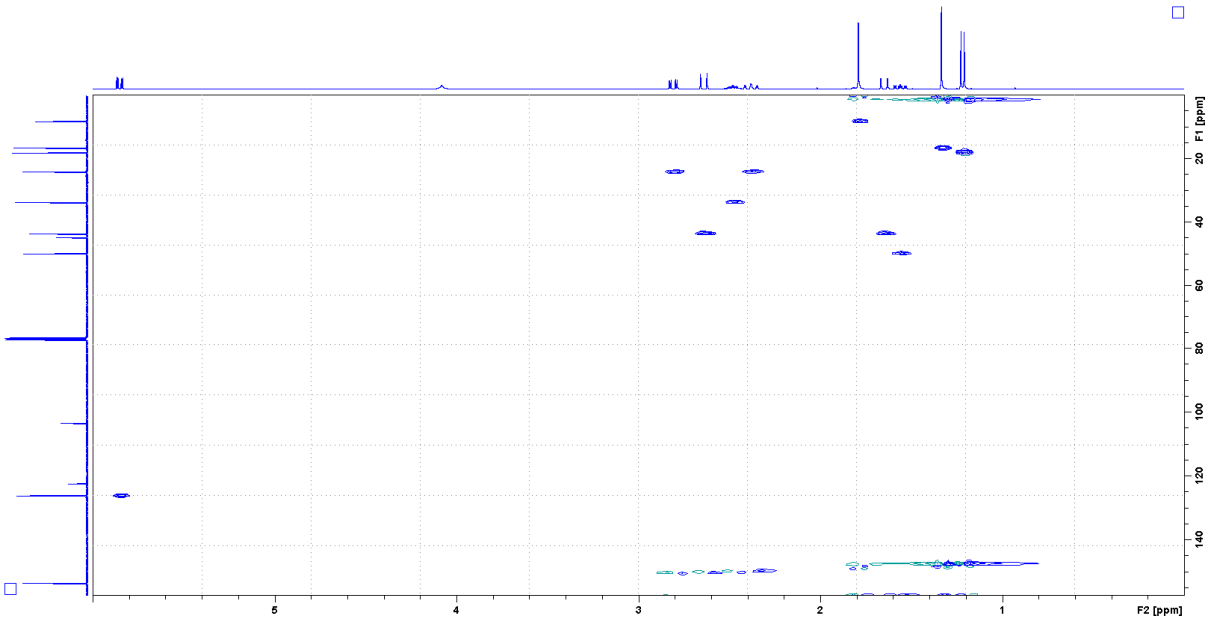

B.2.6: HMBC.

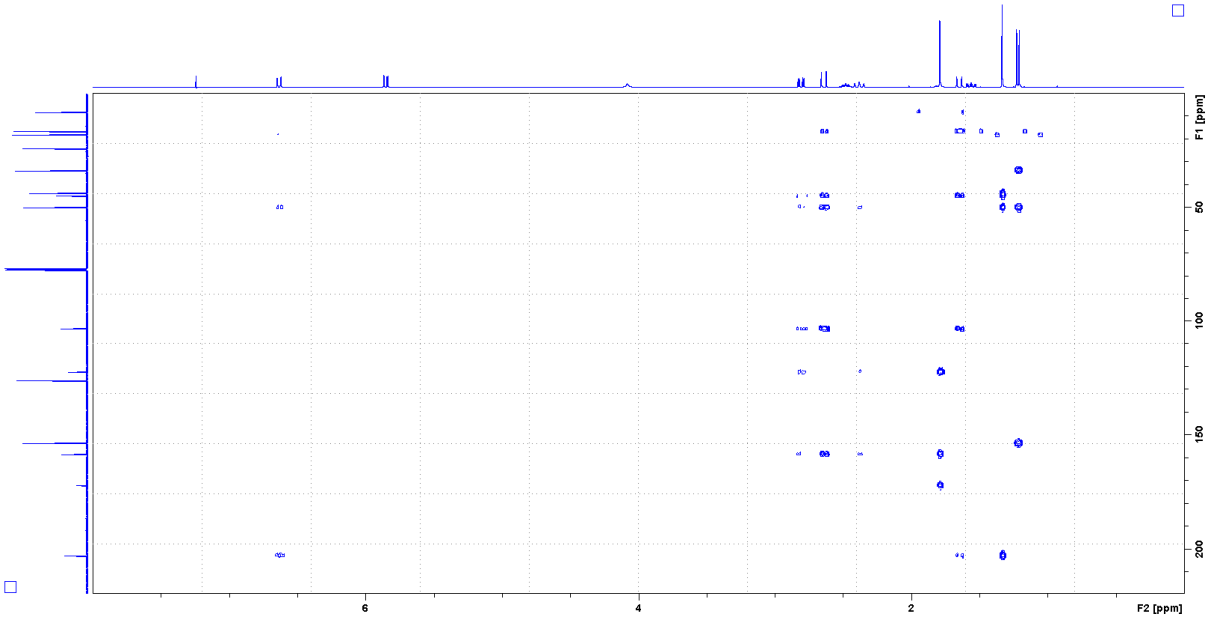

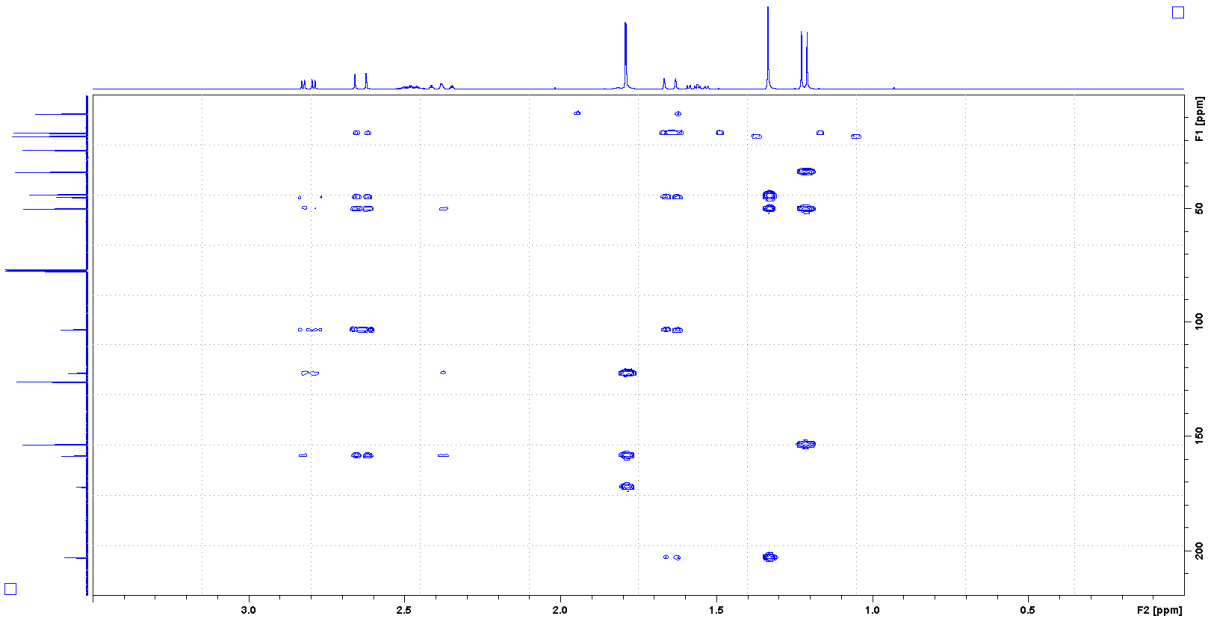

B.2.7: NOESY.

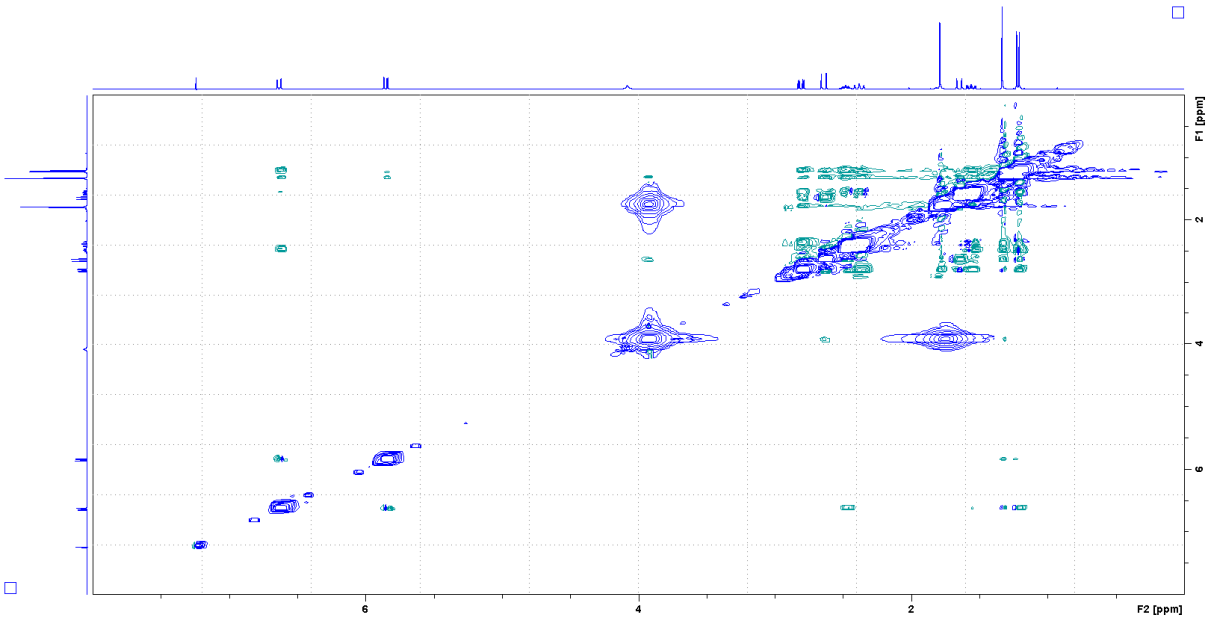

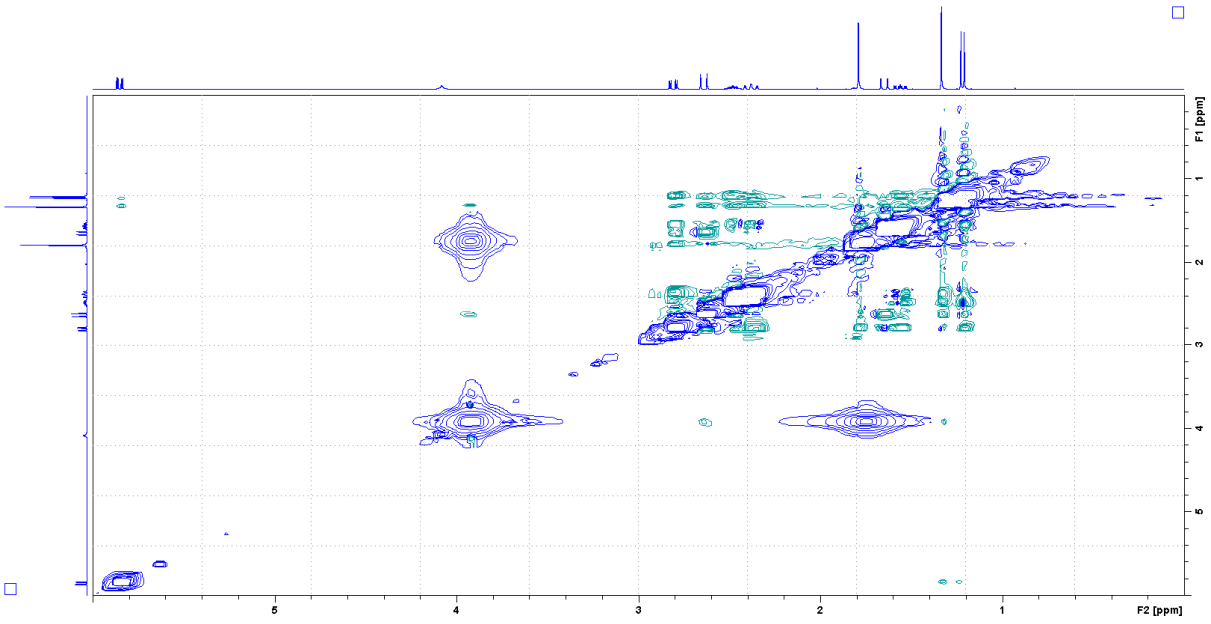

C. Mass spectrometry data

C.1: Furanoterpenoid (4) MS and MS/MS data (TOF MS ES+).

C.1.1: MS data.

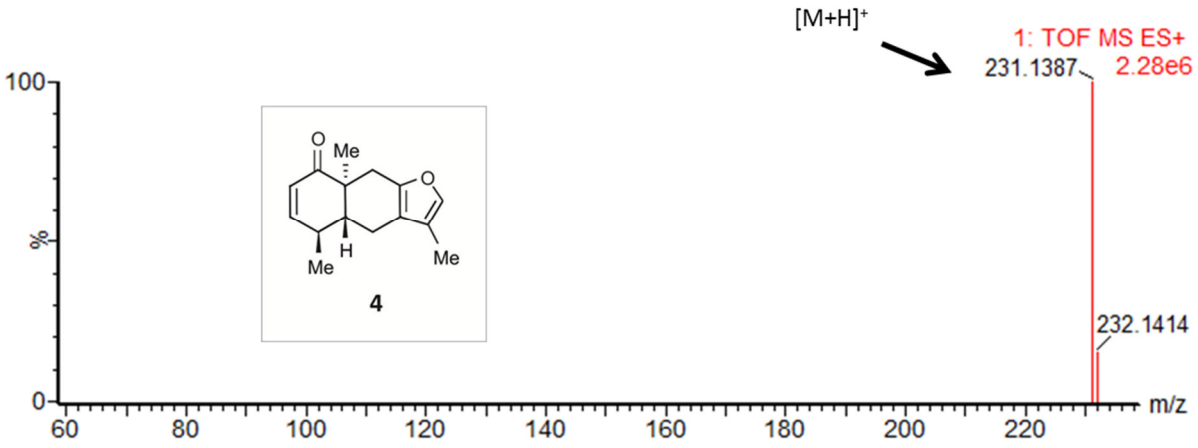

C.1.2: MS/MS data.

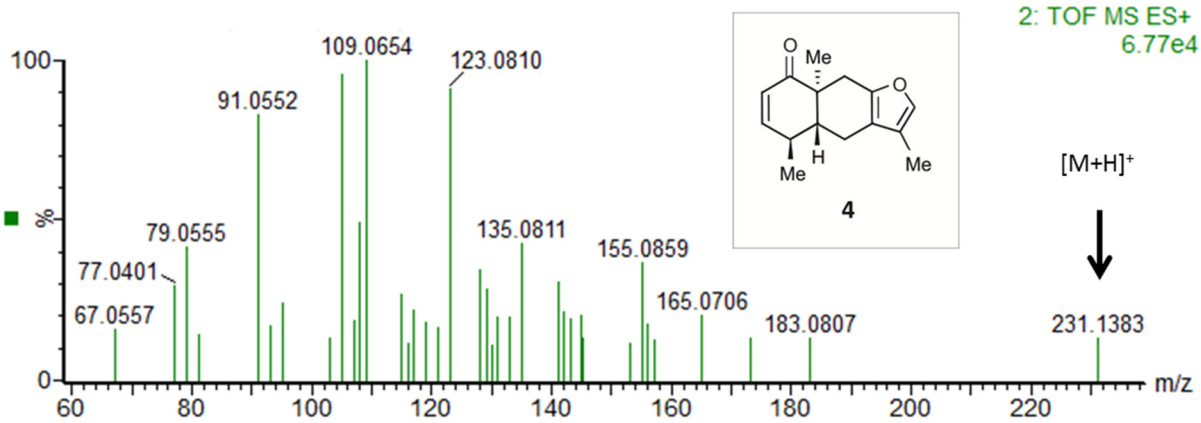

Note: *the fluctuation in the last two decimals between the m/Z in the MS and MS/MS data is due to the calibration of the machine.*

C.2: Hydroxylactone (6) MS and MS/MS data (TOF MS ES+ and TOF MS ES-).

C.2.1: MS data (TOF MS ES+).

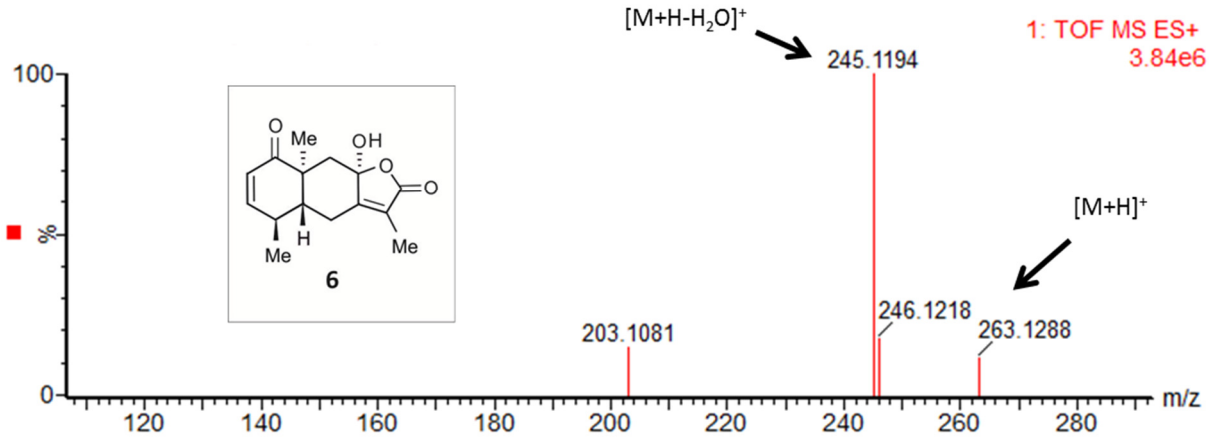

C.2.2: MS/MS data (TOF MS ES+).

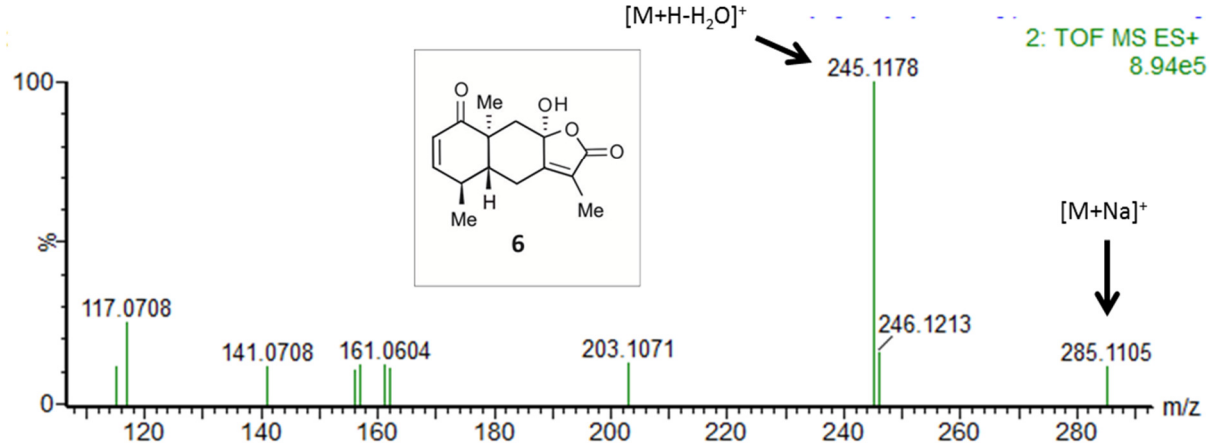

Note: *the fluctuation in the last two decimals between the m/Z in the MS and MS/MS data is due to the calibration of the machine.*

C.2.3: MS data (TOF MS ES-).

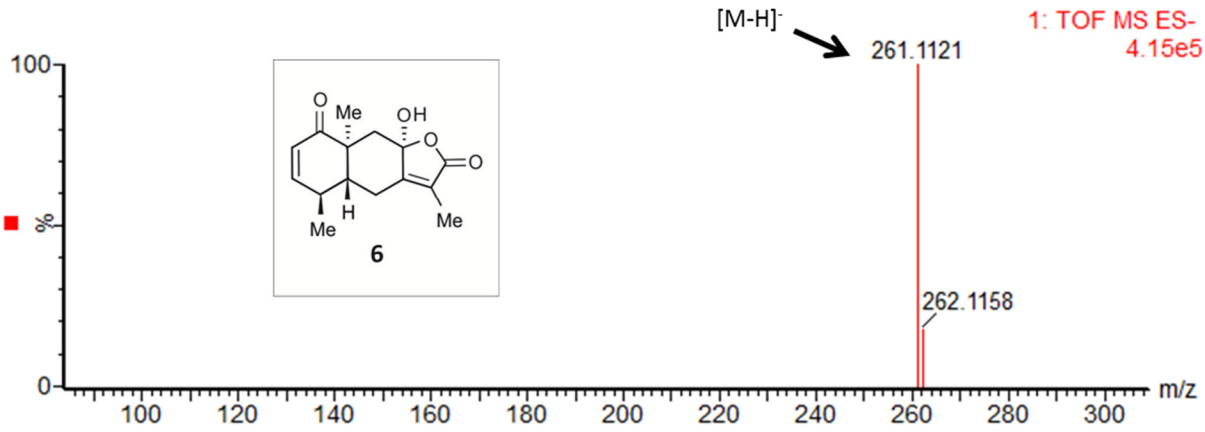

C.2.3: MS/MS data (TOF MS ES-).

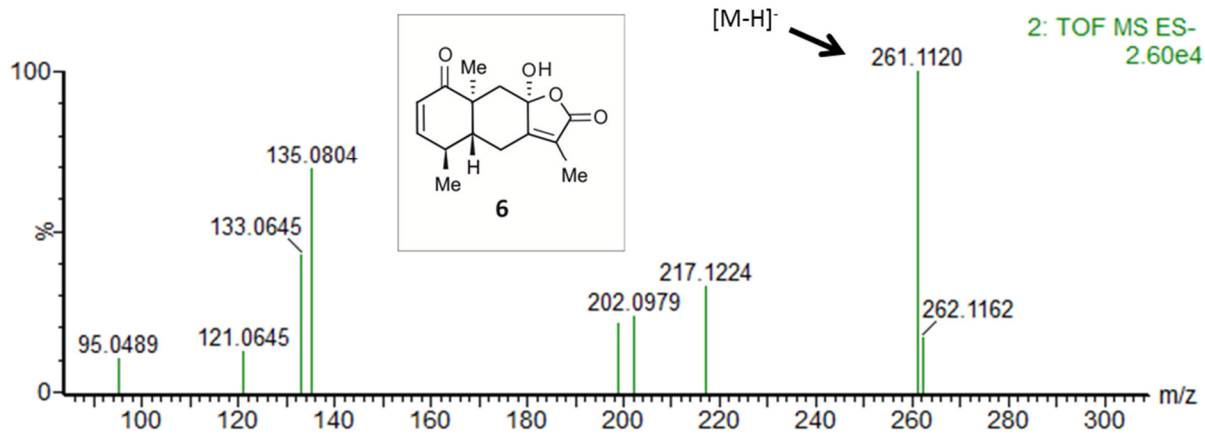

Note: *the fluctuation in the last two decimals between the m/Z in the MS and MS/MS data is due to the calibration of the machine.*

D. UV shift and σ values used for the reported CD curves

D.1: UV shift and σ values used for CD simulations.

N° Figure	UV shift (nm)	σ (eV)
3.15	- 22	0.28
3.16	5	0.25
3.17	10	0.28
3.18	16	0.20
3.19	27	0.29
3.21	0	0.30
3.22	13	0.22
3.24	- 22	0.18
3.25	14	0.22
3.26	- 23	0.18
3.27	33	0.34